

Luminescence Photophysics and Oxygen Sensing Properties of Ru(II) Complexes in Room
Temperature Ionic Liquids and Ionic Liquid Encapsulated Gels

A Dissertation

Presented to
the faculty of the School of Engineering and Applied Science
University of Virginia

in partial fulfillment
of the requirements for the degree

Doctor of Philosophy

by

Kaleem Jamar Morris

May

2012

APPROVAL SHEET

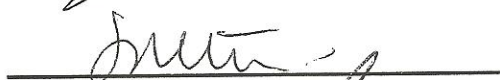
The dissertation
is submitted in partial fulfillment of the requirements
for the degree of
Doctor of Philosophy

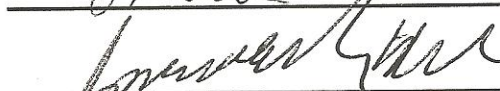

AUTHOR

The dissertation has been read and approved by the examining committee:

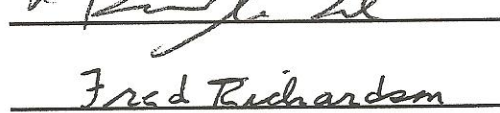

Advisor



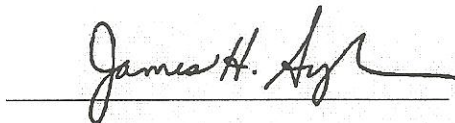








Accepted for the School of Engineering and Applied Science:



Dean, School of Engineering and Applied Science

May
2012

Dedication

This work is dedicated to my daughter, Ka'Leem, my nieces, nephews, and all of my beautiful God-children.

“Optimism is the faith that leads to achievement; nothing can be done without hope and confidence.” Helen Keller

Acknowledgements

There are so many who have contributed to what success I have obtained. If not for them, I would have never been in the position to obtain my doctorate from the University of Virginia. All too often it is only after a significant achievement or recognition that we take the time to acknowledge those who have guided, encouraged, assisted, or helped pave the often rocky way. Nevertheless, I would like to take this opportunity to thank the following people without whom this dissertation would not be possible:

My daughter, Ka'Leem Jasmine Patrice for being my inspiration.

My advisor, James Demas, for his academic and personal support.

My committee members, Fred Richardson, Rosanne Ford, Lloyd Harriott, Simonetta Liuti, and James Fitz-Gerald for their time and effort.

Bethany Leavens, for her assistance in the lab as well as her valued friendship.

Evan Reynolds, for helping with experimental measurements.

All the Demas group members past and present for their assistance over the years.

Ammasi Periasamy and Yuansheng Sun, for their aid with the fluorescence microscope.

Jim Werner, and Andrew Dattlebaum, for their assistance with preliminary work at Los Alamos National Laboratory.

Gary Baker, for providing the room temperature ionic liquids used in my study.

My M.S. advisor, Mikhail Noginov, for introducing me to luminescence and research, as well as scientific writing and speaking. Also, for challenging me to be better and then teaching me how.

My first academic advisor, Vina Punjabi, for introducing me to Physics and convincing me to switch my major. Also, it was your guidance early on that set me on my academic path.

My Mom, Dad, God-mom, God-dad, sisters, brothers, aunts, uncles, cousins, and the rest of my family and friends, for their love and support.

Abstract	i
Chapter 1: Introduction	1
Chapter 2: Oxygen Sensing	11
A. General Background	12
B. Traditional Oxygen Sensing Methodology	13
Chapter 3: Luminescence	20
A. Fluorescence and Phosphorescence	21
B. Intensity vs. Lifetime Measurements	24
C. Ru(II) Transition Metal Complexes	28
D. Luminescence Based Oxygen Sensing	33
Chapter 4: Development of Luminescence Lifetime Standards	39
A. Introduction	40
B. Results and Discussion	48
C. Conclusion	58
Chapter 5: Room Temperature Ionic Liquids	63
A. General Background	64
B. Structure of RTILs	68
Chapter 6: Ru(II)/Ionic Liquid Oxygen Sensing Properties	74
A. Introduction	75
B. Results and Discussion	82
C. Lifetime Temperature Dependence Measurements	97
i. Results and Discussion	100
ii. Conclusion	106
Chapter 7: Oxygen Diffusion in RTILs: Confocal Fluorescence Microscopy Method	110
A. Introduction	111
B. Fluorescence Microscopy Background	112
C. Confocal Fluorescence Microscopy	120
D. Method Verification by Diffusion of Oxygen in Water	125
E. Oxygen Diffusion in RTILs	139
i. Results and Discussion	144
ii. Conclusions	154
Chapter 8: Oxygen Diffusion in RTILs: Electrochemical Method	158
A. Introduction	159
B. Electrochemistry Background	160

C. Working Electrode Electrochemical Radius Determination	167
i. Results and Discussion	171
D. Oxygen Diffusion in RTILs	179
i. Results and Discussion	182
ii. Conclusion	195
Chapter 9: Discussion and Future Work	201
A. Introduction	202
B. Oxygen Diffusion Measurements	203
C. Quenching Rate Constants	205
D. Ionic Liquid Encapsulated Gels Oxygen Sensing Properties	213
E. Conclusions and Future Work	217

Abstract

Due to their high stability, relatively low cost, and remote sensing capabilities luminescence based oxygen sensors have become a popular choice for many oxygen detection applications. Many luminescence based oxygen sensors are based on the oxygen quenching of a luminescent transition metal complex (TMCs). Since the local environment of the luminophore affects the luminescence and oxygen sensing properties of the probe, the support plays a critical role in the operation of the sensor.

Room temperature ionic liquids (RTILs) are an interesting new class of materials with many fascinating properties. RTILs are revolutionizing many areas of chemistry ranging from electrochemistry, catalysis, and green chemistry. In spite of many desirable properties, little research has been reported on the use of RTILs as supports for luminescent probes. A series of new luminescence based oxygen sensors comprised of one of two ruthenium(II) TMCs dissolved in a various RTILs has been developed. The two ruthenium complex described in this study are tris-(4,7-diphenyl-1,10-phenanthroline)ruthenium(II) dichloride, $[\text{Ru}(\text{dpp})_3]\text{Cl}_2$, and tris-(2,2'-bipyridine)ruthenium(II) dichloride, $[\text{Ru}(\text{bpy})_3]\text{Cl}_2$.

The photophysical and oxygen sensing properties of the newly developed oxygen sensors have been investigated. Lifetime measurements reveal a peculiar viscosity effect on the oxygen quenching of the luminescent metal complexes. Anomalously high bimolecular quenching rate constants, as much as three orders of magnitude greater than the predicted diffusion-limited quenching rate constants have been observed.

To better understand the remarkably high quenching behavior in the new Ru(II)/RTIL sensors, a new technique for measuring oxygen diffusion using a commercial fluorescence confocal microscope has been developed. From the solution of the Fick's Law diffusion equation, the quenching properties of the luminophore, and the sample thickness, diffusion coefficients of the sensors were calculated from the time dependence of the emission intensity. Chronoamperometric measurements of the electrochemical reduction of oxygen at the surface of a 10 micron diameter, platinum micro-disk electrode was used to provide independent confirmation of the measured diffusion coefficient as well obtain oxygen solubility in each of the new oxygen sensors.

Our results show the high quenching constants in RTILs are due to anomalously high diffusion coefficients. We explain this high oxygen quenching in the RTILs to the structure of these unique systems.

Photophysical and oxygen sensing properties of [Emim][Tf₂N] (methyl-tributylammonium bis(pentafluoroethylsulfonyl) imide) RTIL encapsulated in 28% by weight silica sol gel were examined. Results show that the lifetime and the oxygen sensing properties of the ionic liquid encapsulated gel (ILEG) are remarkably similar to that of the pure [Emim][Tf₂N] ionic liquid. This is explained using a domain model where the TMC is dissolved in solvent pools.

Chapter 1: Introduction

Luminescence is defined by spectroscopy guru Lakowicz as the emission of light from any substance.¹ There are many different types of luminescence: bioluminescence, in which light is emitted by a living organism; electroluminescence, where emission is a result of electrical current passing through a material; chemiluminescence, in which luminescence is a product of a chemical reaction; sonoluminescence, in which the emission is caused by the cavitation of bubbles in liquid after being excited by sound; thermoluminescence, where the emission of light comes from a heated substance; radioluminescence, which is caused by radioactive materials; and photoluminescence, in which the emission of light comes from a substance that has been excited by a photon.

The different forms of luminescence have intrigued mankind for ages. Many in the field of luminescence have heard the story of how Sir George Stokes, while having a gin and tonic, was amazed when he noticed his drink was producing a beautiful light blue glow. Stokes later came to realize that the blue glow was luminescence from the excited quinine molecules in the tonic water.

Stokes however, was not the first man to observe luminescence. Since the beginning, mankind has certainly observed and wondered at the many luminescence forms.

The aurora borealis and the aurora australis are forms of luminescence that have been naturally occurring in the northern and southern skies since before man's existence.² Also known as the northern lights, the aurora borealis is named after both the Roman goddess Aurora and the Greek name for the north wind, Boreas.³ The northern lights are the emission of photons from nitrogen and oxygen excited by charged particles that have been ejected from the sun's atmosphere. This remarkable display of light is a complex interplay involving the solar wind, the earth's magnetic field, and atmospheric gases of nitrogen and oxygen.

Bioluminescence is another form of naturally occurring luminescence that has been observed since man's beginning. For example, the common firefly produces bioluminescence. The bioluminescence from the firefly is a form of chemiluminescence in which a catalytic protein increases the efficiency of a chemiluminescent reaction. Also, up to ninety percent of all deep sea marine life produces bioluminescence.⁴

While the northern lights and many forms of bioluminescent creatures may have fascinated man since his beginning, the first known luminescence study wasn't until 1603.⁵ That's when an alchemist named Vincenzo Cascariolo heated a mixture of barium sulfate and coal and observed a bright glow emanating from the stone. Although elemental phosphorus wasn't

isolated until 1669, the people of that time called the glowing substance phosphorus, which meant “light bearer”.⁶

Since that first luminescence investigation of glowing rocks in 1603, countless experiments involving luminescence has been performed. Currently, luminescence research and applications are vast and cover a wide range of areas and specialties. For example, temperature sensors,⁷ fluorescent lamps, DNA labeling,⁸ night lights, mobile phone backlighting, and video display screens⁹ are a few of the many ways in which the use of luminescence is currently applied.

Not only are forms of luminescence being extensively studied, but luminescence itself is a major tool in different research processes as well. Medical, biomedical, and biological studies are prime examples of where luminescence is used as a tool in research. It used to be that the majority of biological and medical research experiments involved dissecting organisms and studying them under optical microscopes. Today, fluorescence, in particular fluorescence microscopy, is the major tool in biological and biomedical research. The creation of fluorescence microscopy has allowed advances in biological and biomedical research that would have never been achieved with conventional optical microscopy.

In a less specific sense, the invention of lasers, more recently, light emitting diodes (LEDs), and quantum dots have allowed luminescence to help advance research in many other areas.¹⁰⁻¹¹ These luminescence-based devices, as well as others, are the corner stone of many research endeavors. Further, luminescence has been a major driving force in many technological advances in the last few decades.

One such area aided by the use of luminescence is that of sensor technology. The ability of luminescent sensors to remotely detect small amounts of a substance has led to major advancements in sensing.

In luminescence sensing techniques, photophysical properties of the luminescent probe are directly or indirectly altered by the analyte under investigation. PET (Photo-induced Electron Transfer) sensors are a form of the latter.

A PET sensor consists of a luminophore connected to a receptor. When excited, the luminophore transfers an electron to or from the receptor depending on the design of the system; this transfer quenches (deactivates) the luminescence. Upon binding of the analyte under investigation to the receptor, the reduction/oxidation potential of the receptor changes; thus, making electron transfer more or less favorable between the receptor and

luminophore. The PET sensor may also be designed such that the binding of the analyte to the receptor raises or lowers the oxidation/reduction potential of the receptor to the point where the electron transfer between the luminophore and receptor is no longer possible; thus, the luminescence is enhanced by the binding of the analyte to the receptor.¹² The result is a “turn off” or “turn on” luminescence sensor, depending on the luminophore, the receptor, and design of the system.

As mentioned above, another luminescence sensing technique is when the analyte under investigation directly causes a change in the photophysical properties of the luminescent probe; in this case, luminescence characteristics such as emission intensity, emission spectrum, and/or lifetime of the luminescent probe is altered in the presence of the analyte. This work focuses on the development and study of luminescent oxygen probes based on bimolecular quenching of the luminescence by oxygen.

Luminescence has revolutionized sensor technology. Much interest has been given to utilizing the properties of luminescence for sensing purposes. Among other applications, luminescence probes are currently implemented as pH monitors, temperature sensors, drug residue detectors, environmental pollution probes, and sensors for blood glucose levels.¹³

Many studies have been performed involving the design, implementation, and enhancement of various luminescence based sensors. In this work, the development of luminescence-based oxygen sensors comprised of two luminescent Ru(II) complexes supported in a series of room temperature ionic liquids (RTILs) are discussed. The photophysical behavior and oxygen sensing properties of the new luminescence-based oxygen probes were examined. In order to fully characterize the systems, we needed diffusion coefficients for oxygen in the RTILs. A unique method involving fluorescence confocal microscopy was developed to measure the diffusion of oxygen. Based on the results of this work, a clearer understanding of the structure of the sensor supports was achieved and the anomalously high quenching in the newly developed oxygen sensors explained.

When designing any sensor, the practical application of the sensor must be considered. Since having the newly developed oxygen sensors in solution is not in general practical for real world applications, RTILs encapsulated in silica sol gels were created. The RTILs encapsulated in silica sol gels provided a transparent rigid support for the luminescence based oxygen sensors.

Finally, the sensing properties of the RTILs encapsulated in silica sol gels were compared to that of the sensors in solution. The promising results show that the sol gel matrix does not adversely affect the sensing properties of the newly developed luminescence based oxygen sensors.

References – Chapter 1

1. J. Lakowicz. “Principles of Fluorescence Spectroscopy.” 2nd ed.; KluwerAcademic/Plenum Publishers: New York, 1999.
2. Y, Feldstein. Some problems concerning the morphology of auroras and magnetic disturbances at high latitudes. *Geomagnetism and Aeronomy*. **1963**, 3, 183–192
3. Y, Feldstein. A Quarter Century with the Auroral Oval. *EOS*. **1986**, 67
4. J, Hastings. Biological diversity, chemical mechanisms, and the evolutionary origins of bioluminescent systems. *J. Mol. Evol.* **1983**, 19, 309–21
5. E. Harvey; “A History of Luminescence From the Earliest Times Until 1900.” American Philosophical Society, **1957**
6. Encyclopædia Britannica. “Luminescence.” *Encyclopædia Britannica Online*. Encyclopædia Britannica Inc., **2012**. Web. 18 Apr. 2012
7. L, Goss; A, Smith; M, Post. Surface thermometry by laser-induced fluorescence. *Review of Scientific Instruments*. **1989**, 60, 3702–3706

8. J. Lakowicz. "Principles of Fluorescence Spectroscopy." 3rd ed.; Springer. **2006**
9. D, Fink; H, Beaty. *Standard Handbook for Electrical Engineers, Eleventh Edition*, McGraw-Hill, New York, **1978**
10. M. Lippititsch; J. Pusterhofer; M. Leiner; O. Wolfbeis. "Fibre-Optic Oxygen Sensor With the Fluorescence Decay Time as the Information Carrier." *Analytica Chimica Acta*. **1988**, 205, 1-6
11. de Silva, A.; Gunaratne, H.; Gunnlaugsson, T.; Huxley, A.; McCoy, C.; Rademacher, J.; Rice, T. *Chem. Rev.* **1997**, 97, 1515-1566.
12. B. Valeur; I. Leray. "Design principles of fluorescent molecular sensors for cation recognition." *Coordination Chemistry Reviews*. **2000**, 205, 3-40
13. S, Haron; A, Ray. Optical biodetection of cadmium and lead ions in water. *Medical Engineering and Physics*, **2006**, 28, 978-981.

Chapter 2: Oxygen Sensing

General Background

Oxygen is the third most abundant element in our universe, it makes up two thirds of our planet's atmosphere, and accounts for half of the mass of the Earth's crust.¹ As abundant as oxygen is on our planet, free oxygen is too chemically reactive to remain present without constant replenishment by photosynthesis.²

Not only is oxygen plentiful in our surroundings, but it is also a substantial part of the physical make up of living organisms. For example, oxygen accounts for up to 65% of the mass of the human body.³ This is largely due to the oxygen content in water.

As well as being extremely abundant, oxygen also plays an essential role in many biological, engineering, and manufacturing processes. For example, molecular oxygen is required to convert nutrients into energy during the cellular respiration process. Oxygen is also used in the production of steel, plastics, and various other products. Further, oxygen is used in such applications as water treatment processes and life support apparatuses.¹

As abundant as oxygen is on our planet and as vital a role as the element plays in our daily lives, it's not surprising that accurately and reliably monitoring the amounts of free oxygen is often of great importance.

Oxygen sensors provide a means to monitor oxygen concentrations and/or partial pressures in a vast and dynamic range of biological, engineering, and manufacturing applications. A few of the many uses of oxygen sensors are: monitoring the partial pressure of oxygen in patients' blood, measuring dissolved oxygen content in fish farming ponds, determining levels of oxygen in packaged produce, and monitoring oxygen in combustion reactions.⁴

Traditional Oxygen Sensing Methodology

Oxygen sensing techniques have been greatly investigated over the years. One of the earliest methods of determining oxygen concentrations was developed in 1888 by Ludwig Winkler.⁵ In this method, the dissolved oxygen concentration in water is measured using the following procedure. The first step is the formation of a manganese (II) precipitate in the water sample. Next, the manganese (II) precipitate is oxidized by the dissolved oxygen in the water sample. This is followed by an oxidation of iodide in the sample by the oxidized manganese (III). Finally, the iodine is titrated with a known standard; the concentration of dissolved oxygen in the water sample is proportional to the titrated iodine.⁵⁻⁶

The major drawback to the Winkler method is the length of time required to make the measurements. Also, any addition of oxygen from the outside or escape of oxygen from the sample will produce error in the measurement. As a result, the Winkler method is a very time consuming and tedious technique that is not used as frequently as it once was.⁷

While currently the Winkler method is mainly used as a calibration for other oxygen sensing instruments, the vast majority of oxygen sensing techniques over the last fifty years have been based on the Clark type electrode.⁶⁻⁷ The Clark electrode is named after Dr. Leland Clark who, in 1956, developed an apparatus for measuring the partial pressure of oxygen in blood.⁸⁻⁹

In Clark's experiment, oxygen was reduced at the surface of a cellophane covered platinum electrode under proper applied voltage. The resulting current, produced from the reduction of oxygen, was proportional to the partial pressure of oxygen in the system. The cellophane covering the platinum electrode allowed oxygen diffusion through the covering but prevented the blood from coming in direct contact with the electrode.

Since Clark's first study there have been several works in which modifications to the polarographic technique have been made. Such works

explored using a variety of different materials for the cathode and anode. As well, there has been various electrode arrangements and setups also reported.¹⁰⁻¹¹

While the Clark method of oxygen sensing is a very mature approach and still highly used technique, there are many limitations to this method. One such problem with the Clark method is caused by the buildup of the reactants at the counter electrode.¹² This buildup affects the operation of the system and, over time, could result in a complete halt in oxygen reduction at the cathode. In addition, the reduction reaction can cause a shift in pH to occur over time.¹²⁻¹³ Further, the electrodes also are limited to small sampling regions and their intrusion disturbs the local environment being investigated.¹³ Other disadvantages of the polarographic technique are that oxygen sensors of this nature tend to drift after calibration, consume oxygen, are ineffective at low temperature and low oxygen concentrations, and can be highly unstable.¹²⁻¹⁵

Luminescence based oxygen sensors provide an alternative approach of measuring oxygen concentration and/or oxygen partial pressure, without the many drawbacks encountered with the more traditional oxygen sensing techniques. Some of the advantages of luminescence based oxygen sensors are: they do not consume oxygen, they are highly stable, sensitive, selective,

and also provide remote sensing capability.¹⁴⁻¹⁵ Because of the many advantages of luminescence based oxygen sensors over the more traditional oxygen sensing methods, research into and the application of luminescence based oxygen sensors have increased dramatically over the years.¹⁵ Luminescence based oxygen sensors will be explored in greater detail in subsequent chapters.

References – Chapter 2

1. M, Dole. The Natural History of Oxygen., The Journal of General Physiology., **1965**, 5-27
2. M, Weeks. The discovery of the elements. IV. Three important gases. J. Chem. Educ., **1932**, 9, 215
3. E, Frieden. The Chemical Elements of Life. Scientific American. **1972**, 52-60
4. R. Ramamoorthy; P. Dutta; S. Akbar. “Oxygen sensors: Materials, methods, designs and applications.” Journal of Materials Science. **2003**, 38, 4271 - 4282
5. C. Oudot; R. Gerard; P. Morin; I. Gningue. “Precise Shipboard Determination of Dissolved Oxygen (Winkler Procedure) for Productivity Studies with a Commercial System. American Society of Limnology and Oceanography. **1988**, 33, 146 – 150
6. C, Numako; I, Nakai. XAFS studies of some precipitation and coloration reaction used in analytical chemistry. Physica B: Condensed Matter. **1995**, 208–209: 387–388

7. M. Berntsson; A. Tengberg; P. Hall; M. Josefson. "Multivariate experimental methodology applied to the calibration of a Clark type oxygen sensor." *Analytica Chimica ACTA*. **1997**, 355, 43 - 53
8. J. Severinghaus; P. Astrup. History of blood gas analysis. IV. Leland Clark's oxygen electrode. *Journal of clinical monitoring*. **1986**, 2, 125–39
9. L. Clark; R. Wolf; D. Granger; Z. Taylor. "Continuous Recording of Blood Oxygen Tensions by Polarography." *Journal of Applied Physiology*. **1953**, Volume 6, p 189
10. I. Fatt. "An ultramicro oxygen electrode." *Journal of Applied Physiology*. 1964
11. I. Fatt; R. Helen. "A multicathode polarographic oxygen sensor and its performance." *Journal of Applied Physiology*. 1969, Vol. 27
12. W. Rumsey; J. Vanderkooi; D. Wilson. "Imaging of Phosphorescence: A Novel Method for Measuring Oxygen Distribution in Perfused Tissue." *American Association for the Advancement of Science*. **1988**, Vol. 241, pp. 1649 – 1651

13. S. Gatti; T. Brey; W. Muller; O. Heilmayer; G. Holst. "Oxygen microoptodes: a new tool for oxygen measurements in aquatic ecology." *Marine Biology*. **2002**
14. M. Lippititsch; J. Pusterhofer; M. Leiner; O. Wolfbeis. "Fibre-Optic Oxygen Sensor With the Fluorescence Decay Time as the Information Carrier." *Analytica Chimica Acta*. **1988**, 205, 1-6
15. de Silva, A.; Gunaratne, H.; Gunnlaugsson, T.; Huxley, A.; McCoy, C.; Rademacher, J.; Rice, T. *Chem. Rev.* **1997**, 97, 1515-1566.

Chapter 3: Luminescence

Fluorescence and Phosphorescence

Luminescence occurs when a substance radiatively transitions from an electronically excited state to a lower energy state. Luminescence can be divided into two main categories of fluorescence and phosphorescence. Fluorescence is the emission of light due to a spin-allowed transition from an excited state to a lower state. Fluorescence is fast and typically has lifetimes on the order of a few nanoseconds. Phosphorescence, on the other hand, is the emission of light due to a formally spin-forbidden process and is a much slower process than fluorescence. The forbidden nature of its transition, results in phosphorescence having much longer lifetimes than fluorescence (microseconds to minutes).¹

A simplified version of a Jablonski diagram for a molecule or atom of a photoluminescent substance is shown in Figure 1. This figure gives a simple illustration of the main processes following excitation and leading to luminescence.

The three energy states S_0 , S_1 , and S_2 are singlet states. Consider that after absorbing electromagnetic radiation in the form of a photon, the luminophore is excited from the ground state, S_0 , to a higher energy state, S_2 .

The luminophore then rapidly and efficiently relaxes to the lowest excited state, S_1 . This process is known as internal conversion.

Once in the lowest excited state, S_1 , the luminophore can undergo one of several processes. It may radiatively decay to the ground state, emitting light in the form of fluorescence. The luminophore may also undergo a formally spin-forbidden change of state, known as intersystem crossing, to the lower energy triplet state T_1 . Once in the excited T_1 state, the luminophore may emit light in the form of phosphorescence as it radiatively decays back to the singlet ground state. Lastly, S_1 or T_1 can also nonradiatively relax back to the ground state via vibrations, collisions, or rotations.

The rate of transition from the excited state S_1 back to the ground state S_0 depends upon both the luminophore and its surroundings. The lifetime of the S_1 state is the average time the luminophore spends in the excited state. The lifetime of the luminophore is the reciprocal of the sum of all the rate constants that deplete the excited S_1 state and is given by equation 1

$$\tau = \frac{1}{k_{nr} + k_r} \quad (1)$$

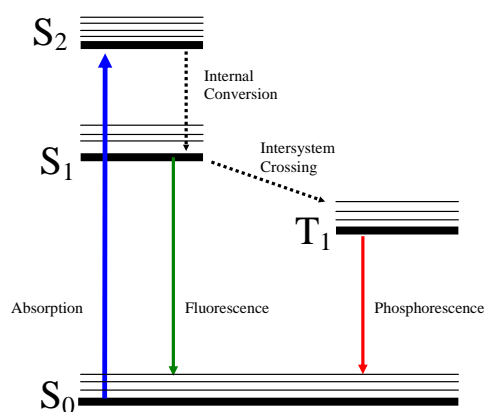


Figure 1. ...Simplified Jablonski diagram showing several key luminescence processes.

where τ is the lifetime, k_{nr} is the nonradiative rate constant, and k_r is the radiative rate constant. In the case of equation 1, k_{nr} represents the sum of all nonradiative rate constants that deplete the S₁ state.

The luminescence quantum yield, Φ , is the ratio of the number of emitted photons to the number of photons absorbed and is given by

$$\Phi = \frac{k_r}{k_{nr} + k_r} \quad (2)$$

The quantum yield of a luminophore is also related to the luminescence lifetime by

$$\Phi = \tau k_r \quad (3)$$

As evident by equation 2, the quantum yield of a luminophore is always less than unity due to nonradiative processes.¹ The closer the quantum yield is to unity, the more efficient the luminophore.

When designing a luminescence based sensor, it is desirable to have a large luminescence quantum yield and long lifetimes. High quantum yields increases the amount of signal obtainable and therefore increases the signal to noise ratio. Also, the longer the lifetime of the luminophore, the more opportunities it has to interact with the analyte being examined therefore increasing its sensitivity.

Intensity vs. Lifetime Measurements

Many luminescence based sensors operate by monitoring the response of either the emission intensity or the luminescence lifetime of a luminophore to changes in the analyte being examined. Lifetime measurements have the advantage over intensity measurements in that the luminescence lifetime is independent of sensor concentration, light source intensity fluctuations, detector instability, detector spectral response, scattering, or sample orientation.² These factors can cause errors in the observed emission intensity, but will have no effect on the lifetime.

Luminescence lifetime measurements may be made in one of two ways, pulsed lifetime measurements or phase shift lifetime measurements. Phase shift measurements have the advantage that their instrumentation is relatively inexpensive and simple in design. However, simple phase shift instruments are incapable of evaluating complex decays and give little to no warning of improper system operations.

With phase shift measurements, the sample is pumped with a periodic sinusoidal excitation source. The resulting luminescence will have the same frequency as the exciting light but with a measurable delay, the phase shift. Also, the degree of modulation (demodulation) of the emission will be lower than for the excitation. The phase shift and amount of demodulation of the emission intensity can be used to calculate an observed lifetime for the sample.

Traditionally, phase shift measurements are made at a single frequency. To measure complex decays such as sums of exponentials, a series of measurements have to be made at different frequencies. Sarah Payne in a recent work demonstrated a phase shift instrument capable of measuring complex exponential decays in a single experiment.³ In her study the excitation contained a grid of frequencies instead of a single frequency. Various distinct lifetimes were obtained with a single measurement. Payne's

device, however, is not a simple phase shift instrument. Information such as multiple lifetime components and the presence of impurities are not obtainable by use of simple phase shift lifetime measurements; however, pulsed lifetime measurements do not incur such problems.

In pulsed lifetime measurements, short pulses of light are used to pump the sample. The absorbed photons excite a finite number of luminophores to an upper excited level. The emission intensity, which is proportional to the number of excited luminophores, will decay as follows

$$I_t = I_0 e^{-t/\tau} \quad (4)$$

where t is time, I_t is the intensity at time t , and I_0 is the intensity at $t = 0$. An appropriate decay model is then chosen and the lifetime is determined by a nonlinear least square fitting of the time dependent intensity data. For single exponential decays the lifetime and preexponential factor are the only adjustable parameters. More complex decays may be evaluated using multiple pre-exponential weighted lifetimes. In doing so each lifetime parameter is weighted based on its contribution to the total decay.¹

Pulsed lifetime measurements require instrumentation with fast electronics. This is the major reason why pulsed lifetime instrumentation is considerably more expensive than phase shift. Pulsed lifetime measurements

however provide a method of evaluating complex multi-exponential decays that simple single frequency phase shift measurements cannot. Also while performing pulsed lifetime measurements, the luminescence decay profile is on hand. This gives the user the opportunity to see when the system may not be operating properly.

Finally, both intensity and lifetime measurements require a means of detecting the luminescence. Photomultiplier tubes, PMTs, are the luminescence detectors utilized in all instrumentation used in this work. The key elements to the operation of PMTs are the photocathode, dynodes, and anode. The inside of the PMT is held at a very high vacuum. A window in the PMT housing is designed such that incident photons will strike the negatively charged photocathode located inside the vacuum tube. When photons strike the photocathode, photoelectrons are generated. A string of positively charged dynodes are positioned in series behind the photocathode. The positive charge on the first dynode causes the generated photoelectrons to accelerate to it. When the photoelectrons strike the first dynode several secondary electrons are produced. Relative to the first dynode, the second dynode is held at a more positive potential. As a result the secondary electrons produced at the first dynode stage are accelerated to the next dynode. Each consecutive dynode is held at a more positive potential than

the preceding one. The number of secondary electrons produced continually increases as the electrons are accelerated through the series of dynodes. The number of dynode stages determines the number of electrons generated. Typically, more than one million electrons are produced for every photon incident at the PMT window. Finally, the secondary electrons are collected by the anode. The result is the generation of a large pulse of electrons for every photon detected.⁴

Ru(II) Transition Metal Complexes

The lifetime of the luminophore is one of the most critical aspects that must be considered when designing a luminescence based sensor. The long lifetimes of transition metal complexes (TMCs) are, in part, the reason why they are attractive as luminescence probes. TMCs can have lifetimes that range from hundreds of nanoseconds to 10s of microseconds. Other advantages of transition metal complexes include their strong visible absorptions and relatively high quantum yields. Further, the use of TMCs with their broad intense absorptions allows for a wide selection of excitation sources as well as the use of minimum amounts of the metal complex when devising a luminescence based sensor.^{2,5}

Transition metals and their complexes are characterized by their partially filled d orbitals.⁶ This work focuses on octahedral d^6 TMCs, in particular Ru(II)L_3 complexes, where L is a bidentate ligand. There are six d electrons residing in five d orbitals of the metal ion and each ligand coordinates to two of the six octahedral coordination sites of the TMC.

When ligands are positioned on the six coordination sites of the octahedral transition metal complex the electrostatic interaction between the filled valence electrons in the ligands and the six d electrons will cause a splitting in the energy of the five d orbitals. The two d orbitals centered on the coordinate axes will be closer to the ligands than the three d orbitals that lie between axes. Thus the electrostatic repulsion will cause the closer d orbitals to have a higher energy than those further away. The resulting upper energy level, e_g , is doubly degenerate, while the lower energy level, t_{2g} , is triply degenerate.

The crystal field splitting parameter, Δ , splits the e_g and the t_{2g} energy levels with the magnitude depending upon the interaction between the metal and the coordinating ligands. The stronger the interaction, the greater the splitting. When Δ is small electrons in the 5 d orbitals will spread out, occupying both e_g and the t_{2g} levels. Conversely, when Δ is large it is more energetically favorable to fill the lower lying t_{2g} energy level first. A d^6 TMC

with a large Δ results in a ground state with a completely filled t_{2g} level and an empty e_g ,^{2,5} such is the case with the Ru(II) TMCs in this work.

The energy levels associated with the ligands of the Ru(II)L₃ TMCs studied remain mostly unchanged after coordination.^{2,5} The ligands have completely filled bonding π orbitals and empty antibonding π^* orbitals.

The ground state and excited states of TMCs are determined by the metal and the coordinating ligands. The electrons in the ground state of the Ru(II)L₃ TMCs are all paired, resulting in a singlet ground state. The excited states depend on the type of electron transitions.

The three possible electron transitions in TMCs are: d-d transitions which are centered on the metal, π - π^* transitions which are localized on the ligand, and charge transfer, CT, transitions which involve the promotion of an electron from a d orbital to a π orbital or vice-versa. d-d states are long-lived, essentially non-luminescent, and frequently photochemically unstable. Since emission always occurs from the lowest excited state, it is essential for the stability and good quantum yield of the luminescence sensor that the d-d state be sufficiently higher than the lowest excited state.

The transition of most significance in the TMCs studied in this work is that from the CT excited state. There are two types of CT states in a TMC,

metal to ligand charge transfer, MLCT, and ligand to metal charge transfer, LMCT. The MLCT state occurs when an electron is promoted from a d orbital of the metal to a π orbital of the ligand. The MLCT is the lowest excited state of the Ru(II) complexes studied in this work and thus the emitting state.

The ground state and excited states described above are shown in Figure 2. As mentioned, the ground state is singlet. The triplet excited states result from the large degree of spin-orbit coupling between the promoted electron's spin and its orbital angular momentum.

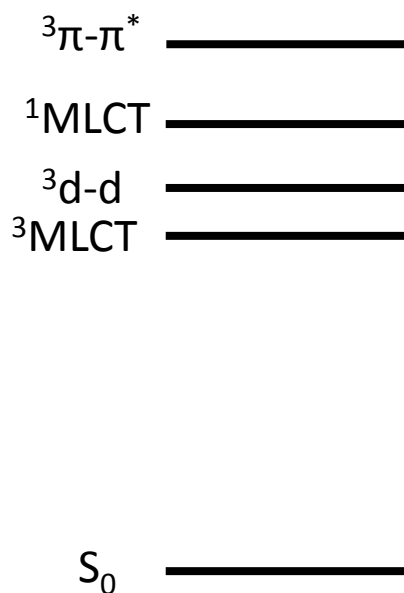


Figure 2. Simplified orbital diagram of the lower states for the two d^6 Ru(II) TMCs with octahedral molecular geometry.

Transition metals such as ruthenium, osmium, rhodium, and rhenium form the basis of many luminescent TMCs.⁵ Of the luminescent TMCs, perhaps the most studied and most interesting are the Ru(II) complexes. They are extremely versatile, photochemically stable, and have very efficient emissions. Further, their emitting state energies and excited state redox properties can be exquisitely sensitive by variations in the metal, coordinating ligands, and local environment.⁵ The structure of the two luminescent Ru(II) TMCs used in this study, tris-(4,7-diphenyl-1,10-phenanthroline) ruthenium(II) dichloride, $[\text{Ru}(\text{dpp})_3]^{2+}\text{Cl}_2$, and tris-(2,2'-bipyridine)ruthenium(II) dichloride, $[\text{Ru}(\text{bpy})_3]^{2+}\text{Cl}_2$ are shown in Figure 3. The design and applications of these two Ru(II) TMCs as luminescence sensors has been well explored, particularly due to their ability to report on the presence of oxygen.^{2,5}

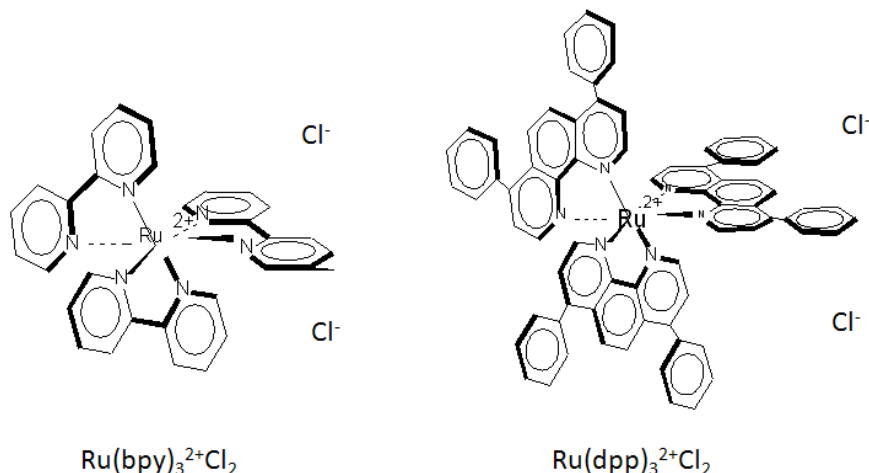


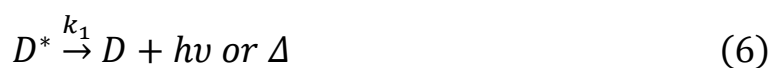
Figure 3. Structures of the two transition metal complexes (TMCs) used in this study, tris-(4,7-diphenyl-1,10-phenanthroline) ruthenium(II) dichloride ($Ru(dpp)_3Cl_2$) and tris-(2,2'-bipyridine)ruthenium(II) dichloride ($Ru(bpy)_3Cl_2$).

Luminescence Based Oxygen Sensing

Quenching is an important aspect of luminescence based sensor design and application. Depending on the probe and its application, quenching can adversely affect the operation of a luminescence based sensor or, as in the case of this study, be a useful tool in its performance. The luminescence based oxygen sensors developed in this work operate by monitoring the quenching of the Ru(II) TMCs' luminescence by oxygen. Both the intensity and lifetime of luminescence of the two Ru(II) complexes used in this study change predictably and reproducibly in the presence of

oxygen, making these complexes ideal for reporting on the presence of oxygen.

The excitation and subsequent deactivation by oxygen of the Ru(II) TMCs is described by the following equations



where D is the luminescent Ru(II) TMC, $h\nu$ represents a photon, D^* is the excited luminophore, k_1 is the sum of the radiative and nonradiative rate constants, Δ is nonradiative energy, O_2 is diatomic oxygen, and k_q is the bimolecular quenching rate constant. After absorbing energy in the form of a photon, the Ru(II) TMC is excited from the ground state to a higher energy state as shown in equation 5. The luminophore then rapidly relaxes to the lowest excited, MLCT, state via internal conversion. In the absence of oxygen the luminophore either radiatively or nonradiatively decays back to the ground state as described in equation 6. If oxygen is present, collisions between oxygen and the Ru(II) TMC may occur resulting in the deactivation of the excited MLCT state by oxygen quenching as described in equation 7.

Quenching is defined by Lakowicz as any process that decreases the luminescence intensity¹. There are two general types of quenching. In the first form of quenching, static quenching, the luminescent material generally forms a non-luminescent material. This type of quenching is not present in the oxygen sensors studied in this work. The more common form of oxygen quenching, dynamic quenching, occurs when the quenching molecule collides with an excited luminophore as described above. Upon collision, the excited luminophore can be deactivated by the quencher. This returns the luminophore to the ground state before it's able to emit a photon. Therefore the longer the lifetime of the luminophore, the greater the distance the quencher can travel and still collide with an excite luminophore molecule.

Quenching of the luminescence of the Ru(II) TMCs can be used as an analytical tool for the determination of the concentration of oxygen. As the concentration of oxygen increases, the probability for collisions between oxygen and Ru(II) TMC increase; as a result, both lifetime and intensity decrease with increasing oxygen concentration. The quenching of the luminescence lifetime and intensity as a function of oxygen concentration is given by the well-known Stern-Volmer equation as follows

$$\frac{\tau_0}{\tau} = \frac{I_0}{I} = 1 + K_{SV}[O_2] \quad (8)$$

where τ_0 is the lifetime of the MLCT state in the absence of oxygen (also known as the unquenched lifetime), τ is the measured lifetime, I_0 is the luminescence intensity in the absence of oxygen, I is the measured luminescence intensity, K_{SV} is the Stern-Volmer quenching constant, and $[O_2]$ is the oxygen concentration. The evaluation of the degree of quenching of the Ru(II) TMC's luminescence by oxygen allows for the determination of oxygen.

Most luminescence based oxygen sensors operate by such method. This luminescence based oxygen sensing method has many advantages over traditional oxygen sensors, as discussed in Chapter 2. However there are still problems associated with the practical application of such sensors. For example, intensity method luminescence sensing is subject to many errors such as source fluctuation, detector drift, geometry changes, and photodecomposition as mentioned previously. To rectify some of these errors an internal reference is often incorporated in the luminescence sensor instrumentation. This is accomplished by using a reference luminescent dye that has an emission spectrum dissimilar to the sensing probe and is not affected by the analyte under investigation.

Luminescence sensors utilizing lifetime measurements on the other hand are inherently self-referencing and are largely unaffected by the perturbations that affect intensity based measurements. These sensors are, however, influenced by changes in lifetime due to both temperature and pressure. Further, many lifetime instruments are phase shift based, because of the low cost and modest size associated with the instrumentation. As discussed, simple phase shift instruments calculate lifetime from a single phase shift at one frequency, with no other information delivered by the system. As a result, there is little warning of flawed instrumentation or response.

References – Chapter 3

1. J. Lakowicz. "Principles of Fluorescence Spectroscopy." 2nd ed.; KluwerAcademic/Plenum Publishers: New York, **1999**.
2. J. Demas; B. DeGraff. "Applications of Luminescent Transition Metal Complexes to Sensor technology and Molecular Probes." Journal of Chemical Education. **1997**, 690-95
3. Payne, Sarah J. M. "Advances in Luminescence Sensors, Techniques, and Instrumentation," Ph. D. Dissertation, University of Virginia, Charlottesville, VA, 2010.
4. V, Zworykin; G, Morton; L, Malter. The Secondary Emission Multiplier-A New Electronic Device. Proceedings of the IRE. **1936**, 24, 351
5. J. Demas; B. DeGraff. "Applications of luminescent transition platinum group metal complexes to sensor technology and molecular probes." Coordination Chemistry Reviews. 211, **2001**, 317-351
6. D. Oxtoby; N. Nachtrieb. "Principles of Modern Chemistry." Third Edition. Saunders College Publishing. **1996**, 604-634

Chapter 4: Development of Luminescence Lifetime Standards

Introduction

In developing luminescence based oxygen sensors, as with any technology, it is important for practical applications purposes as well as fundamental comprehension of the science involved, that the response of the system under different conditions is understood. A condition that could very easily vary considerably from user to user is temperature. For example, the temperature of the Honey Island swamp in Louisiana, the temperature inside the University of Virginia Medical Center, and the temperature of the Rocky Mountains' Cucharas River are not only different from each other but will most likely differ with time. As a result, measurements taken under one condition may not accurately reflect the behavior of the system at another.

It is known that luminescence lifetimes have a strong temperature dependence, hence in order to be a practical and effective analytical tool, how luminescence based sensors will behave under such varying conditions for different users must be understood. The goal of this experiment has been to develop a method of rapidly and accurately determining the temperature dependence of luminescence lifetimes in a series of ruthenium-based complexes. Studying the temperature dependence of these luminescence lifetimes allows for a better understanding of the photo-physics involved in

the molecular processes of luminescence based sensors as well as gives insight into the function and design of such sensors. With luminescence based sensors becoming increasingly important in the industrial, environmental, biological, and health areas,¹⁻¹⁹ the understanding of these sensors is critical.

Many luminescence sensor systems are based on luminescent transition metal complexes.^{1-8, 12-18} Both intensity and lifetime methods are used. Intensity methods are subject to errors from source fluctuation, detector drift, geometry changes, and photodecomposition.¹⁹ To alleviate these problems, internal standards that have different emission spectra that are not affected by the analyte can be incorporated. In contrast, lifetime approaches have the advantage that they are inherently self-referencing. The lifetime directly provides the desired information and is largely independent of the perturbations that affect intensity methods. Lifetime methods have become increasingly popular, but at present low cost lifetime instrumentation is phase shift based and limited to lifetimes greater than 100 ns. This largely limits their use to systems based on metal complexes such as platinum metals (Ru, Ir, Os, and Pt).

The popularity of luminescent platinum metal complexes rest on their long-lived excited states coupled with strong visible absorptions which aid

in sensor design. Their lifetimes and spectral characteristics are generally well suited for low cost LED based phase shift instrumentation. The primary disadvantage of phase shift instruments is that they generally provide only a single phase shift at one frequency, which allows calculation of a lifetime. However, since complete decays are not available for examination, there is little warning of instrument malfunction.

Using a series of fluorophores in liquid solution at 20°C, a group of 9 independent laboratories developed a set of lifetime standards with lifetimes ranging from 89 ps to 31.2 ns.²⁰ A set of 20 fluorescence lifetime standard/solvent combinations was compiled. These standards should prove extremely useful in the testing and calibration of fluorescence lifetime instruments such as Fluorescence Lifetime Imaging Microscopy (FLIM) where the lifetime of the most commonly used fluorophores are a few nanoseconds or less. These standards would be useless however in calibrating metal complex based sensors, due to the long-lived excited states of metal complexes. Lakowicz reported a few lifetime standards for this class of molecules, but it was not comprehensive.²¹ Further, there is also a practical need for standards that are not limited to laboratory conditions where temperature and oxygen pressure can be easily controlled but are applicable over a wide range of temperatures and oxygen pressure. It would

therefore be useful to have a set of standards that could be used to rapidly check the performance of instruments both in the laboratory and under the much more extreme condition of field or plant work. Also, in spite of the wide use of these systems, there is still little detailed fundamental information on such things as the temperature dependence of quenching.

We wished to develop a simple method for determining the temperature and oxygen quenching properties of metal complexes. Exploiting this technology, we wanted to develop a set of reliable standards that could be used to calibrate phase shift and pulsed lifetime based instruments. Our systems were optimized for use with platinum metal complexes having lifetimes in the 0.1-6 μs range. Further, the standards should be usable over a wide range of temperatures and air pressures so that they could be used to check the operation of instrumentation under a variety of field conditions. Finally, we wanted to develop models that would allow precise descriptions of the pressure and temperature dependences of luminescent complexes.

Materials: Our samples consisted of one of two Ru(II) metal complexes in a several analytical grade solvents. The ruthenium complex tris-(4,7-diphenyl-1,10-phenanthroline)ruthenium(II) dichloride, $[\text{Ru}(\text{dpp})_3]\text{Cl}_2$, was from GFS Chemicals Inc. while the second complex,

tris-(2,2'-bipyridine)ruthenium(II) dichloride, $\text{Ru}(\text{bpy})_3\text{Cl}_2$, was synthesized by standard method as referenced,²² but it is also available from GFS Chemicals and others. The solvents chosen for this experiment were ethylene glycol (Sigma-Aldrich or Fisher Scientific), glycerol (Aldrich), and double distilled water. Because of its low solubility $\text{Ru}(\text{dpp})_3\text{Cl}_2$ was not measured in water. The sample concentrations for these experiments were approximately 45 μM for $\text{Ru}(\text{bpy})_3\text{Cl}_2$ in ethylene glycol, 18. μM solution $\text{Ru}(\text{bpy})_3\text{Cl}_2$ in water, 40 μM solution of $\text{Ru}(\text{bpy})_3\text{Cl}_2$ in glycerol, and 10 μM solution of $\text{Ru}(\text{dpp})_3\text{Cl}_2$ in ethylene glycol.

Experimental Setup: The experimental setup used is shown in Figure 1. Samples were excited with a short, 3 ns, pulse from a N_2 laser (Laser Science, VSL 337). A saturated, approximately 1 cm thick, CuSO_4 solution was placed at the output of the N_2 laser to remove plasma emissions. The beam was focused onto the sample and a Hamamatsu R928 photomultiplier tube was used to detect the luminescence. A complementary red pass filter was used over the PMT to eliminate scattered excitation light. The photomultiplier output was recorded on a digital oscilloscope (Tektronix TDS 2022 Two Channel Storage Oscilloscope, 200 MHz, 2GS/sec) interfaced to a desktop PC through an IEEE 488 interface. A 50 Ω load resistor was used. Sample temperature was monitored with a thermocouple

(Type T, Omega Engineering, Inc.) that was immersed directly in the sample. An electronic cold junction compensator was used. The voltage was read with a Keithley 2000 digital multimeter interfaced to the PC through an IEEE 488. The samples were placed in a well-stirred water bath heated with a Variac controlled immersion heater. The sample was first cooled below 10° C and then heated at approximately 0.5 °C/min to collect data.

During data collection, the well-stirred sample was sparged with compressed N₂, air, or O₂ gas bubbled directly into the sample with a frit to maintain the equilibrium oxygen concentration during the measurement. For water solutions, the gas was water saturated by using a bubbler to minimize evaporation. Glycol and glycerol have negligible vapor pressure and evaporation was not an issue.

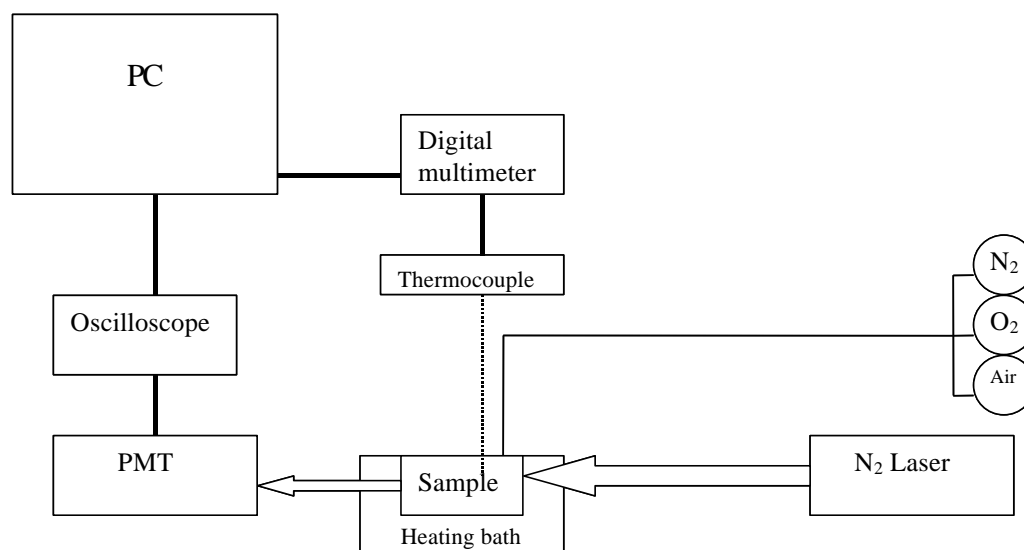


Figure 1: Schematic diagram of experimental setup.

Experimental Procedure: The lifetimes of our Ru(II) complexes, in a variety of solutions, were measured at different temperatures. Separate measurements under nitrogen, oxygen, and air were performed. Solutions were bubbled, with the respective gas, for at least 40 minutes to allow the systems to equilibrate. After a sufficient equilibrium time, the sample was immersed in an ice bath and cooled to less than approximately 8 °C. The sample was allowed several minutes to stabilize at this low temperature and then the temperature was slowly raised. Starting at a predetermined

temperature (typically 10 °C), a decay curve was collected at every 0.5°C. At each temperature, 100 decays were collected and averaged. The oscilloscope does not average except at 8-bit resolution so, to exploit the enhanced resolution of averaging, each decay was transferred to the computer and averaged in software. This has the advantage of allowing each transient to be analyzed and to reject large pulses that saturated the ADC. Each temperature and its corresponding averaged decay curve were saved in separate LabView files. Finally, once the temperature reached 50 °C, the experiment was terminated. The sample was cooled and the next gas was bubbled through the solution.

Each decay curve was fit by nonlinear least squares in Labview. All the decays were single exponential. A complete data set for each sample consisted of decay times versus temperature for each of the three oxygen concentrations.

The nonlinear models for fitting the oxygen temperature dependence of the lifetimes (see below) were fit by nonlinear least squares using PSI Plot (Poly Software International) or a MathCAD routine.

Results and Discussion

The model used for interpreting the temperature dependence is shown in Figure 2 where k_r is the radiative rate constant, k_{nr} is the non-radiative rate constant, and k_{dd} is the rate constant for thermally activated quenching via the nonluminescent d-d state. This model adopts the accepted temperature dependence for thermal deactivation of the emitting MLCT state via a non-luminescent d-d excited state. The lifetime of the MLCT state, in nitrogen, air, and oxygen, is given by

$$\tau_0 = 1/(k_0 + k_{dd}) \quad (1)$$

$$\tau_{\text{air}} = 1/(k_0 + k_{dd} + k_2[\text{O}_2]) \quad (2)$$

$$\tau_{\text{oxygen}} = 1/(k_0 + k_{dd} + k_2[\text{O}_2]) \quad (3)$$

$$k_0 = k_{nr} + k_r \quad (4)$$

$$k_{dd} = A \cdot \exp(-\Delta E/kT) \quad (5)$$

$$[\text{O}_2] = K_h P_{\text{oxygen}} \quad (6)$$

where τ_0 is the lifetime in nitrogen purged samples and, therefore, in the absence of a bimolecular quencher, k_0 is the sum of the radiative and non-radiative rate constants, τ_{air} is the lifetime in air purged samples, k_2 is the

bimolecular quenching rate constant, $[O_2]$ is the quencher concentration, K_h is the Henry's Law constant for oxygen solubility, and P is the oxygen pressure. τ_{oxygen} is the lifetime in oxygen purged samples, A is a pre-exponential factor, ΔE is the energy difference between the emitting charge transfer state and the thermally populated d-d state, k is the Boltzmann constant, and T is temperature. k_2 and k_{dd} are assumed to be the only temperature dependent parameters in our model.

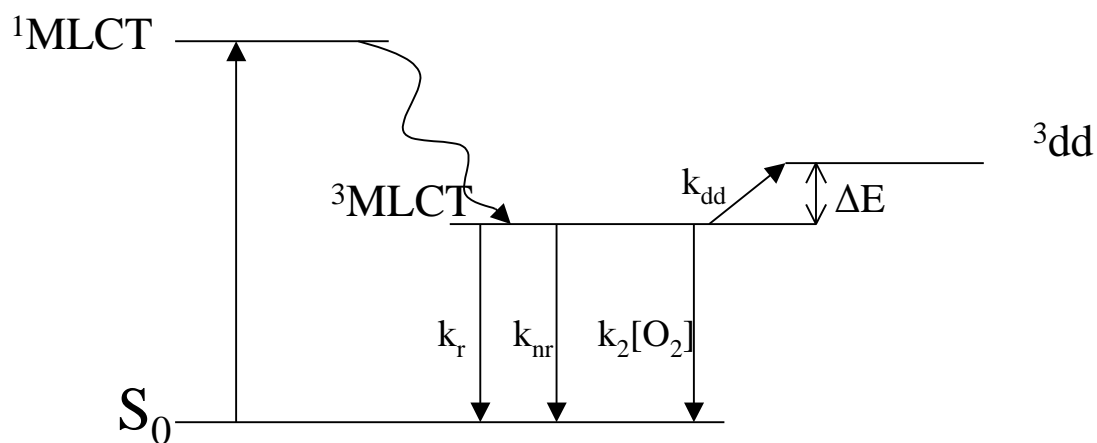


Figure 2: Lifetime temperature dependence model.

Figures 3 and 4 show the lifetime temperature and oxygen pressure dependence of $\text{Ru}(\text{bpy})_3\text{Cl}_2$ in water and $\text{Ru}(\text{dpp})_3\text{Cl}_2$ in ethylene glycol respectively. The dots are data points, while the solid black lines represent the fit to the model described below. As expected by the thermally activated decay path, the lifetime decreases as the temperature is raised. Oxygen quenching is also pronounced except for the very viscous glycerol but even there the lifetime of $\text{Ru}(\text{dpp})_3^{2+}$ is long enough to give noticeable quenching especially at higher temperatures where the viscosity is lower.

Since oxygen is a dynamic quencher of the luminescence lifetime, we can describe the quenching at each temperature with a Stern-Volmer equation.

$$\tau_0/\tau = 1 + K_{\text{svp}}P_{\text{oxygen}} = 1 + K_{\text{sv}}K_{\text{h}}P_{\text{oxygen}} \quad (7)$$

$$K_{\text{sv}} = k_2 \cdot \tau_0 \quad (8)$$

where τ is the measured lifetime, K_{sv} is the Stern-Volmer quenching constant, and K_{svp} is a pressure based Stern-Volmer constant. The lifetime at each oxygen pressure and temperature is given by

$$\tau = \tau_0 / (1 + K_{\text{svp}}P_{\text{oxygen}}) \quad (9)$$

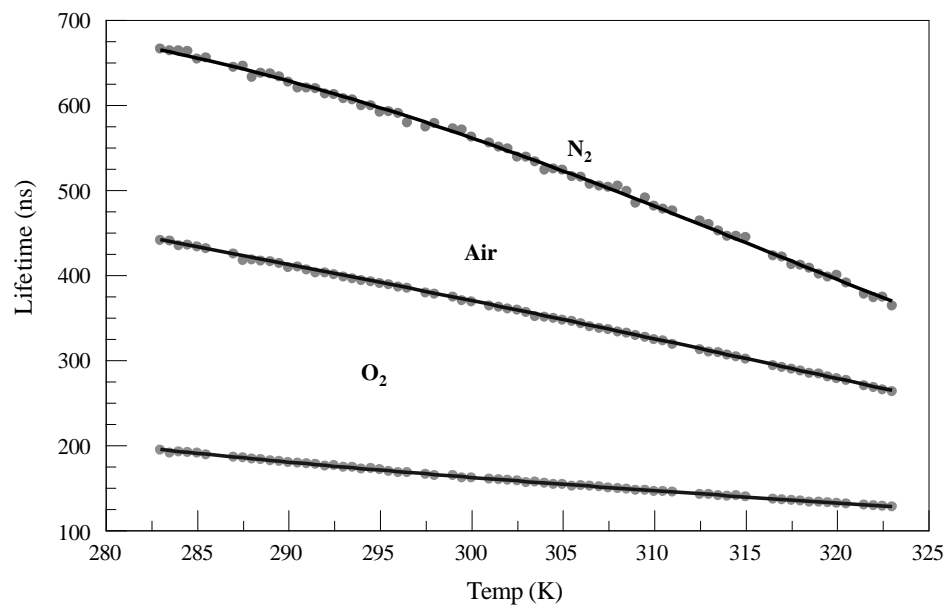


Figure 3: Lifetime temperature dependence of $\text{Ru}(\text{bpy})_3^{2+}$ in distilled water purged with N_2 , air, O_2 . The dots are data points, while the solid black lines represent the fit to the model.

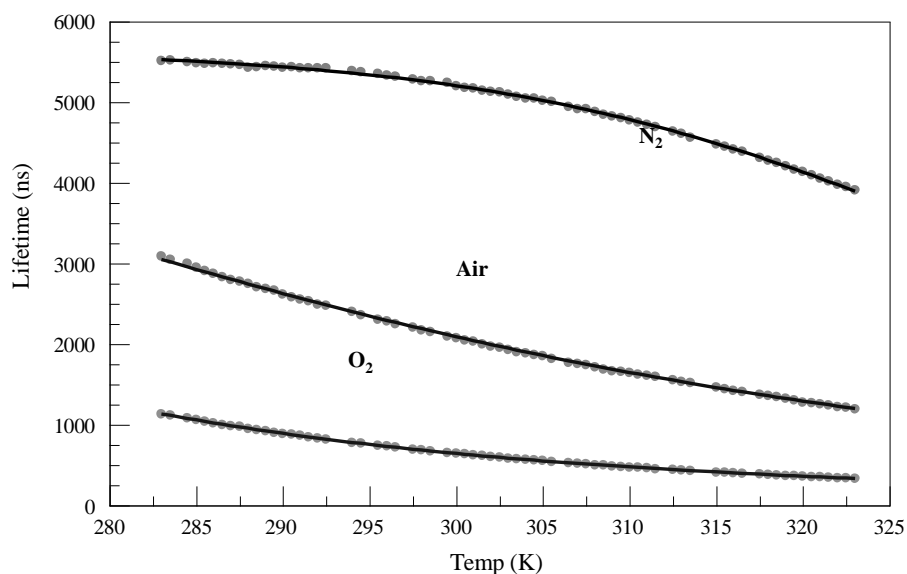


Figure 4: Lifetime temperature dependence of $Ru(dpp)_3^{2+}$ in ethylene glycol purged with N_2 , air, and O_2 . The dots are data points, while the solid black lines represent the fit to the model.

However, the different quantities in the equations are temperature dependent. k_2 will increase while τ_0 and K_h will decrease with increasing temperature. Therefore a complex temperature dependence for K_{svP} would not be surprising. Rewriting equation 9 including the temperature dependence we obtain

$$\tau(T) = 1/(k_0 + k_{dd}(T) + [K_{svP}(T)/\tau_0(T)] \cdot P_{\text{oxygen}}) \quad (10a)$$

$$\tau(T) = \tau_0(T)/(1 + K_{svP}(T) \cdot P_{\text{oxygen}}) \quad (10b)$$

Equation 10b allows the calculation of τ at any temperature and oxygen pressure if one knows $\tau_0(T)$ and $K_{svP}(T)$. Equation 1 provides a fundamental form for $\tau_0(T)$ and the oxygen free temperature data can provide the necessary parameters to reproduce $\tau_0(T)$. Figure 5 shows the $K_{svP}(T)$ vs. T for $\text{Ru}(\text{dpp})_3^{2+}$ in ethylene glycol.

There is no good fundamental expression for $K_{svP}(T)$, but for standards one only needs a fitting equation that accurately reproduces the data. We initially tried a second order polynomial fit of $K_{svP}(T)$ vs. T (Figure 5a), which works moderately well, but it has trouble fitting the low and high temperature limits. However, if we define k_2 in terms of pressure, k_{2P} , we have

$$k_{2P} = K_{svP}(T)/\tau_0(T) \quad (11)$$

which gives a much smoother curve that is essentially perfectly fit by a second order polynomial (Figure 5b). Using the three parameters for the fit to $\tau_0(T)$ and the three polynomial coefficients (B, C, and D), we can then generate $\tau(T)$ at all pressures and temperatures from

$$\tau(T) = \tau_0(T)/(1 + (k_{2P}(T) \tau_0(T) \cdot P_{\text{oxygen}})) \quad (12)$$

$$k_{2P}(T) = B + CT + DT^2 \quad (13)$$

$\tau_0(T)$ is given by the three-parameter equation 1.

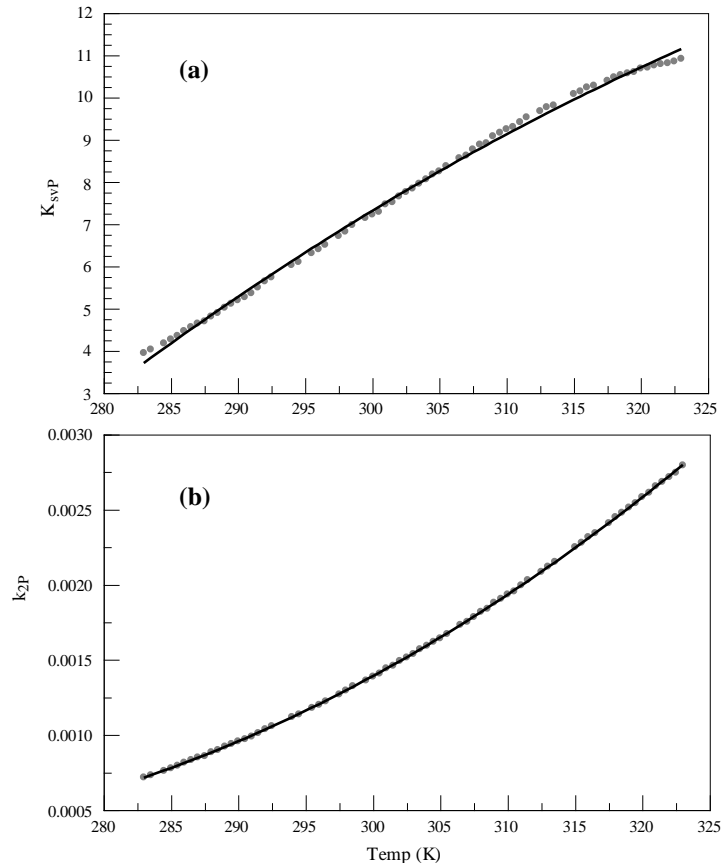


Figure 5: (a) Temperature dependence of K_{SVp} . The dots are calculated pressure based Stern-Volmer constant, K_{SVp} , for each temperature, while the solid black line represents a second order polynomial fit of K_{SVp} . (b) Temperature dependence of k_{2P} . The dots are the defined k_{2P} calculated using the temperature dependent pressure based Stern-Volmer constant divided by the unquenched temperature dependent luminescent lifetime, while the solid black line is the second order polynomial fit of $k_{2P}(T)$.

The fits in Figures 3 and 4 are derived from the 6 parameters needed in equations 1, 2, 3 and 13. The fits are essentially perfect. The standard deviations for all three pressures and all temperatures are 10.5 ns for the $\text{Ru}(\text{dpp})_3^{2+}$ in glycol and 2.1 ns for $\text{Ru}(\text{bpy})_3^{2+}$ in water. Comparable fits are obtained for the remaining systems. Table 1 shows the parameters for the best fits for the different systems along with standard deviations for each data set. One should put no fundamental significance on the constants B, C, and D. They are merely fitting parameters that accurately describe the data. Table 2 summarizes the operational range for each system.

Table 1: Fitting parameters ^a								
Complex	Solvent	$\underline{k}_0 \cdot 10^{-5}$ (s ⁻¹)	$\underline{k}_{dd} \cdot 10^{-12}$ (s ⁻¹)	\underline{E} (cm ⁻¹)	$\underline{B} \cdot 10^{-6}$ (s·atm) ⁻¹	$\underline{C} \cdot 10^{-4}$ (s·atm·K) ⁻¹	$\underline{D} \cdot 10^{-1}$ (s·atm) ⁻¹ (K) ⁻²	Std Dev (ns)
Ru(bpy) ₃	Ethylene Glycol	7.609	55.18	3834	30.66	-24.6	49.61	4.6
	Distilled Water	13.26	2.657	3238	-37.21	23.78	-32.95	2.1
	Glycerol	7.693	169.7	4115	5.572	-3.935	6.95	4.4
Ru(dpp) ₃	Ethylene Glycol	1.774	249.6	4894	33.97	-26.52	52.17	10.5

a) The number of significant figures on the fitting parameters is provided only to give reliably computed lifetimes and no physical significance should be attributed to their number or certainty.

Table 2: Optimal lifetime ranges of Ru(bpy) ₃ ²⁺ and Ru(dpp) ₃ ²⁺ in glycol, water, and glycerol			
<u>Complex</u>	<u>Solvent</u>	<u>Lifetime – low end</u> (O ₂ high temperature)	<u>Lifetime – high end</u> (N ₂ high temperature)
Ru(bpy) ₃	Ethylene Glycol	~ 200 ns	~1100 ns
	Distilled Water	~ 125 ns	~ 675 ns
	Glycerol	~ 350 ns	~ 1100 ns
Ru(dpp) ₃	Ethylene Glycol	~ 300 ns	~ 5500 ns

If a setup such as the one described in our experiments is to be used in real world applications, then the system responses must be reproducible as well as not easily influenced by slight variations in sample preparation or measurements. Figure 6 shows the lifetime temperature dependence of a Ru(dpp)₃²⁺ in ethylene glycol. The two sets of data correspond to experiments performed on the same sample more than a week apart. As you can see from Figure 6, the two separate experiments agree well. Figure 7 shows the effect of concentration variations for Ru(dpp)₃²⁺ in O₂ purged ethylene glycol samples (3:M, 10:M, and 24 :M). The differences in the lifetimes of the three samples over the temperature range of 283K to 323K are negligible. This is not surprising as we would not expect appreciable self-quenching in these systems, especially at such low concentrations.

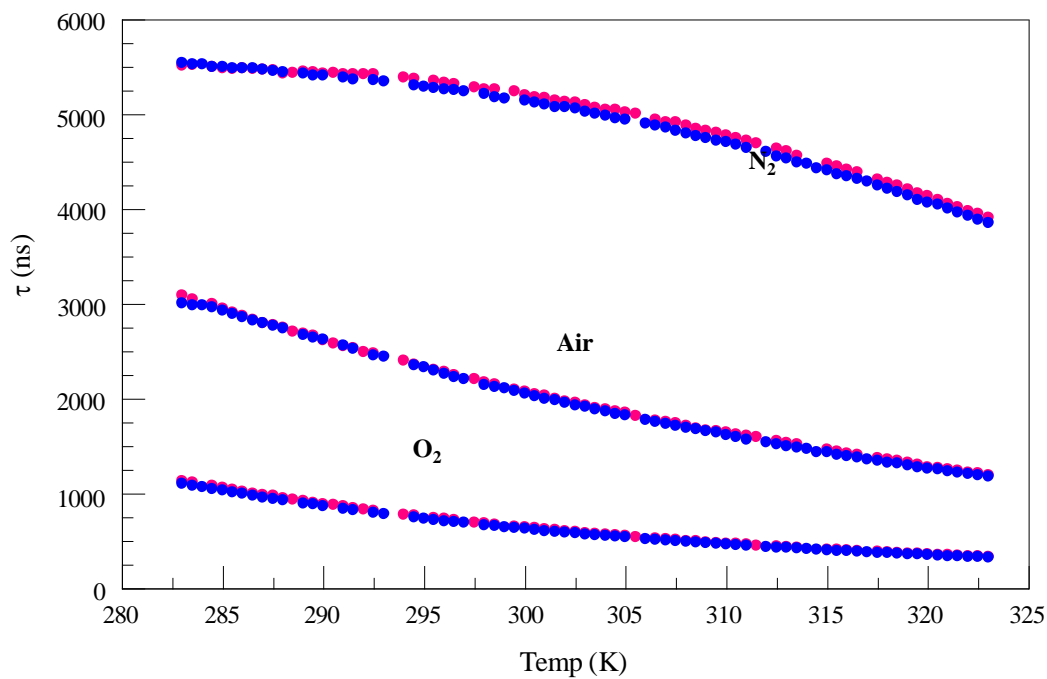


Figure 6: $Ru(dpp)_3^{2+}$ in ethylene glycol purged with N_2 , air, and O_2 . The red and blue dots are data collected more than a week apart.

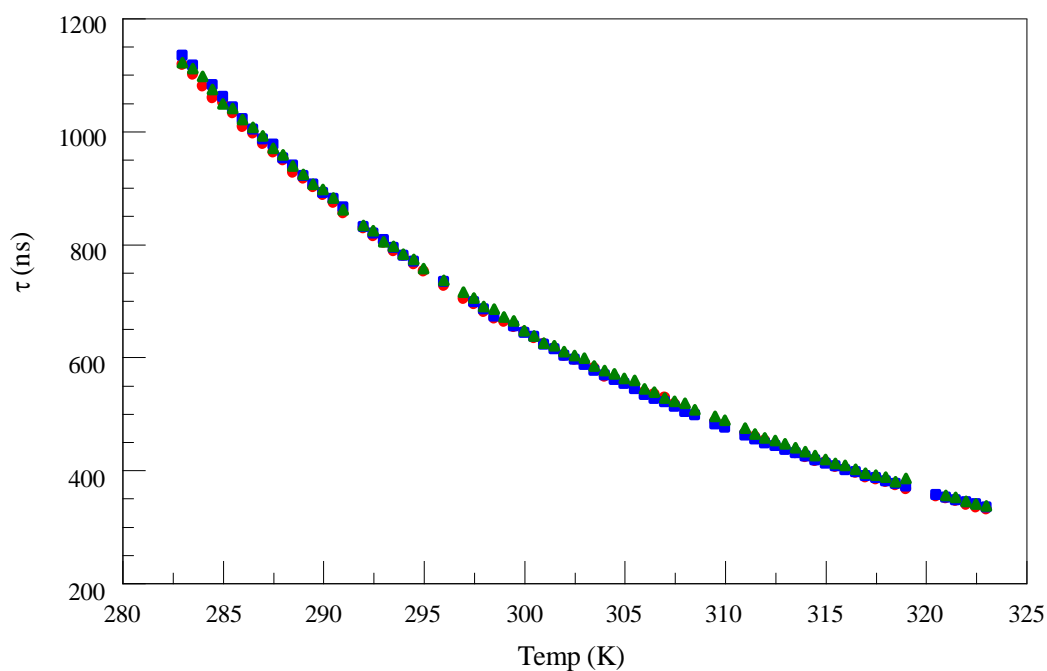


Figure 7: O_2 purged, $Ru(dpp)_3^{2+}$ in ethylene glycol samples of varying concentrations (3:M –green triangles, 10:M -blue squares, 24:M –red circles).

Conclusions

A method was developed that allowed the rapid and efficient determination of the temperature and oxygen dependence of excited state lifetimes in a variety of systems. It was used to characterize two Ru(II)

complexes in a several solvents. These systems are useful as lifetime standards. Each system can be fit with high precision over the range 10-50° C and 0 to one atmosphere of oxygen with a simple, six parameter equation. The applied model fits extremely well for all systems and almost perfectly for some. The systems covered a wide range of lifetimes from a little more than one hundred nanoseconds to approximately five and a half microseconds. This allows potential users the flexibility of being able to choose the appropriate system for checking system calibration either in the laboratory or in the field. Because the decays are essential pure exponentials, the standards are suitable for both pulsed and phase shift instruments.

References – Chapter 4

1. Coyle, L. M.; Gouterman, M. *Sens. Actuators, B* 1999, *61*, 92-99.
2. Zelelow, B.; Khalil, G.; Phelan, G.; Carlson, B.; Gouterman, M.; Callis, J. B.; Dalton, L. R. *Sens. Actuators, B* 2003, *96*, 304-314.
3. Hradil, J.; Davis, C.; Mongey, K.; McDonagh, C.; MacCraith, B. D. *Meas. Sci. Technol.* 2002, *13*, 1552-1557.
4. Koese, M. E.; Carrol, B. F.; Schanze, K. S. *Langmuir* 2005, *21*, 9121-9129.
5. Gouterman, M.; Callis, J.; Dalton, L.; Khalil, G.; Mébarki, Y.; Cooper, K. R.; Grenier, M. *Meas. Sci. Technol.* 2004, *15*, 1986-1994.
6. Lo, K.; Hui, W.; Ng, D.; Cheung, K.; *Inorg. Chem.* **41** (2002), p. 40.
7. Lo, K.; Chan, J.; Chung, C.; *Inorg. Chim. Acta* **357** (2004), p. 3109.
8. Amao, Y. *Microchim. Acta* 2003, *143*, 1-12.
9. DiMarco, G.; Lanza, M. *Sens. Actuators B* 2000, *63*, 42-48.
10. Yeh, T.; Chu, C.; Lo, Y. *Sens. Actuators B* 2006, *119*, 701-707.

11. Bell, J.; Schairer, E.; Hand, L.; Mehta, R. *Annu. Rev. Fluid Mech.* 2001, 33, 155–206.
12. de Silva, A. P.; Gunaratne, H. Q. N.; Gunnlaugsson, T.; Huxley, A. J. M.; McCoy, C. P.; Rademacher, J. T.; Rice, T. E. *Chem. Rev.* 1997, 97, 1515-1566.
13. Demas, J. N.; DeGraff, B. A. *Coord. Chem. Rev.* 2001, 211, 317-351.
14. Demas, J. N.; DeGraff, B. A.; Coleman, P. B. *Anal. Chem.* 1999, 71, 793A-800A.
15. Malins, C.; Glever, H. G.; Keyes, T. E.; Vos, J. G.; Dressick, W. J.; MacCraith, B. D. *Sens. Actuators, B* 2000, 67, 89-95.
16. Huber, C.; Klimant, I.; Krause, C.; Wolfbeis, O. S. *Anal. Chem.* 2001, 73 (9), 2097-2103.
17. Mills, A.; Eaton, K. *Quim. Anal.* 2000, 19, 75-87.
18. Demas, J. N.; DeGraff, B. A. *Proc. SPIE-Int. Soc. Opt. Eng.* 1992, 1796, 71-75.
19. Lippitsch, M. E.; Draxler, S. *Sens. Actuators, B* 1993, 11, 97-101.

20. Boens, N.; Pouget, J.; Gratton, E.; Enggelborghs, Y.; Rumbles, G.; Visser, A.; Lakowicz, J.; Szabo, A.; Tamai, N. *Anal. Chem.* 2007, 79, 2137-2149.
21. Lakowicz, J. R. *Principles of Fluorescence Spectroscopy*, 2nd ed.; KluwerAcademic/Plenum Publishers: New York, 1999.
22. Lin, C. T.; Boettcher.; Chou, M.; Creutz, C.; Sutin, N. *J. Am. Soc.* **1976**, 98, 6536-44.

Chapter 5: Room Temperature Ionic Liquids

General Background

The sensor support is a critical element in the design, application, and operation of any luminescent probe. As with any luminescence sensor support, the characteristics of the support affect the sensing properties of the probe. In efforts to create better luminescent sensors, it is imperative that new sensor supports consistently be investigated.

Room temperature ionic liquids are a unique and interesting class of material that has recently shown a remarkable growth in usage in many areas of chemistry and engineering.¹⁻⁵ Room temperature ionic liquids are currently being used in synthesis, as catalyst, in batteries, and in fuel cells. RTILs are non-volatile and have little to no vapor pressure, as a result, they have become an extremely attractive alternative as solvents in “green chemistry”.¹⁻⁴ Furthermore, RTILs are inexpensive to manufacture, have high thermal stability, and are non-flammable.

While research and applications involving RTILs is extensive and steadily growing, there has been limited amount of research investigating their use as supports for luminescence based sensors. RTILs have many attractive properties that make them ideal candidates for such applications.

In this work, several RTILs are used as supports for two Ru(II) luminescent oxygen probes. The oxygen sensing and photophysical properties of the luminescence based sensors are examined. The remarkable behavior of the various luminescence based oxygen sensors is attributed to the unique properties of the RTILs.

RTILs simply put are molten salts. Conventionally to be considered a RTIL, the melting point of the salt must be below 100 °C.² RTILs consist of large bulky asymmetric cations (typically organic) and anions. The large asymmetric cations are the main cause for the low melting temperature of the ionic salts. The bulky cations reduce the lattice energy and thus lower the melting point of the salt.

The compositional difference between the most well-known salt sodium chloride, NaCl, and that of the RTIL 1-propyl-3-methylimidazolium chloride is the bulky 1-propyl-3-methylimidazolium cation. The presence of the bulky cation in the latter creates marked differences in the physical properties of the two salts. For example, sodium chloride has a melting point of 801 °C while the large asymmetric cation of the 1-propyl-3-methylimidazolium chloride results in a melting point of 60 °C for the RTIL.^{2,6}

Not only do RTILs have low melting points, but they also remain liquid over a range of more than 400 K. This is one of the many interesting properties of RTILs that make them very attractive as solvents for synthesis and extraction.¹⁻⁴ Other such properties of RTILs include their ability to simultaneously dissolve both organic and inorganic materials at the same time. Also, RTILs are miscible with substances having a wide range of polarities. Further, the ionic charges inside the RTILs can be used to influence synthesis.^{1,3}

The abundance of ionic charge carriers inside RTILs also make RTILs ideal supporting electrolytes for electrochemical reactions. The oxidation and/or reduction of the supporting electrolyte is always a concern in electrochemical reactions; however, RTILs are known to have potential windows as large as 6 V, making them extremely electrochemically stable.⁷⁻⁸

In electrochemical measurements the reduction and/or oxidation of the ions in RTILs are typically not a concern, however impurities in RTILs are known to narrow the potential window of RTILs.⁷ Impurities can also greatly affect the density, viscosity, and thermal stability of RTILs.^{1,9} As a result, impurities are of great concern when evaluating the physical and chemical properties of RTILs. The major impurities found in RTILs are water and halides.^{1,9}

Although impurities affect the physical and chemical properties of RTILs, the base cations and anions provide the major properties associated with RTILs.¹ Physical properties of RTILs can be altered by varying the cations and anions of the liquid salt. Further, RTIL properties can be fine-tuned by varying the length and branching of functional groups associated with the cation.

The ability to adjust physical and chemical properties of RTILs such as viscosity, index of refraction, density, melting point, potential window, conductivity, hydrophobicity, and miscibility by varying the choice and structure of its ions is why RTILs have been termed “designer solvents”.¹⁻³ Because of this unique characteristic of RTILs it is possible to tailor RTILs for specific applications.

Many different RTILs with varying properties have been designed and utilized in various applications. There are currently hundreds of known RTILs.¹ The possible number of cation/anion pairings possible to create RTILs is almost limitless. Earle and Seddon predict that the number of possible RTILs exceeds one billion.²

Structure of RTILs

The unique properties of RTILs are attributed to their structure. To better understand the nature of this interesting class of material, techniques such as x-ray diffraction (XRD), small angle x-ray diffraction (SAXRD), Raman spectroscopy, and computer simulations have been implemented to investigate the structure of RTILs.¹⁰⁻¹⁴

Several studies examining the structure of RTILs have shown that RTILs exhibit considerable short range order. For example, in a study by Katayanagi, it was concluded that RTILs can exist as weakly aligned patches of crystal-like structures.¹³ It was reported that the crystal-like patches were the result of the short range ordering of the aligned chloride and bromide ions in the RTILs.

Another study suggested that the bulky cations in the RTILs investigated formed aggregates surrounded by free anions.¹⁴ The study reported that the long alkyl tails on the cations clustered together. The description is similar to that of micelles with the exception being that the aggregation is the result of the hydrophobic alkyl tails not the hydrophilic head group. It was shown that the alkyl chain length determined the ordering of the system. The shorter the alkyl chain, the higher the ordering;

as result, the higher the melting temperature. The RTILs with intermediate alkyl chain lengths that were studied were shown to have nanometer range ordering.

Understanding the nature of the structure of RTILs is critical in understanding the photophysical and oxygen sensing properties of our luminescence based oxygen probes if such materials are to be utilized as sensor supports. The RTILs that were used as sensor supports in this study are: 1-butyl-1-methylpyrrolidinium bis(trifluoromethanesulfonyl) imide ([C4mpy][Tf₂N]), 1-butyl-1-methylpyrrolidinium bis(pentafluoroethylsulfonyl) imide ([C4mpy][beti]), 1-hexyl-1-methylpyrrolidinium bis(trifluoromethanesulfonyl) imide ([C6mpy][Tf₂N]), 1-decyl-1-methylpyrrolidinium bis(trifluoromethanesulfonyl) imide ([C10mpy][Tf₂N]), 1-propyl-3-methylimidazolium bis(pentafluoroethylsulfonyl) imide ([C3mimm][beti]), 1-ethyl-3-methylimidazolium bis(trifluoromethanesulfonyl) imide ([Emim][Tf₂N]), methyl-tributylammonium bis(pentafluoroethylsulfonyl) imide ([N4,4,4,1][beti]), and trihexyl-(tetradecyl)phosponium bis(trifluoromethanesulfonyl) imide ([P14,6,6,6][Tf₂N]). Their structures are shown in Figure 1. In this work the RTILs used consisted of two anions, [beti] and [Tf₂N], with various cations of differing sizes and shapes.

Based on the studies of the structure of RTILs, it is reasonable to suggest that some form of aggregation or short range order exists inside RTILs. Such short range ordering in RTILs will be used to help explain the anomalously high oxygen quenching exhibited by several Ru(II)/RTIL luminescence based oxygen sensors in this work.

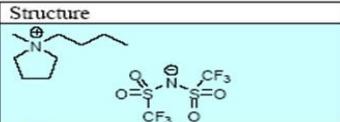
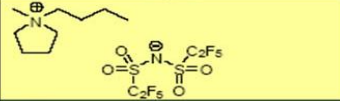
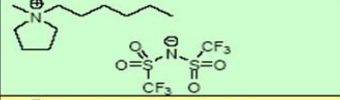
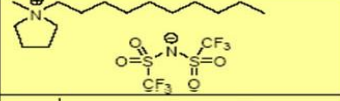
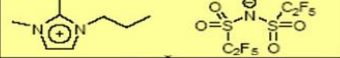
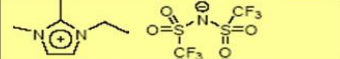
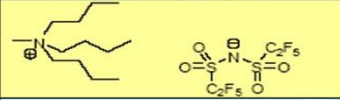
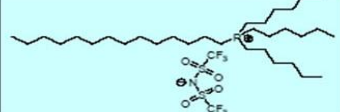
RTIL Label	Structure
[C ₄ mpy][Tf ₂ N]	
[C ₄ mpy][beti]	
[C ₆ mpy][Tf ₂ N]	
[C ₁₀ mpy][Tf ₂ N]	
[C ₃ mim][beti]	
[Emim][Tf N]	
[N ₄₄₄₁][beti]	
[P _{6,6,6,14}][Tf ₂ N]	

Figure 1. Abbreviations and structures for the room temperature ionic liquids (RTILs) used in this study. RTILs are composed of cations and anions. The cations structures and abbreviations are to the left and the anions are to the right.

References – Chapter 5

1. K. Marsh; J. Boxall; R. Lichtenthaler. “Room temperature ionic liquids and their mixtures – a review.” *Fluid Phase Equilibria*. 219, **2004**, 93-98
2. M. Earle; K. Seddon. *Pure Appl. Chem.* 72, **2000**, 1391-1398
3. S. Pandey. “Analytical applications of room-temperature ionic liquids: A review of recent efforts.” *Analytica Chimica Acta*. 556, **2006**, 38-45
4. J. Huddleston; A. Visser; M. Reichert; H. Willauer; G. Broker; R. Rogers. “Characterization and comparison of hydrophilic and hydrophobic room temperature ionic liquids incorporating the imidazolium cation.” *Green Chemistry*. 3, 2001, 156-164
5. H. Matsumoto; H. Sakaebe; K. Tatsumi. “Preparation of room temperature ionic liquids base on aliphatic onium cations and asymmetric amide anions and their electrochemical properties as a lithium battery electrolyte.” *Journal of Power Sources*. 146, **2005**, 45-50
6. B. Dinker; L. Sirdeshmukh; K. Subhadra. *Alkali halides: a handbook of physical properties*. Springer. **2001**, 65, 68
7. E. Rogers; B. Sljucic; C. Hardacre; R. Compton. “Electrochemistry in Room-Temperature Ionic Liquids: Potential Windows at Mercury Electrodes.” *J. Chem. Eng. Data*. 54, **2009**, 2049-2053

8. D. Silvester; R. Compton. "Electrochemistry in Room Temperature Ionic Liquids: A Review and Some Possible Applications." *Z. Phys. Chem.* **220**, **2006**, 1247-1274
9. K. Seddon; A. Stark; M. Torres. "Influence of chloride, water, and organic solvents on the physical properties of ionic liquids." *Pure Appl. Chem.* Vol. **72**, **2000**, 2275-2287
10. Gomes, M. F.; Lopes, J. N.; and Padua, A. "Thermodynamics and Micro Heterogeneity of Ionic Liquids." *Top Curr Chem.* **2009**
11. Liu, Y.; Li, J.; Wang, M.; Li, Z.; Liu, H.; He, P.; Yang, X.; Li, J. "Preparation and Properties of Nanostructure Anatase TiO₂ Monoliths Using 1-Butyl-3-methylimidazolium Tetrafluoroborate Room-Temperature Ionic Liquids as Template Solvents." *Crystal Growth & Design*, **2005**, *5* (4), pp 1643–1649
12. Triolo, A.; Russina, O.; Fazio, B.; Triolo, R.; Di Cola, E. "Morphology of 1-alkyl-3-methylimidazolium hexafluorophosphate room temperature ionic liquids." *Chemical Physics Letters* **457**, **2008**, 362–365
13. Katayanagi, H.; Hayashi, S.; Hamaguchi, H.; Nishikawa, K. "Structure of an ionic liquid, 1-n-butyl-3-methylimidazolium iodide, studied by wide-angle X-ray scattering and Raman spectroscopy." *Chem. Phys Let.* **392**, **2004**, 460–464.

14. Triolo, A.; Russina, O.; Bleif, H.; and Di Cola, E. "Nanoscale Segregation in Room Temperature Ionic Liquids." *J. Phys. Chem. B.* 111, **2007**, 4641-4644
15. D. Rooney; J. Jacquemin; R. Gardas. "Thermophysical Properties of Ionic Liquids." *Top Curr Chem.* 290, **2009**, 185-212

Chapter 6: Ru(II) Complexes in Room Temperature Ionic Liquids (RTILs): Oxygen Sensing Properties

Introduction

The unique and interesting properties of RTILs that make them attractive solvents for many applications were discussed extensively in Chapter 5.¹⁻⁸ However, since little research has been done investigating their use in luminescence applications little is known of the effectiveness of their use as supports for luminescence based sensors.

The local environment of the luminophore plays a critical role in determining the properties of any luminescence based sensor. Thus, understanding the interaction between the luminophore and support is essential to the understanding of the photo-physics involved in the operation of any luminescence based sensor. Further, insight to the nature of the luminophore-support interaction will be necessary to the practical design and application of such sensors.

To investigate the applicability of RTILs as supports for luminescence based oxygen sensors, the quenching properties of our two Ru(II) complexes in the several RTILs listed in Chapter 5 were examined. The luminescence lifetime at three separate oxygen partial pressures were measured for each sample using a simple homemade lifetime instrument. The instrument was

similar in design to the one used for the lifetime standards measurements discussed in Chapter 4 but with a few modifications.

During the course of the investigation, the RTILs studied were found to be intensely fluorescent. The fluorescence from certain RTILs was vivid enough to be visible with the naked eye. The high energy RTIL fluorescence was greatly minimized by use of a 405 nm diode laser instead of the 337 nm N₂ laser used during the lifetime standards experiment. Use of the new excitation source required a slightly more complicated data collection and analysis procedure.

Materials: Each sample consisted of one of the two Ru(II) metal complexes dissolved in one of the several RTILs. The ruthenium complex tris-(4,7-diphenyl-1,10-phenanthroline)ruthenium(II) dichloride, [Ru(dpp)₃]Cl₂, was from GFS Chemicals Inc. while tris-(2,2'-bipyridine)ruthenium(II) dichloride, [Ru(bpy)₃]Cl₂, complex was synthesized by standard method as referenced in Chapter 4,⁹ but it is also available from GFS Chemicals and others. The RTILs: 1-butyl-1-methylpyrrolidinium bis(trifluoromethanesulfonyl) imide ([C4mpy][Tf₂N]), 1-butyl-1-methylpyrrolidinium bis(pentafluoroethylsulfonyl) imide ([C4mpy][beti]), 1-hexyl-1-methylpyrrolidinium bis(trifluoromethanesulfonyl) imide ([C6mpy][Tf₂N]), 1-decyl-1-

methylpyrrolidinium bis(trifluoromethanesulfonyl) imide ([C10mpy][Tf₂N]), 1-propyl-3-methylimidazolium bis(pentafluoroethylsulfonyl) imide ([C3mimm][beti]), 1-ethyl-3-methylimidazolium bis(trifluoromethanesulfonyl) imide ([Emim][Tf₂N]), methyl-tributylammonium bis(pentafluoroethylsulfonyl) imide ([N4,4,4,1][beti]), and trihexyl-(tetradecyl)phosponium bis(trifluoromethanesulfonyl) imide ([P14,6,6,6][Tf₂N]) were all obtained courtesy of Dr. Gary Baker, Oak Ridge National Laboratory.

Typically, less than 0.2 mL of sample was used for each measurement. Due to the extremely small sample size, the Ru(II) concentrations for these experiments were not measured. However, samples were made optically dilute while ensuring that the Ru(II) concentrations were still high enough to produce a sufficient signal to noise ratio.

Experimental Setup: The experimental setup used is shown in Figure 1. Ru(II)/RTIL samples were placed in a test tube. A continuous, 5 mW, 405 nm diode laser (Power Technology Inc.) connected to a pulse generator (Stanford Research Systems, DG535) was used to create a short, 200 ns square wave excitation pulse. To control the magnitude of the excitation light hitting the sample and thus the resulting luminescence signal, an aperture was placed between the laser and the sample. A fiber optic was

used to transmit the luminescence from the sample to the front face of a Hamamatsu R928 photomultiplier tube. A complementary red pass filter and a sodium nitrite solution were placed in front of the PMT to eliminate any RTIL fluorescence and scattered excitation light. The photomultiplier output was recorded on a digital oscilloscope (Tektronix TDS 2022 Two Channel Storage Oscilloscope, 200 MHz, 2GS/sec) interfaced to a desktop PC through an IEEE 488 interface. A 50Σ load resistor was used.

During data collection, compressed N_2 , air, or O_2 gas bubbled directly into the sample. A micro stir bar placed in the bottom the sample test tube provided continuous stirring of the sample to ensure gas equilibrium within the sample.

Experimental Procedure: All measurements were performed at room temperature, 25 °C. Samples were purged with nitrogen, oxygen, and air, respectively, for approximately twenty minutes to allow the systems to equilibrate. The pulse generator produced a 200 ns duration square-wave pulse which was applied to the 405 nm continuous diode laser. This created a 200 ns rectangular-wave that was used to pump the samples. Intensity versus time profiles were measured for the respective gases.

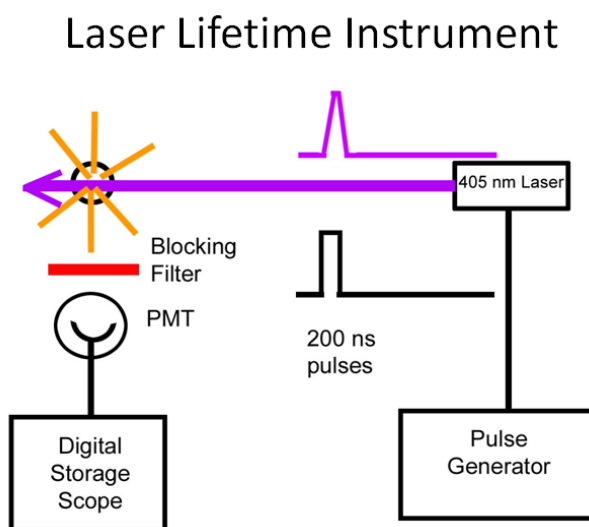


Figure 1. Schematic diagram of Ru(II)/RTIL luminescence quenching experimental setup.

During data collection two thousand decay profiles were collected and averaged using Labview software to produce one decay curve per measurement. Background measurements were made for all samples by recording intensity versus time profiles under the same settings as the gas purged data sets but with the aperture closed. The background profiles were later subtracted from the sample decay curves.

Because the considerably short lifetimes of the $\text{Ru}(\text{bpy})_3^{2+}$ systems, and the oxygen and air purged $\text{Ru}(\text{dpp})_3^{2+}$ samples were comparable to the duration of the excitation pulse, deconvolution of the luminescence decay had to be performed during data analysis. This data analysis technique

required an additional decay profile known as the instrument response function (IRF) to be recorded during the data collection. To obtain the IRF, the decay profile of subnanosecond rose bengal sample (solvent) was measured under the same settings as each of the $\text{Ru}(\text{bpy})_3^{2+}$ systems, as well as the oxygen and air purged $\text{Ru}(\text{dpp})_3^{2+}$ samples.

All pulses generated from real photoluminescence excitation sources have finite pulse widths, shapes, and characteristics determined by the instrumentation; it is impossible to create a true delta function pulse. The non-ideal shape of physical excitation light sources causes measured luminescence decays to deviate from a pure theoretical exponential decay. The measured decay is the result of the convolution of the pure exponential decay and the instrument response function and is given by

$$I(t) = \int_0^t D(\tau)IRF(t - \tau)d\tau \quad (1)$$

Where $I(t)$ is the measured luminescence intensity profile and $D(\tau)$ is the free exponential decay of the luminophore.

Even though all physical excitation sources are non-ideal if the excitation pulse is temporally narrow compared to the time scale of the luminescence decay, the measured luminescence decay will not be significantly distorted by the finite width of the excitation pulse. The

lifetime would then typically be calculated by a nonlinear least squares fitting of the recorded decay curve to a predicted exponential model. If on the other hand the excitation source is wide when compared to the luminescence decay of the luminophore, large deviations will exist between the measured decay and the free decay. To determine lifetimes under these circumstances a deconvolution of the signal must be made.

Iterative reconvolution is a pseudo deconvolution technique in which the IRF is convoluted with test luminescence decays of an assumed model until the best fit to the measured decay curve is obtained.¹¹ The parameters of the model are iteratively varied and a least squares method is used to determine the best fit to the measured decay profile. In order to perform an iterative reconvolution, the IRF must be first determined. The IRF is obtained by recording the intensity profile of a scattering sample or, in our case, a very short-lived fluorescent dye under the same conditions as the measured decay profile. The decay profile of rose bengal was used in our measurements as the IRF. Rose bengal has a lifetime of at 25 °C is 0.519 ns.¹¹

The luminescence decay of N₂ purged Ru(dpp)₃²⁺ samples are long-lived. Therefore it was not necessary to deconvolute the decay curves. All

N_2 purged $\text{Ru}(\text{dpp})_3^{2+}$ samples were fit well to a single exponential decay using a built in fitting routine in the PTI software.

Lifetimes for each sample were determined using the appropriate built in fitting function in the Photon Technology International (PTI) Felix 32 (NJ) software. All decays were single exponential.

After the lifetimes of the Ru(II) complexes in each of the RTILs were measured under nitrogen, oxygen, and air, a three-point Stern-Volmer plot for each Ru(II)/RTIL was generated. The Stern-Volmer plots were constructed by plotting the corresponding lifetimes as a function of oxygen partial pressure.

Results and Discussion

Figure 2 shows the luminescence decay profile for N_2 purged $\text{Ru}(\text{dpp})_3^{2+}/[\text{N4441}][\text{beti}]$ sample with the calculated fit superimposed. The x's are data points, while the solid black lines represent the fit to the single exponential predicted decay model. The residuals to the fit are displayed in Figure 3.

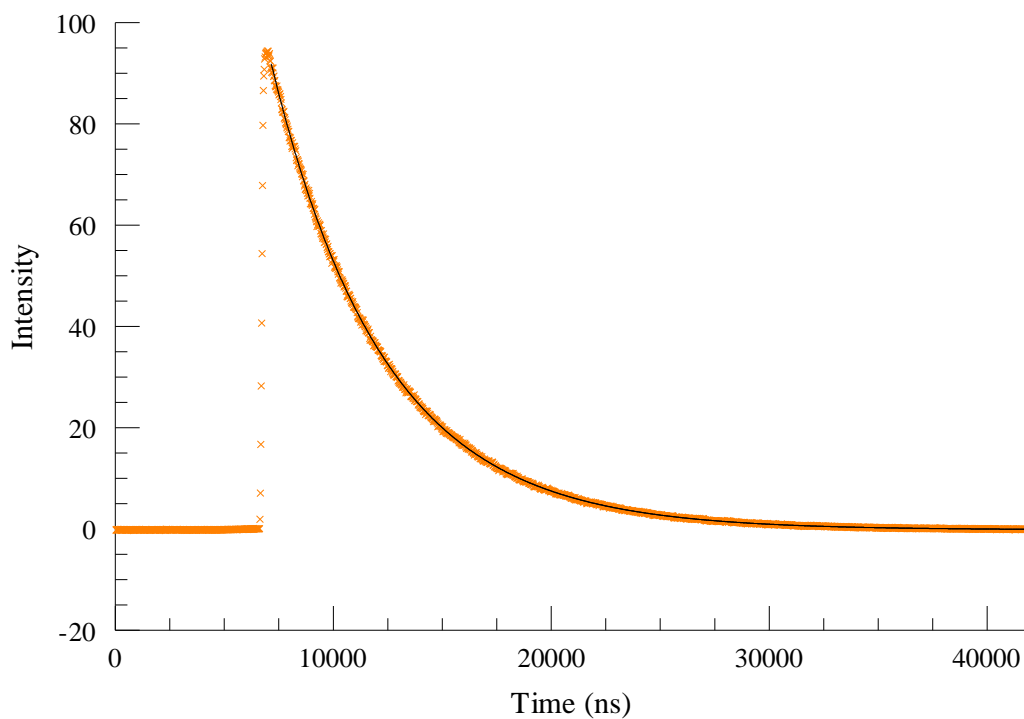


Figure 2: Luminescence decay and single exponential fit for N_2 purged $Ru(dpp)_3^{2+}/[N4441][beti]$. The x's are data points, while the solid black line represent the fit to the single exponential decay model.

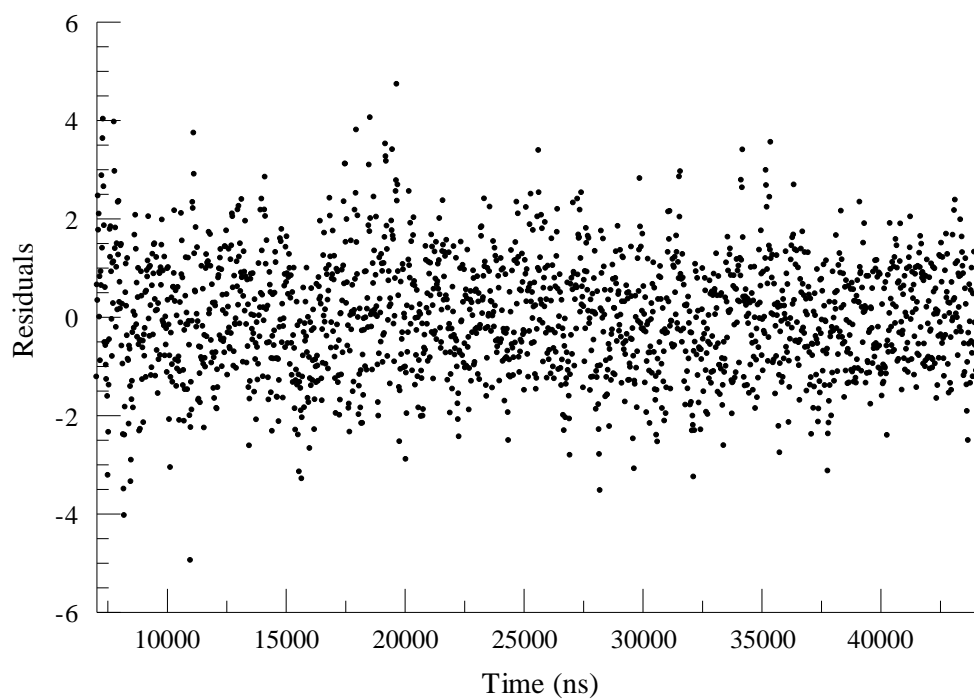


Figure 3: Residuals of single exponential fit to N_2 purged

$Ru(dpp)_3^{2+}/[N4441][beti]$ decay.

N_2 purged $Ru(dpp)_3^{2+}/[C6mpy][Tf_2N]$ are shown in Figure 4 and the corresponding residuals are shown in Figure 5.

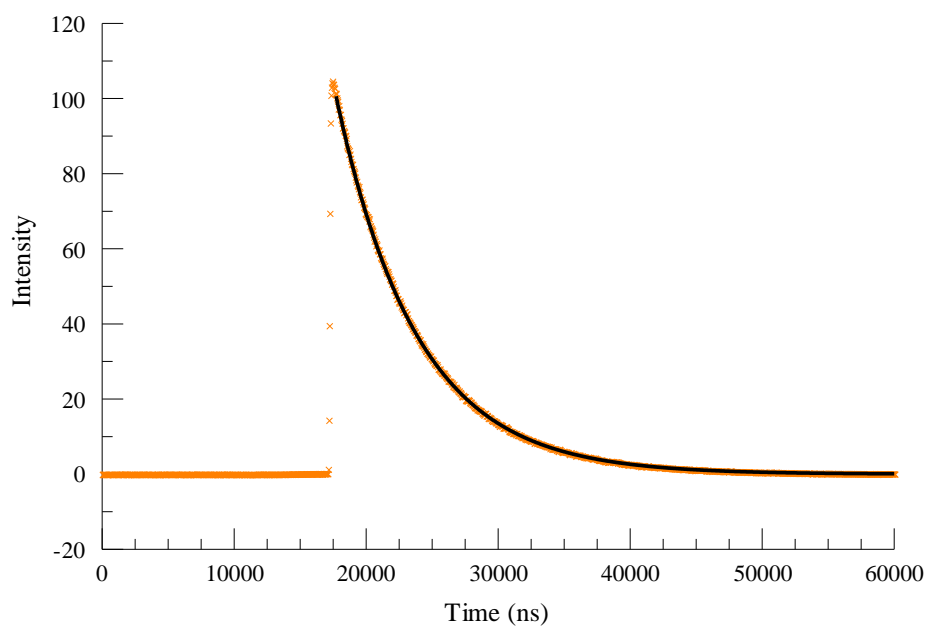


Figure 4: Luminescence decay and single exponential fit for N_2 purged $Ru(dpp)_3^{2+}/[C6mpy][Tf_2N]$. The x's are data points, while the solid black line represent the fit to the single exponential decay model.

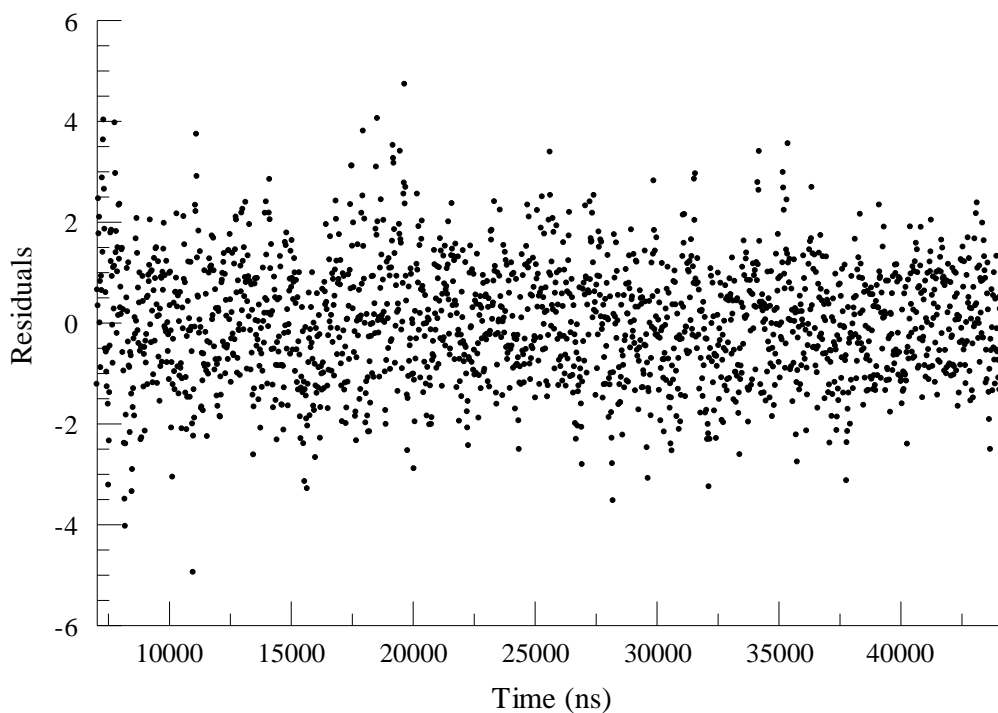


Figure 5: Residuals of single exponential fit to N₂ purged

Ru(dpp)₃²⁺/[C6mpy][Tf₂N] decay.

The N₂ purged Ru(dpp)₃²⁺/[N4441][beti] and Ru(dpp)₃²⁺/[C6mpy][Tf₂N] luminescence intensity profiles are described well by a single exponential decay with lifetimes of 5168 ± 1.6 ns and 6118 ± 2.6 ns respectively. Comparable fits using the same fitting procedure were obtained for all N₂ purged Ru(dpp)₃⁺²/RTIL systems.

The luminescence decay profile of air purged Ru(dpp)₃⁺²/[C6mpy][Tf₂N] and the fit using the iterative reconvolution

function of the PTI software is shown in Figure 6. The solid red line is the IRF, the circles are measured intensity data points, and the solid black lines represent the fit using the IRF and a single exponential decay model. The residuals to the fit are displayed in Figure 7. The iterative reconvolution of the rose bengal decay and the predicted single exponential decay model produced a lifetime of 1057 ± 0.09 ns. Clearly the residuals displayed in Figure 7 aren't as good as those for the N₂ purged samples but the single exponential model is still shown to describe the luminescence decay well.

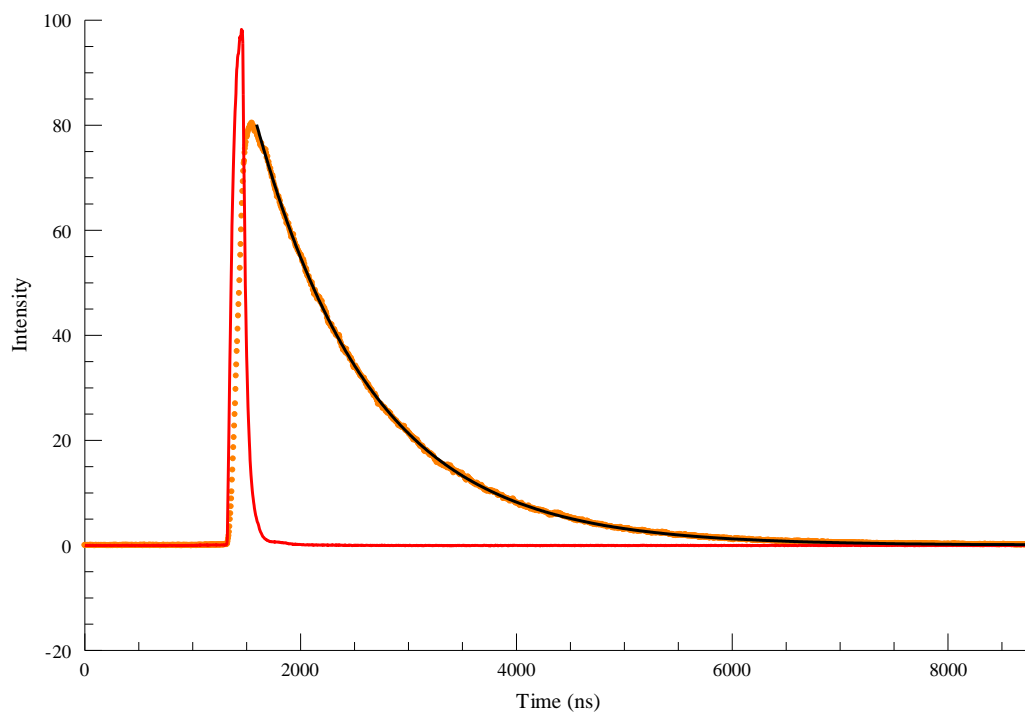


Figure 6: Rose bengal fluorescence, luminescence decay of air purged $Ru(dpp)_3^{2+}/[C6mpy][Tf_2N]$ sample, and single exponential fit using iterative reconvolution. The solid circles are the $Ru(dpp)_3^{2+}$ luminescence data points, the solid red line is the rose bengal data, and the solid black line is the fit.

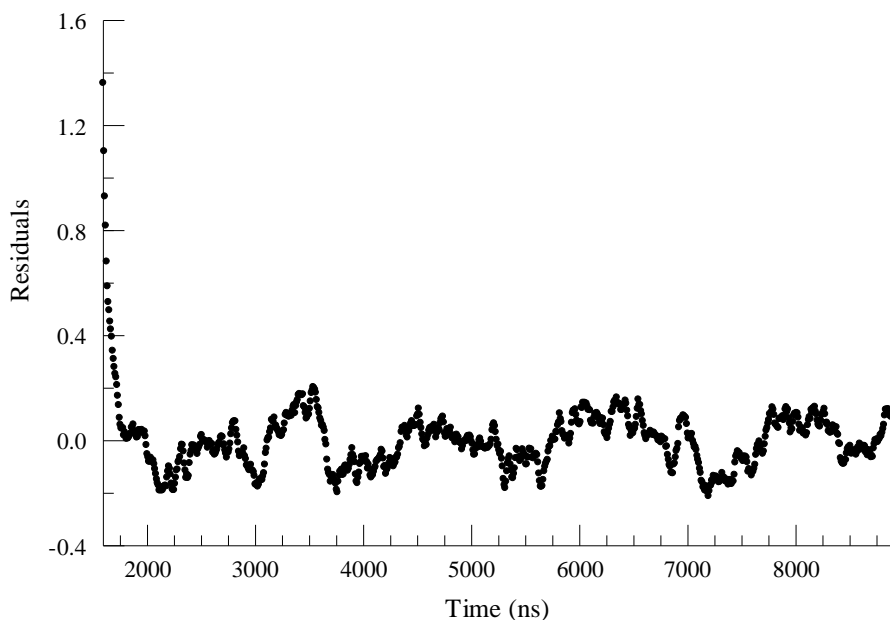


Figure 7: Residuals of single exponential fit to air purged

$Ru(dpp)_3^{2+}/[C6mpy][Tf_2N]$ luminescence decay using iterative reconvolution.

The emission decay profile of oxygen purged

$Ru(dpp)_3^{2+}/[C6mpy][Tf_2N]$ and the fit using the iterative reconvolution

function of the PTI software is shown in Figure 8. The solid red line is the

IRF, the open circles are measured intensity data points, and the solid black

lines represent the fit using the IRF and a single exponential decay model.

The residuals to the fit are displayed in Figure 9. The large amount of

quenching in the oxygen purged sample greatly decreases the luminescence

lifetime of the sample. As the lifetime decreases, the width of the excitation

pulse becomes more significant relative to the luminescence decay profile.

The notable width of the excitation pulse, as characterized by the fast decay of the rose bengal fluorescence, relative to that of the quenched $\text{Ru}(\text{dpp})_3^{+2}$ emission decay is clearly evident in Figure 8.

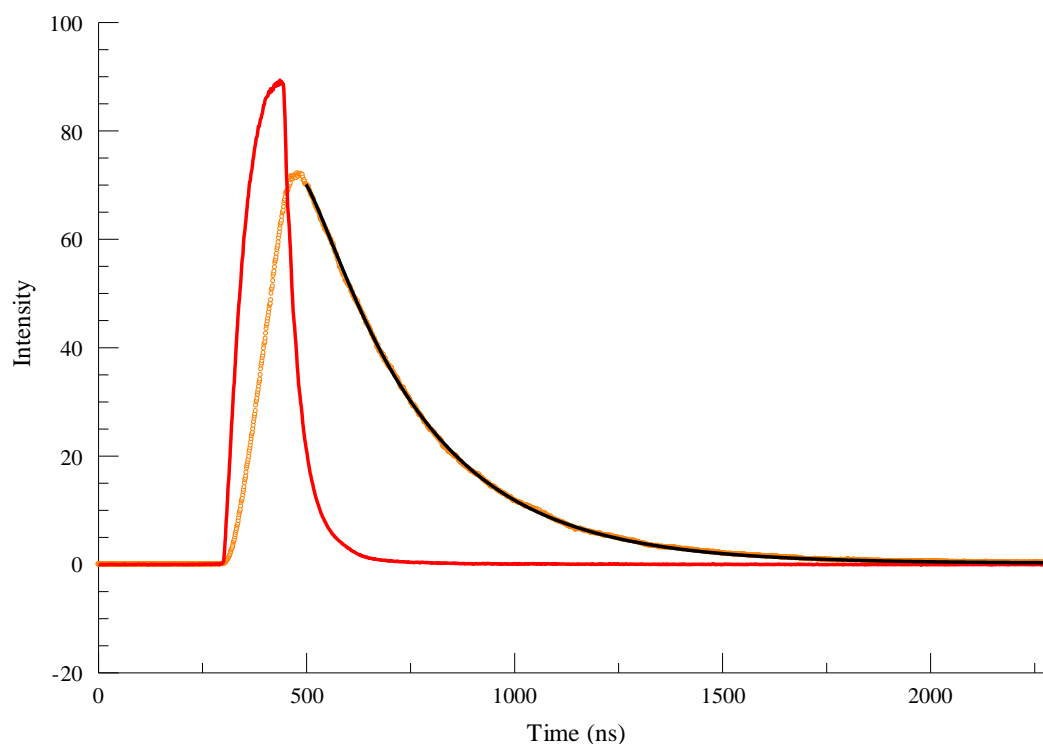


Figure 8: Rose bengal fluorescence, luminescence decay of oxygen purged $\text{Ru}(\text{dpp})_3^{2+}$ /[C6mpy][Tf₂N], and single exponential fit using iterative reconvolution. The open circles are the $\text{Ru}(\text{dpp})_3^{2+}$ luminescence data points, the solid red line is the rose bengal data, and the solid black line is the fit.

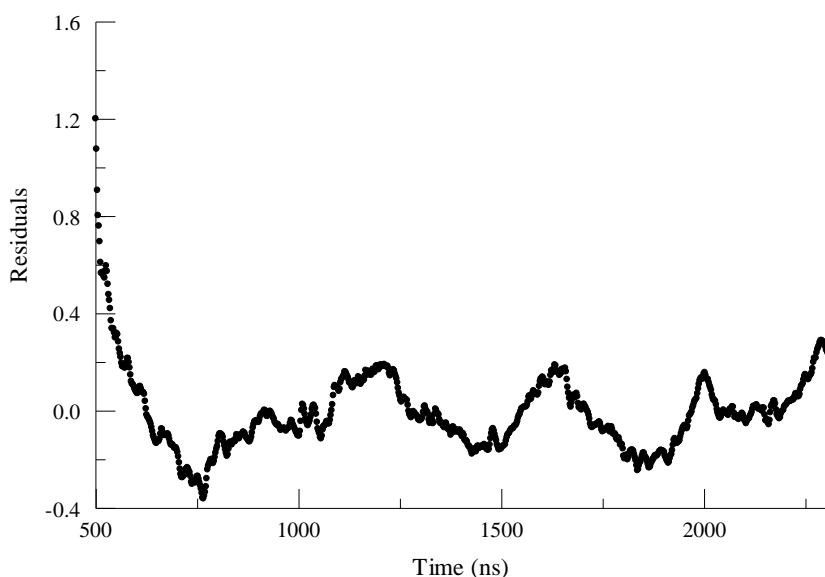


Figure 9: Residuals of single exponential fit to oxygen purged $Ru(dpp)_3^{2+}/[C6mpy][Tf_2N]$ luminescence decay using iterative reconvolution.

A lifetime of 258.7 ± 0.06 ns for the oxygen purged $Ru(dpp)_3^{2+}/[C6mpy][Tf_2N]$ sample was calculated using the iterative reconvolution of the rose bengal decay and a single exponential decay model. As expected, the quality of the fit got poorer as the amount of quenching increased. The luminescence intensity of the samples decreased considerably as the concentration of oxygen increased. The lower the luminescence intensity, the smaller the signal-to-noise ratio becomes. Also,

as the quencher concentration increases the lifetime of the luminescence decreases. The shortened lifetime results in an emission decay profile in which the width of the excitation pulse is comparable to the time scale of the luminescence decay. This greatly distorts the measured decay profile, but doesn't invalidate the deconvoluted lifetimes.

A χ^2 value of 8.433 was obtained for the fit of the oxygen purged $\text{Ru}(\text{dpp})_3^{2+}/[\text{C6mpy}][\text{Tf}_2\text{N}]$ sample using a single exponential decay model. Double and triple exponential decays were also used as test models to fit the decay. However attempts to fit the decay profile using multi-exponentials decay models produced extremely poor fits; more often than not the fits failed to converge indicating that a single exponential is a good decay model and is not the cause of the poorer fit.

Each of the $\text{Ru}(\text{bpy})_3^{2+}$ systems, as well as the oxygen and air purged $\text{Ru}(\text{dpp})_3^{2+}$ decays were analyzed using a single exponential decay model with the iterative convolution function in the PTI software. The goodness of the fits were comparable to the results shown for the air and oxygen purged $\text{Ru}(\text{dpp})_3^{2+}/[\text{C6mpy}][\text{Tf}_2\text{N}]$ systems.

After determining the lifetimes of the Ru(II) complexes in each of the RTILs under nitrogen, oxygen, and air, a three-point Stern-Volmer plot for

each Ru(II)/RTIL was created. The ratio of the unquenched lifetime to quenched lifetimes was plotted versus the respective oxygen partial pressure. Figure 10 shows a typical three-point Stern-Volmer plot of one of the Ru(II)/RTIL systems. The R^2 values for the linear fits to the three point Stern-Volmer equation were >0.9999 .

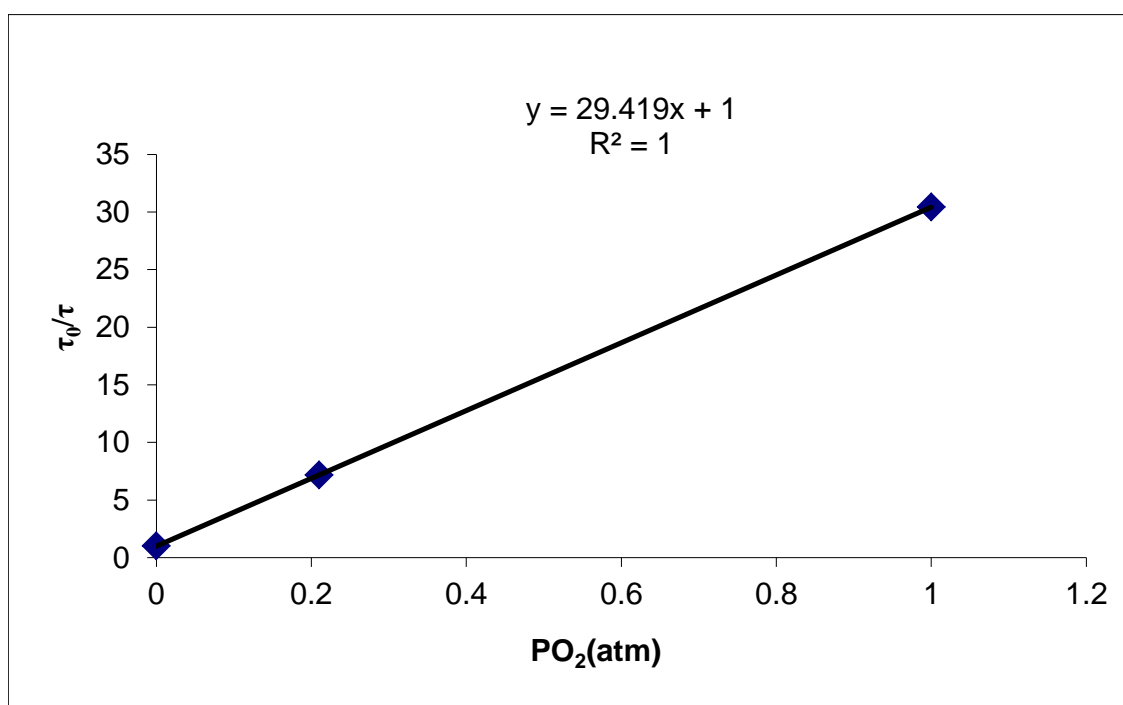


Figure 10: Stern-Volmer plot for $Ru(dpp)_3^{2+}/[Emim][Tf_2N]$. Solid line is the linear fit to the Stern-Volmer equation.

Just as in Chapter 4, here we describe the oxygen quenching of the luminescence lifetime of each system by the Stern-Volmer equation as follows

$$\tau_0/\tau = 1 + K_{sv}P_{\text{oxygen}} = 1 + K_{sv}K_hP_{\text{oxygen}} \quad (2)$$

The lifetimes and true Stern-Volmer constants are displayed in Table 1. At the time of these measurements, no information about the solubility of oxygen in the RTILs studied was known. However, oxygen solubility values were experimentally determined later. The oxygen concentrations used in the following discussion are based on the solubility results detailed in Chapter 8.

Table 1. Oxygen Quenching of Ru(II)/RTIL Systems			
Ru(dpp) ₃ ²⁺	RTIL	τ_0 (μ s)	K_{sv} (M ⁻¹) ^a
	Emmim [Tf2N]	5.9	5676
	C4mpy [Tf2N]	5.7	8362
	C6mpy [Tf2N]	6.1	3364
	C10mpy [Tf2N]	5.7	3798
	P14666 [Tf2N]	4.8	16923
	C3mmim [beti]	5.5	2377
	N4441 [beti]	5.2	7130
	C4mpy [beti]	5.5	
Ru(bpy) ₃ ²⁺			
	P14666 [Tf2N]	0.516	1846
	C4mpy [Tf2N]	0.695	901
	C6mpy [Tf2N]	0.665	435
	C10mpy [Tf2N]	0.650	475
a) Values based on results from measurements discussed in Chapter 8			

The bimolecular quenching rate constant is then given by equation 3 as

$$k_q = K_{SV}/(K_h \cdot \tau_0) \quad (3)$$

For each of the Ru(II)/RTIL systems oxygen quenching is very pronounced even for the highly viscous [N4441][Tf₂N] system where the viscosity is greater than 1200 cP. The oxygen quenching of excited states is considered

to be a diffusion-controlled process. The observed bimolecular quenching rate constant in our systems is therefore limited by the rate of diffusion of the oxygen molecules and the Ru(II) complexes in the RTIL supports. A maximum quenching rate constant, k_{\max} , can be calculated for the diffusion-limited case using the Smoluchowski equation as follows

$$k_{\max} = 4\pi RDN/1000 = 4\pi N(R_f + R_q)(D_f + D_q)/1000 \quad (4)$$

where k_{\max} is the diffusion-controlled rate constant, R is the collision radius which is assumed to be sum of the radii of the Ru(II) complex (R_f) and quencher (R_q), D is the sum of the diffusion coefficients of the Ru(II) complex (D_f) and quencher (D_q), and N is Avogadro's number.¹³ The diffusion of the complex and quencher (oxygen) through the support is dependent upon the properties of the media such as temperature and viscosity. The Stoke-Einstein relation describes the diffusion coefficient of a molecule diffusing through a continuous media as

$$D = \frac{k_b T}{6\pi\eta R} \quad (5)$$

where k_b is the Boltzmann's constant, T is temperature in Kelvin, R is the radius of the diffusing species, and η is the viscosity of the sample.¹³

If the radii of the quencher molecule and the luminophore are considered to be equal, and both species are assumed to be spherically

shaped molecules moving through a continuous media, equations 4 and 5 can be combined to predict the maximum quenching rate constant as

$$k_{max} = 8k_bT / 6000\eta \quad (6)$$

A comparison of the bimolecular quenching rate constants and the predicted maximum diffusion limited bimolecular rate constants based on equation 6 is shown in Table 2.

Ru(dpp)₃²⁺	RTIL	τ_0 (μs)	$^a k_{sv}$ (M^{-1})	$^a k_q \times 10^{-9}$ ($M \cdot s$)⁻¹	$k_{max} \times 10^{-9}$ ($M \cdot s$)⁻¹	η (cP)
	Emmim [Tf2N]	5.9 \pm 0.002	5676	0.96	0.172	38
	C4mpy [Tf2N]	5.7 \pm 0.003	8362	1.47	0.072	94
	C6mpy [Tf2N]	6.1 \pm 0.003	3364	0.55	0.092	73
	C10mpy [Tf2N]	5.7 \pm 0.002	3798	0.67	0.06	110
	P14666 [Tf2N]	4.8 \pm 0.002	16923	3.53	0.0228	290
	C3mmim [beti]	5.5 \pm 0.002	2377	0.43	0.024	277
	N4441 [beti]	5.2 \pm 0.002	7130	1.37	0.0056	>1200
	C4mpy [beti]	5.5 \pm 0.003		1.28	0.04	160
Ru(bpy)₃²⁺						
	P14666 [Tf2N]	0.52 \pm 0.0002	1846	3.58	0.0228	290
	C4mpy [Tf2N]	0.70 \pm 0.0002	901	1.30	0.072	94
	C6mpy [Tf2N]	0.67 \pm 0.0002	435	0.65	0.092	73
	C10mpy [Tf2N]	0.65 \pm 0.0002	475	0.73	0.06	110

a) Values based on oxygen solubility results from measurements discussed in Chapter 8

As seen in Table 2, the bimolecular quenching rate constants of the RTIL systems far exceed the maximum diffusion limited rate constants predicted by the Smoluchowski equation. For example, the quenching rate constant for the N4,4,4,1-beti/Ru(dpp)₃²⁺ system was roughly three orders of magnitude larger than predicted. The discrepancy between the two values is

even larger since k_{\max} was determined based on the assumption that every collision between the Ru(II) complex and an oxygen molecule results in a deactivation of the excited state. One would expect the quenching rate constants to be considerably lower based on viscosity effects alone. Even within the RTILs studied where viscosity values ranged from 38 cP to greater than 1200 cP, there is little difference between the oxygen quenching rate constants of the high viscosity and low viscosity systems. With the viscosity of the RTILs spanning such a wide range, the $1/\eta$ dependence of the diffusion coefficient predicted by the Stokes-Einstein relation should show a pronounced viscosity effect on the bimolecular quenching rate constant.

Lifetime Temperature Dependence Measurements

Diffusion of both the luminescent Ru(II) complex and the oxygen molecule through the RTILs determine the rate at which quenching occurs. Solvent properties such as viscosity and temperature affect the diffusion of the two species and ultimately the luminescence quenching properties. Further investigation of the Ru(II)/RTILs oxygen sensing properties was performed by examining the luminescence lifetime temperature dependence of several Ru(II) systems.

Materials: Five of the Ru(II)/RTILs previously examined were used in the temperature dependence study. The samples consisted of [Ru(bpy)₃]Cl₂ dissolved in [Emim][Tf₂N] and [Ru(dpp)₃]Cl₂ dissolved in the following RTILs: [Emim][Tf₂N], [C10mpy][Tf₂N]), [P14,6,6,6][Tf₂N], and [N4,4,4,1][beti].

Experimental Setup: The experimental setup shown in Figure 1 was slightly modified to allow for varying and monitoring of sample temperature; the rest of the instrumentation and setup remained the same. Sample temperature was monitored with a thermocouple (Type T, Omega Engineering, Inc.) that was immersed directly in the sample. An electronic cold junction compensator was used. The voltage was read with a Keithley 2000 digital multimeter interfaced to the PC through an IEEE 488. A 50 Ω load resistor was used. The samples were placed in a well-stirred water bath heated with a Variac controlled immersion heater. The sample was first cooled below 10° C and then heated at approximately 0.5 °C/min as data was collected. Decays were recorded every 5 °C.

Experimental Procedure: The lifetime measurements of the five Ru(II)/RTIL samples were conducted in a manner similar to which the lifetime standards in Chapter 4 were performed. Separate measurements

under nitrogen, oxygen, and air were made. Samples were bubbled with the respective gas for approximately 25 minutes and then immersed in an ice bath. Samples were cooled slightly below 10 °C. Samples were given several minutes to equilibrate at this low temperature and then the temperature was slowly raised. Starting at 10 °C, a decay curve was recorded at every 5 °C. At each temperature, 300 decays were collected and averaged. When the temperature reached 80 °C, the experiment was stopped. The sample was cooled and the experiment was repeated for the next gas.

At each temperature several profiles were recorded. For all of the $\text{Ru}(\text{bpy})_3^{2+}$ systems, as well as the oxygen and air purged $\text{Ru}(\text{dpp})_3^{2+}$ samples background measurements, rose bengal decay profiles, and sample decays were made at each temperature. To minimize the amount of temperature change between the required measurements at a given temperature, the number of decay averages was reduced from the 2000 averages used during the room temperature study to only 300 averages during the temperature dependence measurements. The long-lived N_2 purged $\text{Ru}(\text{dpp})_3^{2+}$ samples required only background and sample measurements at each temperature. After the necessary measurements were made for each temperature, lifetimes at the corresponding temperatures were determined

using the appropriate fitting function in the PTI software. All decays were single exponential.

Results and Discussion

Figures 11, 12, 13, 14, and 15 show the lifetime temperature and oxygen pressure dependence of $[\text{Ru}(\text{bpy})_3]\text{Cl}_2/[\text{Emim}][\text{Tf}_2\text{N}]$, $[\text{Ru}(\text{dpp})_3]\text{Cl}_2/[\text{Emim}][\text{Tf}_2\text{N}]$, $[\text{Ru}(\text{dpp})_3]\text{Cl}_2/[\text{C10mpy}][\text{Tf}_2\text{N}]$, $[\text{Ru}(\text{dpp})_3]\text{Cl}_2/[\text{P14,6,6,6}][\text{Tf}_2\text{N}]$, and $[\text{Ru}(\text{dpp})_3]\text{Cl}_2/[\text{N4,4,4,1}][\text{beti}]$ respectively. As expected the lifetime decreases as the temperature increases. Also, there is a high degree of oxygen quenching even in the most viscous $[\text{N4,4,4,1}][\text{beti}]$ RTIL at high temperatures. Unlike the viscous glycerol system studied in Chapter 4 in which the difference between the unquenched lifetime and oxygen purged lifetime only became distinguishable at higher temperatures, the high degree of oxygen quenching in the $[\text{N4,4,4,1}][\text{beti}]$ creates a large disparity between quenched and unquenched lifetimes over the entire range of temperatures.

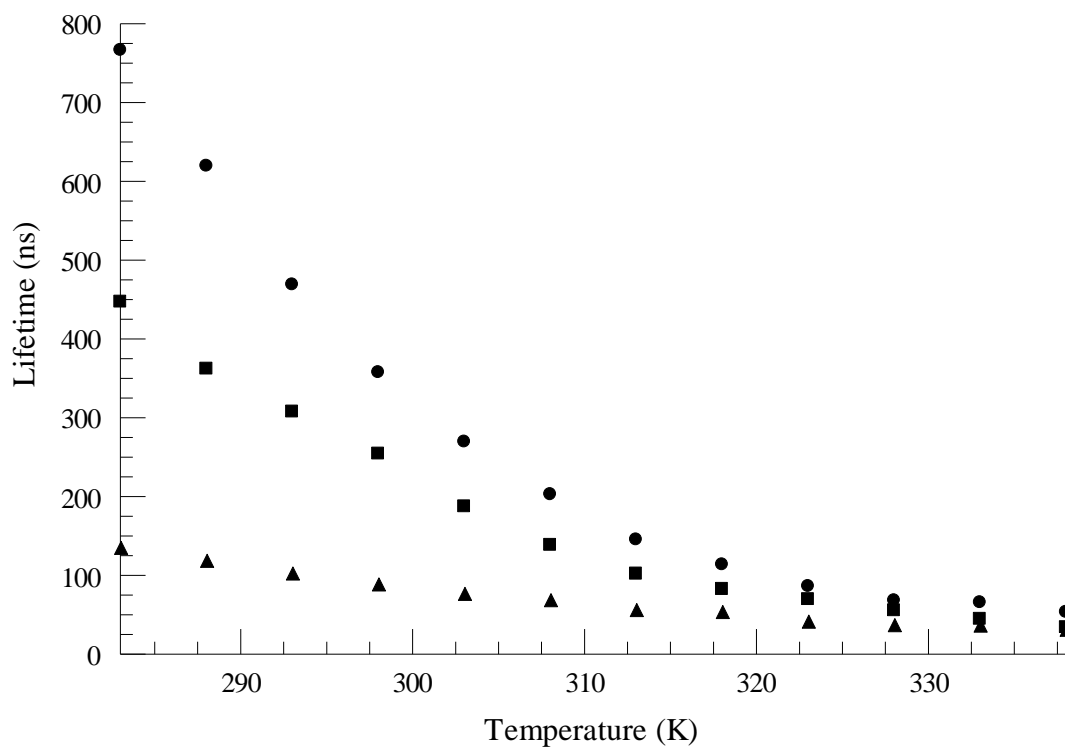


Figure 11: Lifetime temperature dependence of $Ru(bpy)_3^{2+}$ in $[Emim][Tf_2N]$ RTIL for three oxygen partial pressures. The circles are the N_2 purged data points, the squares are the air purged data points, and the triangles are the O_2 purged data points.

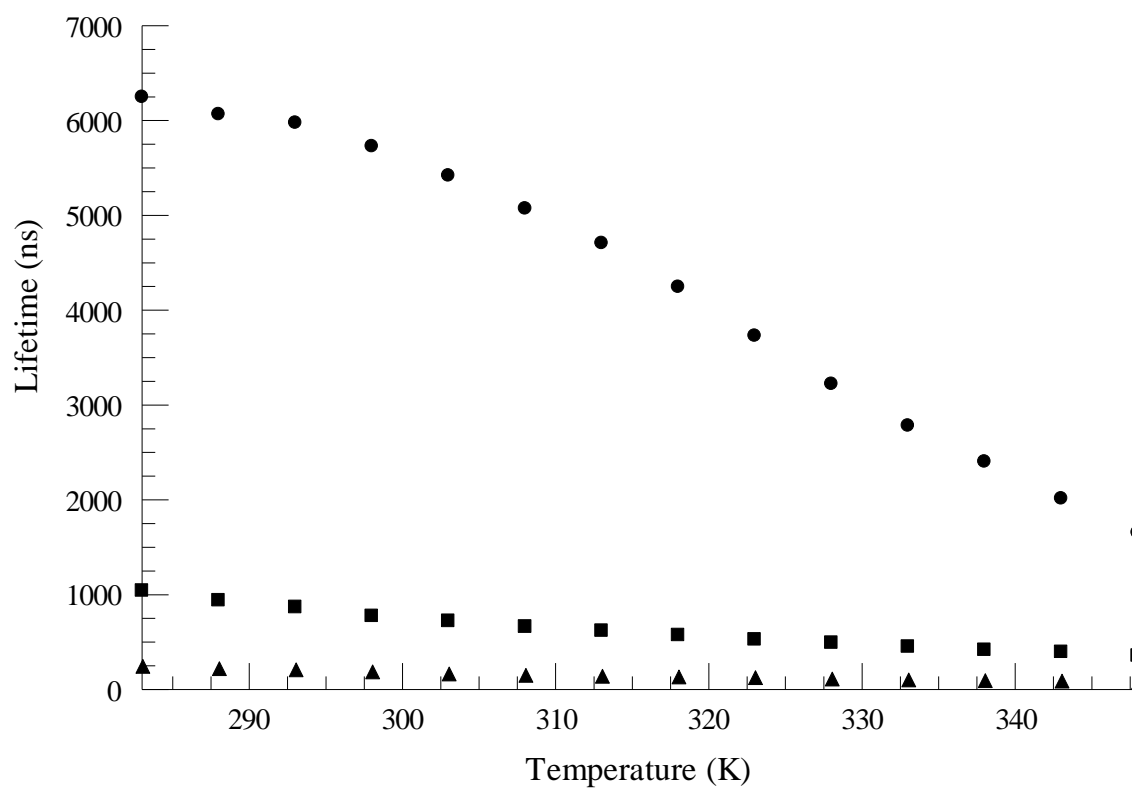


Figure 12: Lifetime temperature dependence of $Ru(dpp)_3^{2+}$ in $[Emim][Tf_2N]$ RTIL for three oxygen partial pressures. The circles are the N_2 purged data points, the squares are the air purged data points, and the triangles are the O_2 purged data points.

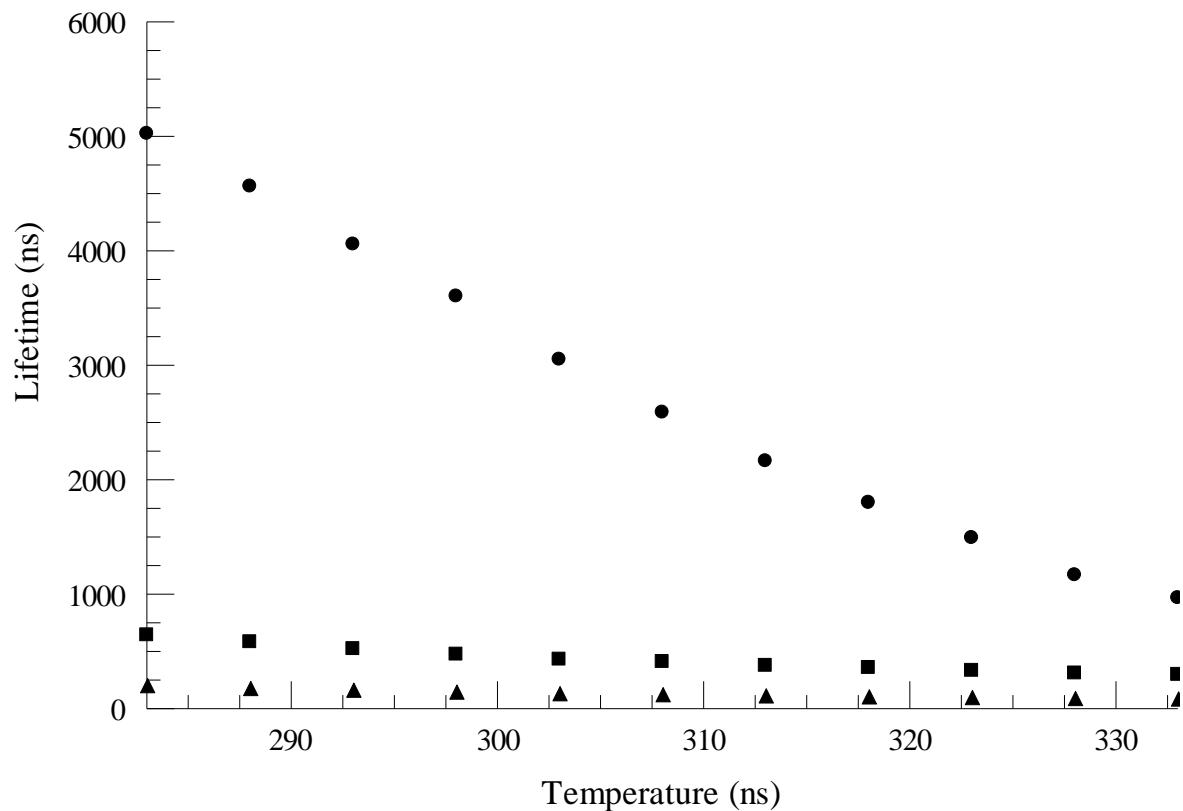


Figure 13: Lifetime temperature dependence of $Ru(dpp)_3^{2+}$ in $[C10mpy][Tf_2N]$ RTIL for three oxygen partial pressures. The circles are the N_2 purged data points, the squares are the air purged data points, and the triangles are the O_2 purged data points.

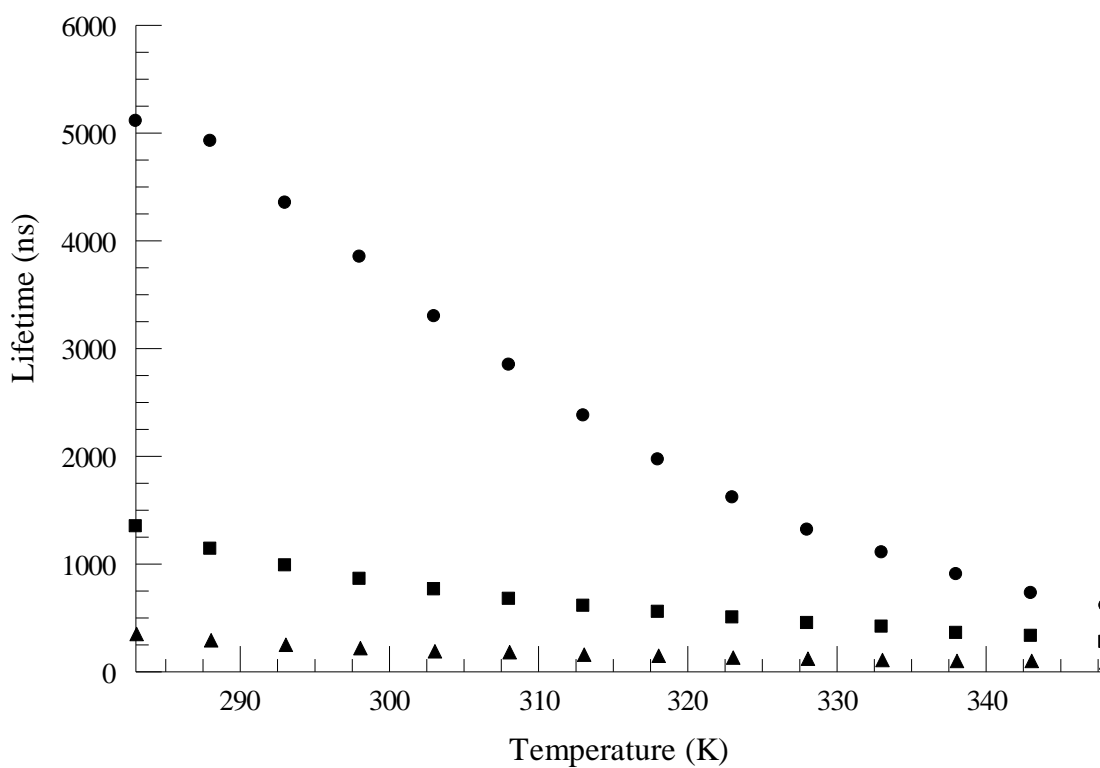


Figure 14: Lifetime temperature dependence of $\text{Ru}(\text{dpp})_3^{2+}$ in $[\text{P14,6,6,6}][\text{Tf}_2\text{N}]$ RTIL for three oxygen partial pressures. The circles are the N_2 purged data points, the squares are the air purged data points, and the triangles are the O_2 purged data points.

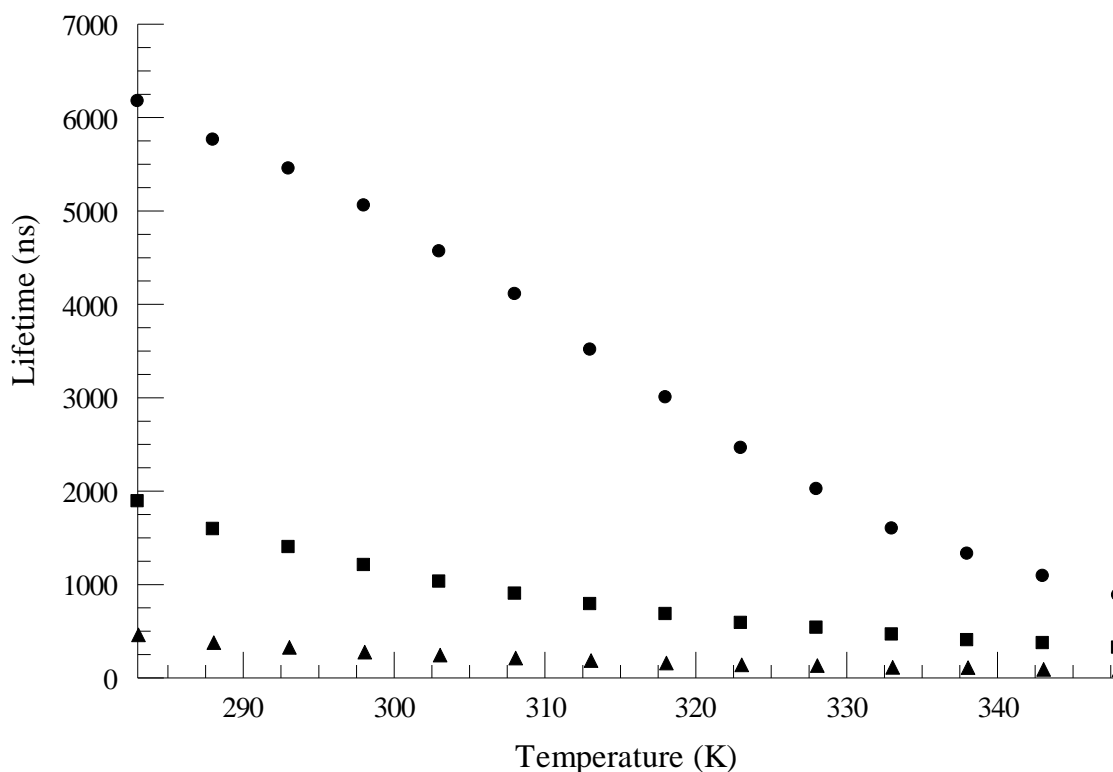


Figure 15: Lifetime temperature dependence of $Ru(dpp)_3^{2+}$ in $[N4,4,4,1][beti]$ RTIL for three oxygen partial pressures. The circles are the N_2 purged data points, the squares are the air purged data points, and the triangles are the O_2 purged data points.

Further investigation was performed by examining the temperature dependence of the deactivation the excited state. The Stokes-Einstein relation predicts a diffusion coefficient temperature and viscosity dependence of $D \propto T/\eta$. As temperature is raised the Stokes-Einstein relation predicts an increase in D . With no other temperature dependent processes, this would cause an increase in the quenching rate constant.

However, as the temperature increases, the oxygen solubility in the RTIL solvents decreases. The lower oxygen concentrations reduces the opportunity for collision with the Ru(II) luminophore, reducing the rate of quenching. In addition, the thermal population of the low lying d-d state is temperature dependent process that further depletes the excited state. The luminescence quenching of the excited MLCT state is a complicated process involving multiple temperature dependent parameters. However, a cursory look at the temperature dependence of the quenching rate constants for the RTILs suggests that there isn't a lot of difference between the systems. Figure 16 shows the temperature dependence of the pseudo bimolecular quenching rate constants for five Ru(II)/RTIL systems.

Conclusion

The oxygen quenching of two Ru(II) in several RTILs was studied. The systems displayed an unusually high degree of quenching considering the extremely viscous nature of the solvents. Also, a brief inspection of the temperature dependence of a few Ru(II)/RTIL samples revealed a similarity between the temperature dependence of the pseudo bimolecular quenching rate constants. Examination of the oxygen diffusion in the Ru(II)/RTIL systems is necessary in order to further investigate and ultimately

comprehend the nature of the anomalously high oxygen quenching witnessed here.

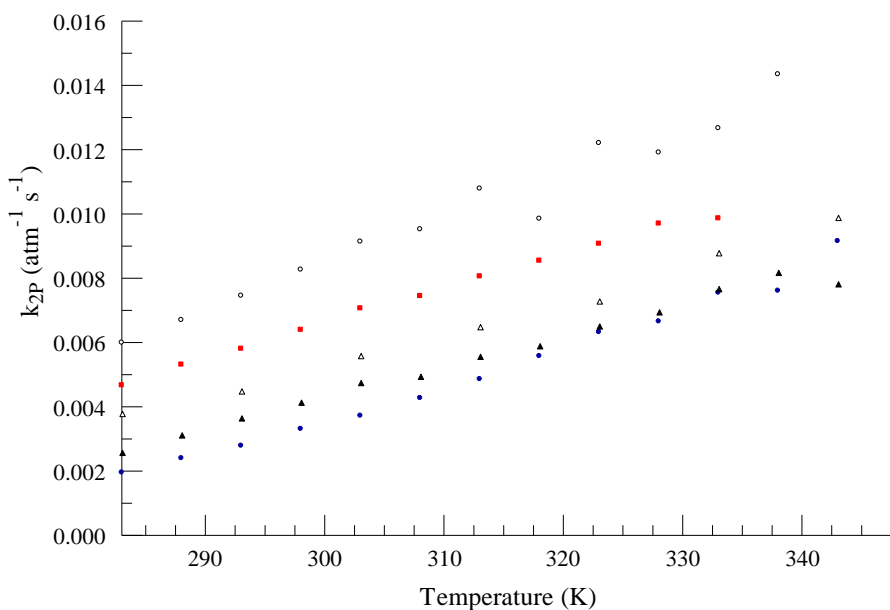


Figure 16: Temperature dependence of pseudo bimolecular quenching rate constant k_{2P} for $Ru(dpp)_3^{2+}$ and $Ru(bpy)_3^{2+}$ in several RTILs. Solid blue circles are $Ru(dpp)_3^{2+}/[N4,4,4,1][beti]$, red squares are $Ru(dpp)_3^{2+}/[C10mpy][Tf_2N]$, solid black triangles are $Ru(dpp)_3^{2+}/[P14666][Tf_2N]$, open triangles are $Ru(dpp)_3^{2+}/[Emmim][Tf_2N]$, and open circles are $Ru(bpy)_3^{2+}/[Emmim][Tf_2N]$.

References – Chapter 6

1. K. Marsh; J. Boxall; R. Lichtenthaler. “Room temperature ionic liquids and their mixtures – a review.” *Fluid Phase Equilibria*. 219, **2004**, 93-98
2. M. Earle; K. Seddon. *Pure Appl. Chem.* 72, **2000**, 1391-1398
3. S. Pandey. “Analytical applications of room-temperature ionic liquids: A review of recent efforts.” *Analytica Chimica Acta*. 556, **2006**, 38-45
4. J. Huddleston; A. Visser; M. Reichert; H. Willauer; G. Broker; R. Rogers. “Characterization and comparison of hydrophilic and hydrophobic room temperature ionic liquids incorporating the imidazolium cation.” *Green Chemistry*. 3, 2001, 156-164
5. H. Matsumoto; H. Sakaebe; K. Tatsumi. “Preparation of room temperature ionic liquids base on aliphatic onium cations and asymmetric amide anions and their electrochemical properties as a lithium battery electrolyte.” *Journal of Power Sources*. 146, **2005**, 45-50
6. E. Rogers; B. Sljucic; C. Hardacre; R. Compton. “Electrochemistry in Room-Temperature Ionic Liquids: Potential Windows at Mercury Electrodes.” *J. Chem. Eng. Data*. 54, **2009**, 2049-2053
7. D. Silvester; R. Compton. “Electrochemistry in Room Temperature Ionic Liquids: A Review and Some Possible Applications.” *Z. Phys. Chem.* 220, **2006**, 1247-1274

8. K. Seddon; A. Stark; M. Torres. "Influence of chloride, water, and organic solvents on the physical properties of ionic liquids." *Pure Appl. Chem.* Vol. 72, **2000**, 2275-2287
9. Lin, C. T.; Boettcher.; Chou, M.; Creutz, C.; Sutin, N. *J. Am. Soc.* **1976**, 98, 6536-44.
10. Picomaster TCSPC Fluorescence Lifetime Spectrofluorometer. Photon Technology International. [Brochure]. Retrieved January 18, 2012. Web Site: <http://www.pti-nj.com/brochures/PicoMaster.pdf>
11. J. Lakowicz. "Principles of Fluorescence Spectroscopy." 2nd ed.; KluwerAcademic/Plenum Publishers: New York, 1999
12. X. Huang; E. Rogers; C. Hardacre; R. Compton. "The reduction of oxygen in various room temperature ionic liquids in the temperature range 293-318 K: exploring the applicability of the Stokes-Einstein relationship in room." *J. Phys. Chem. B.* 113, **2009**, 8953-8959
13. J. Lakowicz. "Principles of Fluorescence Spectroscopy." 2nd ed.; KluwerAcademic/Plenum Publishers: New York, 1999.
14. A. Einstein. *Z. Elektrochem.* 14, **1908**, 235

Chapter 7: Oxygen Diffusion in RTILs: Confocal Fluorescence Microscopy Method

Introduction

To better understand the anomalously high quenching discussed in Chapter 6, where the measured quenching rate constants were as much as three orders of magnitude greater than those predicted for diffusion-limited quenching rate constants, oxygen diffusion in RTILs was examined.

The dynamic quenching of the Ru(II) luminescence by oxygen, in the RTILs systems, is a diffusion-controlled process. That is, in each sensor, the observed quenching rate constant is limited by the rate of diffusion of oxygen and the rate of diffusion of the Ru(II) complex in the RTIL. While the diffusion of the Ru(II) metal complexes is briefly discussed in Chapter 8, far greater attention is given in this chapter to the oxygen diffusion in the RTILs.

As one would reasonably expect, in the RTILs oxygen diffuses much faster than the Ru(II) complexes. As a result, the luminescence quenching in the sensor system is dominated by the rate of oxygen diffusion and not that of the Ru(II) complex diffusion. To study the oxygen diffusion in our Ru(II)/RTIL sensors, a new technique using a commercial con-focal fluorescent microscope was developed and implemented to measure oxygen diffusion coefficients in each of the RTILs.

Fluorescence Microscopy Background

In 1908, more than three centuries after the first optical microscope was made, Köhler and Siedentopf invented the first fluorescence microscope. The cadmium spark, long since abandoned, was the excitation source for this revolutionary instrument. Some of the first major studies involving fluorescence microscopy included Stübel who in 1911 examined the autofluorescence of animal tissue, the first reported autofluorescence in plants by Wilischke in 1914, and the first investigation of the autofluorescence of human tissue by Borst and Königsdorfer in 1929.¹ It's highly unlikely that Köhler and Siedentopf realized at the time that the fluorescence microscope they invented would change the face of research in areas of study such as biology, pharmaceutical, clinical medicine, material science, and others.

There are many different specific applications of fluorescence microscopy. One such technique is Förster (Fluorescence) Resonance Energy Transfer (FRET). In FRET, an excited donor fluorophore transfers energy to an acceptor fluorophore by means of dipole-dipole interactions when the two fluorophores are in close proximity to each other. After excitation by the donor, the acceptor fluorophore subsequently emits a

photon. The distance at which this phenomenon occurs is very specific, typically between 0.5 and 10 nm. This allows FRET to be a very useful tool in the study of biological interactions. For example, DNA and RNA reactions such as hybridization, cleavage, and ligation recombination are processes that are often observed using FRET.¹

Another fluorescence microscopy technique is Total Internal Reflection Fluorescence (TIRF) microscopy. When light is incident on a boundary of lower index of refraction and is at an angle greater than the critical angle, the light will be totally internally reflected. While the incident light is completely reflected, an evanescent wave propagates normal to the surface. The evanescent wave decreases exponentially resulting in a probing depth of tens of nanometers from the slide surface. As a result, TIRF is an extremely powerful tool in the study of surface and near-surface interactions.

There are a number of other fluorescence microscopy techniques, but after introducing the basics of fluorescence microscopy by describing wide-field fluorescence microscopy, the remainder of this section will focus on confocal fluorescence microscopy; which was the major tool used in this research.

Fluorescence microscopy in its most general form is a technique known as wide-field fluorescence microscopy. The very first fluorescence microscopy studies, including those mentioned above, were in fact wide-field fluorescence microscopy experiments. Figure 1 shows the basic operation of a modern wide-field fluorescence microscopy and the major components of a fluorescence microscope. A fluorescence microscope, and each of its parts, operates in practically the same manner as in conventional optical microscopy.

The optics in fluorescence microscopes is far more complex than the depiction in Figure 1; many different lenses and mirrors are used in the focusing, collection, and correction of light in the fluorescence microscope. The condenser, for example, consists of a series of lenses and mirrors that ensures the exciting light illuminates the sample evenly. Also, the objective is typically made up of several lenses as well. The objective lenses are fixed inside one nosepiece. The design of the objective is such that all the lenses move together, therefore maintaining the same focal length. The focal length of an objective is the distance, measured from the center of the objective, at which parallel rays that pass through the objective converge along the optical axis. In a microscope the objective is positioned extremely close to the sample stage, either directly above or below, depending on the type of

microscope. The focus is adjusted by moving the objective vertically, up or down, depending on the microscope design.

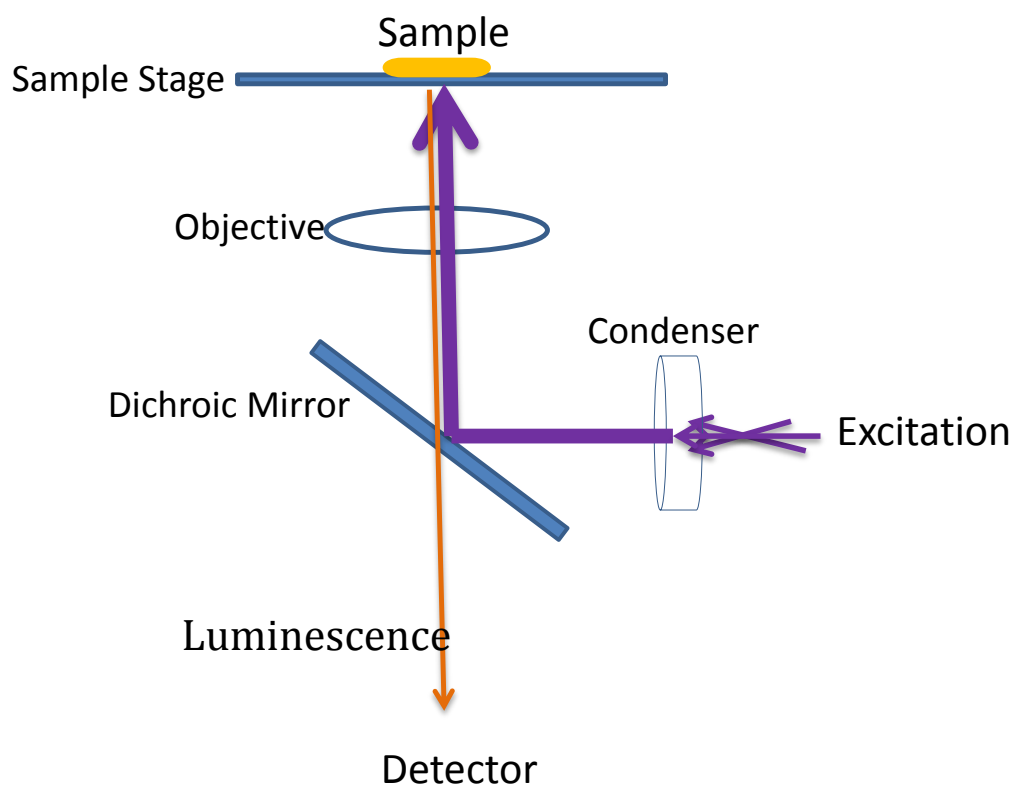


Figure 1: Basic components and operation of a wide-field fluorescence microscope.

Objective lenses are characterized by the medium (water, air, or oil) used in the interface between the objective and sample slide, the magnification, and the numerical aperture (NA). Water and oil objectives increase the NA of the objective by increasing the index of refraction of the

medium between the sample slide and the objective. The numerical aperture is given by equation 1 as

$$NA = n \sin \theta \quad (1)$$

where n is the index of refraction of the medium between the objective and the sample slide, and θ is the half angle of the maximum cone that can enter the objective.²⁻³ The NA is a measure of a lens' light gathering power.

The higher the NA, the better the resolution of the microscope. The resolution (r), which measures the minimum distance between two points on a sample that can still be distinguished from each other, is given by equation 2

$$r = \frac{\lambda}{2NA} \quad (2)$$

where λ is the wavelength of the emitted luminescence. Other lenses are also used in the light pathway to correct for various optical aberrations.⁴

The dichroic mirror is another common component of the fluorescence microscope. Usually these mirrors aren't mentioned when discussing the optics of a fluorescence microscope, but are instead typically listed with the excitation source and filters. The main purpose of the dichroic mirror is to pass the exciting light while blocking the majority of the

scattered exciting light from reaching the detector. Since the intensity of the excitation source will far exceed that of the luminescence intensity from the sample, the addition of the dichroic mirror helps to greatly reduce background.

Since dichroic mirrors aren't 100% selective, fluorescence microscopes have additional emission and excitation filters included. The emission filter works with the dichroic mirror to provide further reduction of any scattered light. The emission filter is chosen such that it passes on to the detector only wavelengths of light near the emission wavelength of the sample. The excitation filter on the other hand is used to prevent light that is not from the excitation source from reaching the sample.

An essential part of any fluorescence microscope is the excitation source. Fluorescence microscopy, as with most luminescence spectroscopy, requires a light source with a high intensity and narrow bandwidth. Some of the most common excitation sources in fluorescence microscopes include lasers, arc lamps, and light emitting diodes. Lasers are inherently monochromatic and intense, making them ideal for fluorescence microscopy. The main disadvantages of lasers are high cost and limited to one wavelength per laser. Arc lamps such as xenon lamps and mercury lamps are commonly used because they provide high intensity exciting light

over a broad range of wavelengths. With arc lamps, filters are used to provide wavelength selection. Light emitting diodes are becoming an increasingly popular excitation source in fluorescence microscopy because of their low cost, many wavelengths to choose from, and relatively high intensities.

The final major part of the fluorescence microscope is the detecting system. Charged Coupled Device (CCD) cameras and PMTs are the two most commonly used detecting devices in fluorescence microscopy. The operation of the PMT was discussed earlier and won't be described again here.

The operation of a CCD camera is as follows. The sensing portion of a CCD camera consists of a two dimensional array of micron-sized photon sensitive semiconductor devices. The fundamental sensor element, which represents a single pixel, is a Metal Oxide Semiconductor (MOS) operating under highly reversed-biased conditions. The surface of the device is actually polysilicon, not metal, and is transparent to light of wavelengths greater than 400 nm.

When photons strike the polysilicon surface, electrons originally accumulated under the gate are provided enough energy to reach the

adjacent depletion region, in the process creating holes in the region under the gate. One electron-hole pair is created for every absorbed photon. The electrons are collected and stored in the potential well created by the applied reverse-biased voltage. For readout the electrons and holes are then controlled by manipulating the external voltage in such a manner to cause the electrons to be transferred along the device substrate. The charges are converted to voltages which are then amplified and digitized.⁵

The components of a fluorescence microscope work together to produce an image created from the luminescence of an excited sample. As illustrated in Figure 1, during operation, light from the excitation source is reflected by the dichroic, through the condenser, and onto the sample. Luminescence from the sample is collected by the objective and focused on the detector. The dichroic mirror is chosen such that it reflects at the wavelength of the exciting light but is transparent to the emitted luminescence.

When a luminescent sample is excited as shown in the setup of Figure 1, luminophores throughout a volume of the sample become excited. As a result, luminophores from the entire excited region emit photons in all directions. The photons that are emitted in the direction along the optical axis are collected and used in the imaging process.

Due to the narrow focus of the objective, photons originating from the focal plane will be sharply focused, while photons originating from above or below the focal plane will be out of focus. This creates a highly blurred image from a large region of the sample. With this setup it is impossible to obtain sharp images from a specific imaging plane due to the many additional photons originating from different regions throughout the sample.

Confocal Fluorescence Microscopy

In 1957, Marvin Minsky developed the very first version of a confocal microscope. Figure 2 illustrates the layout of Minsky's new instrument. In this earliest version of the confocal microscope, one pinhole was placed in front of the light source, creating a single spot of illumination, while another pinhole was placed in front of the detector. The traditional condenser was replaced with a lens identical to the objective that focused the spot onto the sample. The pinhole of the light source, the sample stage, and the pinhole of the detector were placed in series along the optical axis as shown in Figure 2. Each pinhole was located a focal length away from the sample stage and the corresponding objective. Since the objectives were identical, the illuminated spot focused on the sample was at all times an equal distance away from both the light source and the detector.⁶⁻⁷

While both conventional confocal microscopes and fluorescence confocal microscopes today are setup differently than Minsky's original design, the principles of operation remain the same. Figure 3 shows the setup of a typical modern fluorescence confocal microscope. In this setup, a laser is focused to a diffraction-limited spot. If an arc lamp is used instead of a laser, an aperture similar to that in the Minsky setup would be needed in front of the light source to reduce the spatial dimensions of the exciting light to a single spot. The excitation spot is reflected by the dichroic mirror and focused onto the luminescent sample by the objective. Luminescent elements in the small volume element, created by the excitation spot, emit photons in all directions. Scattered light is blocked by the dichroic mirror, while photons emitted from the sample along the optical axis are transmitted. The objective focuses the luminescence to a single diffraction-limited spot on the front of detector. An aperture, positioned in front of the detector, is situated such that it passes light from the focal plane but blocks the light from all other planes above and below the focal plane. In this single objective setup, the aperture in front of the detector and the exciting spot are positioned a focal length distance away from the objective.

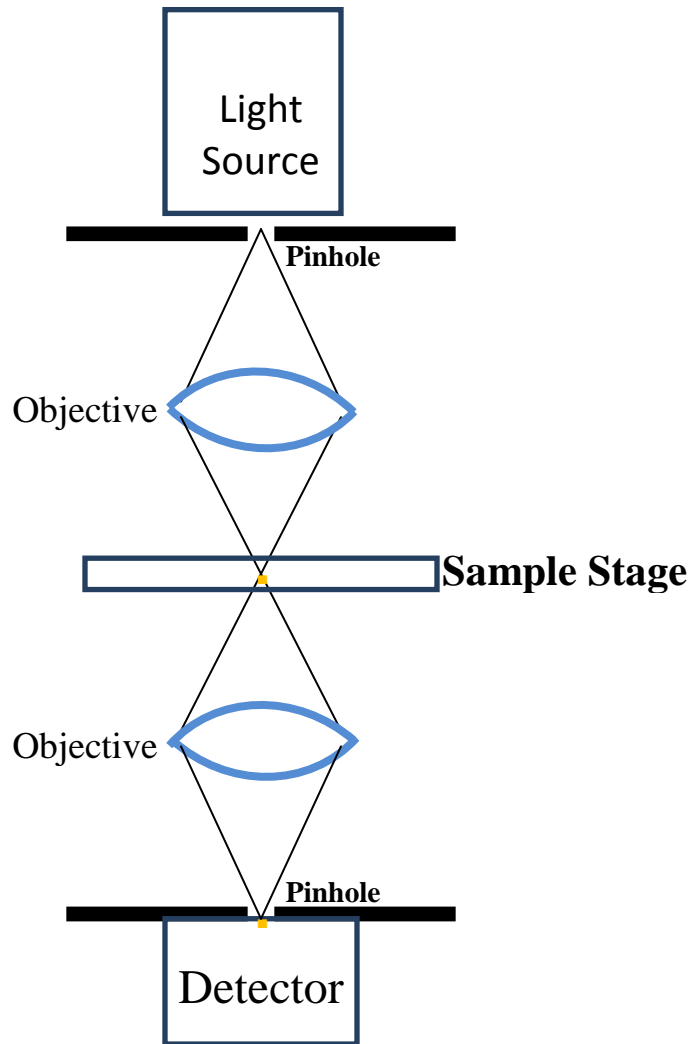


Figure 2: Basic components and operation of the first confocal microscope developed in 1957 by Marvin Minsky.

In wide-field fluorescence microscopy the generated image is produced by photons from the full thickness of the sample. In confocal fluorescence microscopy however, imaging photons come from a very small specified region of the sample. For this reason, in confocal microscopy, the image has to be “built up”. As a result, imaging in confocal fluorescence

microscopy is achieved by either the scanning-stage method or the scanning-beam method.

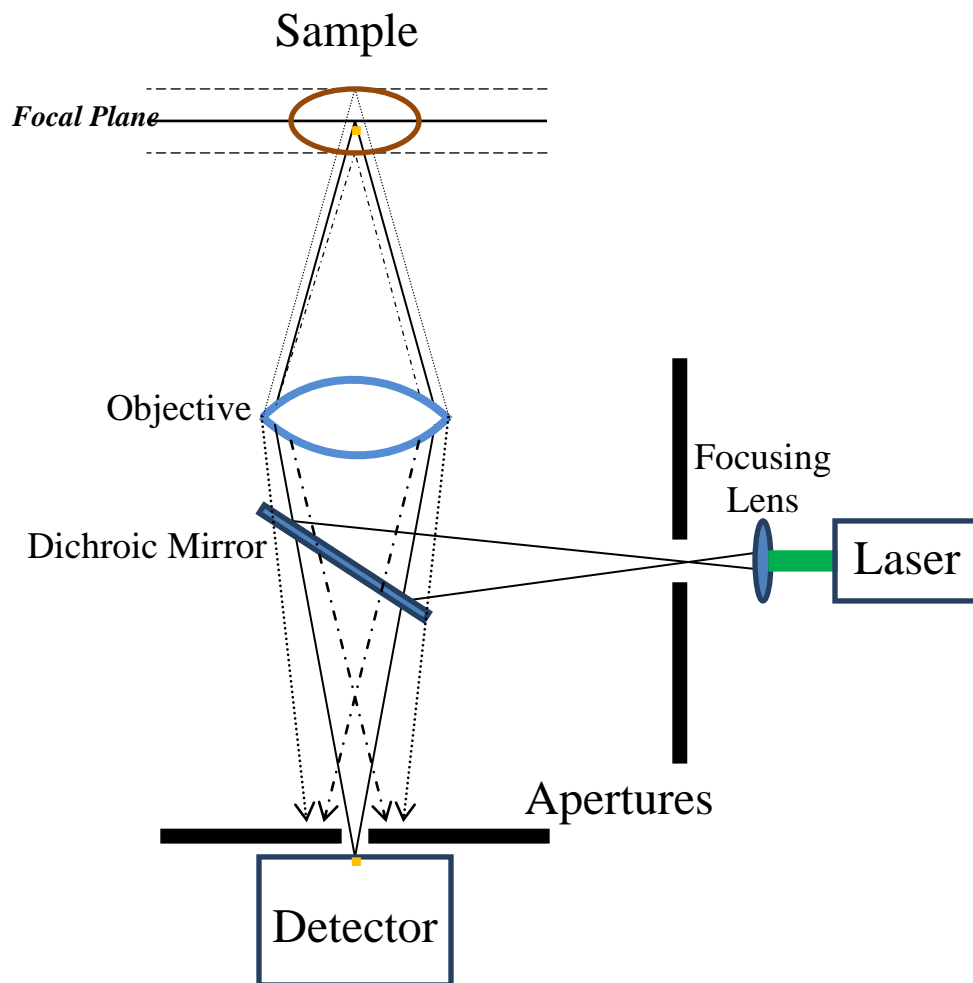


Figure 3: Setup and major components of a typical modern fluorescence confocal microscope.

The scanning-stage method was the first to be employed in confocal microscopy. In this technique, an image is generated by collecting the

luminescence of the sample point by point as the sample stage is moved. A major advantage of this method is that it reduces spherical aberrations because the light always passes directly along the optical axis of the microscope as the sample is moved. Another advantage is that the optics doesn't limit the size of the sample being imaged. The major disadvantage is the length of time required to produce a single image is considerable. Not only does it take a significant amount of time to accurately move the stage in small increments to collect a single image, but often multiple scans of a single frame are necessary to improve the signal to noise ratio. This could result in very long data collection times.⁶⁻⁷

In the scanning-beam technique, the excitation spot is raster scanned on the fixed sample by rotating or vibrating mirrors. The major advantage of this method is that it allows for very fast data collection. The disadvantages are the size limitations due to the scanning optics as well as the increased optical aberrations caused by the deflection of the excitation source.⁷⁻⁹ The latter was one of the problems we encountered during our oxygen diffusion measurements that forced us to modify our experimental setup.

Method Verification by Diffusion of Oxygen in Water

To verify the performance of our system we needed a standard. The diffusion of oxygen in water has been a greatly studied process and was used as the test system. Oxygen in water has an accepted diffusion coefficient value of approximately $2.20 \times 10^{-5} \text{ cm}^2\text{s}^{-1}$ at 25°C .¹⁰ In the following section we describe our newly developed method for measuring oxygen diffusion coefficients and the verification of the method by measuring the oxygen diffusion coefficient in water as a standard.

The following method to measure oxygen diffusion coefficients, developed by our research group, uses con-focal fluorescence microscopy to measure the reduction of luminescence intensity of a luminescent Ru(II) complex at the sample-slide focal plane following a step change in the oxygen quencher concentration at the external interface. From the solution of the Fick's Law diffusion equation, the quenching properties of the luminescent complex, and the sample thickness, the diffusion coefficient is calculated from the time dependence of the emission intensity profile and sample thickness.

This method for measuring oxygen diffusion coefficients using a commercial confocal fluorescence microscope was first developed using a

Ru(II) complex dissolved in water. After perfecting the technique using a conventional solvent, the method was modified to study oxygen diffusion in our RTILs.

Materials: The Ru(II) complex, $\text{Ru}(\text{bpy})_3\text{Cl}_2$, was synthesized by a standard method but is also available commercially.¹¹ Double-distilled water was produced in house. Compressed argon and air gases were purchased from GTS-Welco, Allentown Pa.

Instrumentation: All fluorescence microscopy measurements were carried out using the Leica SP5X confocal microscope shown in Figure 4. The Leica confocal microscope was equipped with a 405 nm diode laser and a white light laser source. The 405 nm diode laser was the excitation source used in all of the following experiments. In the Leica SP5X, filtering of the emission and excitation light is done by acousto-optical filters which replace the beam splitter and filter set.

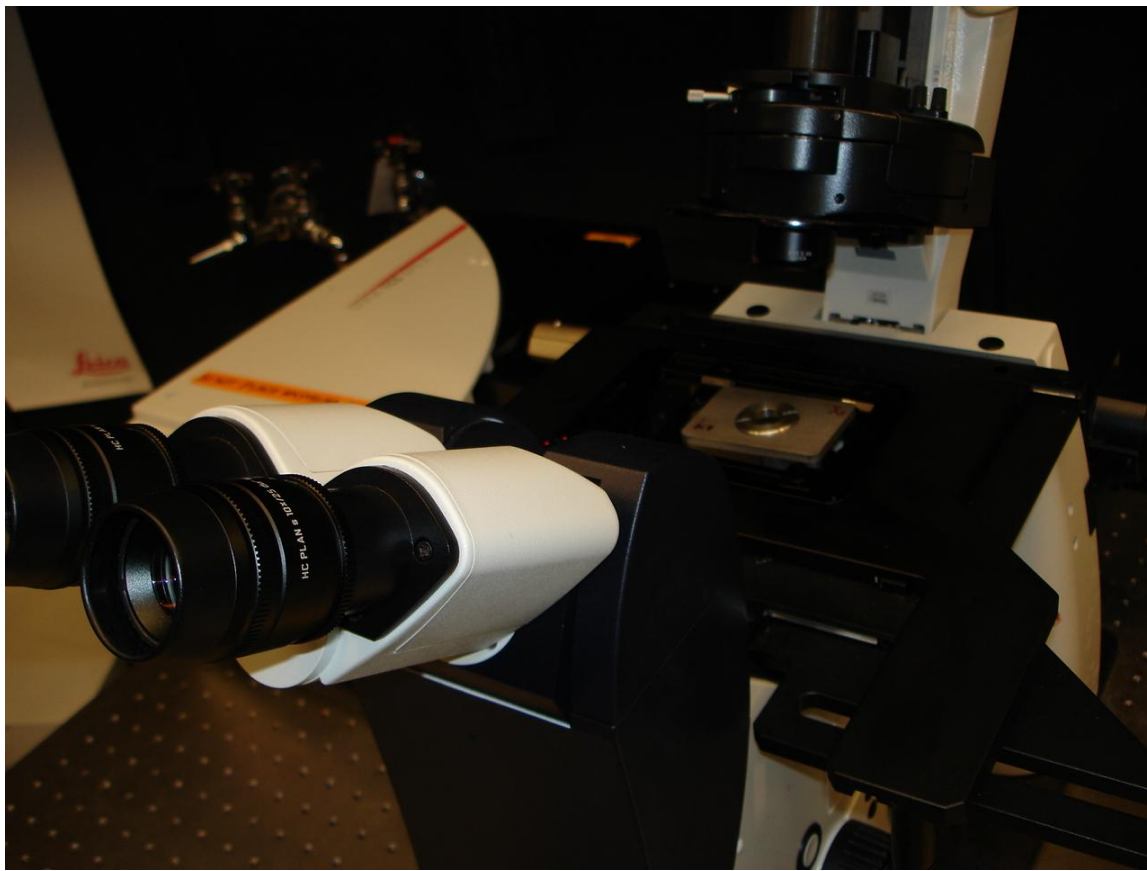


Figure 4: Photograph of the Leica SP5X confocal microscope used to perform diffusion coefficient measurements.

Experimental Setup: Figure 5 is an illustration of the setup used in this experiment. The custom made sample holder consisted of two separate parts, a 20 mm diameter stainless steel hollow well and a flat stainless steel base. The outside of the sample well and the base had matching threads that allowed the well to be screwed into the base.

Tygon tubing was passed through a hole that was cut in the side of a petri dish. The inverted petri dish covered the sample well as shown in

Figure 5. A three-way valve which allowed rapid switching between the argon and air flow, was placed in gas tubing line at the output of the gas cylinders. To prevent evaporation, the gases were first passed through a water bubbler before reaching the sample.

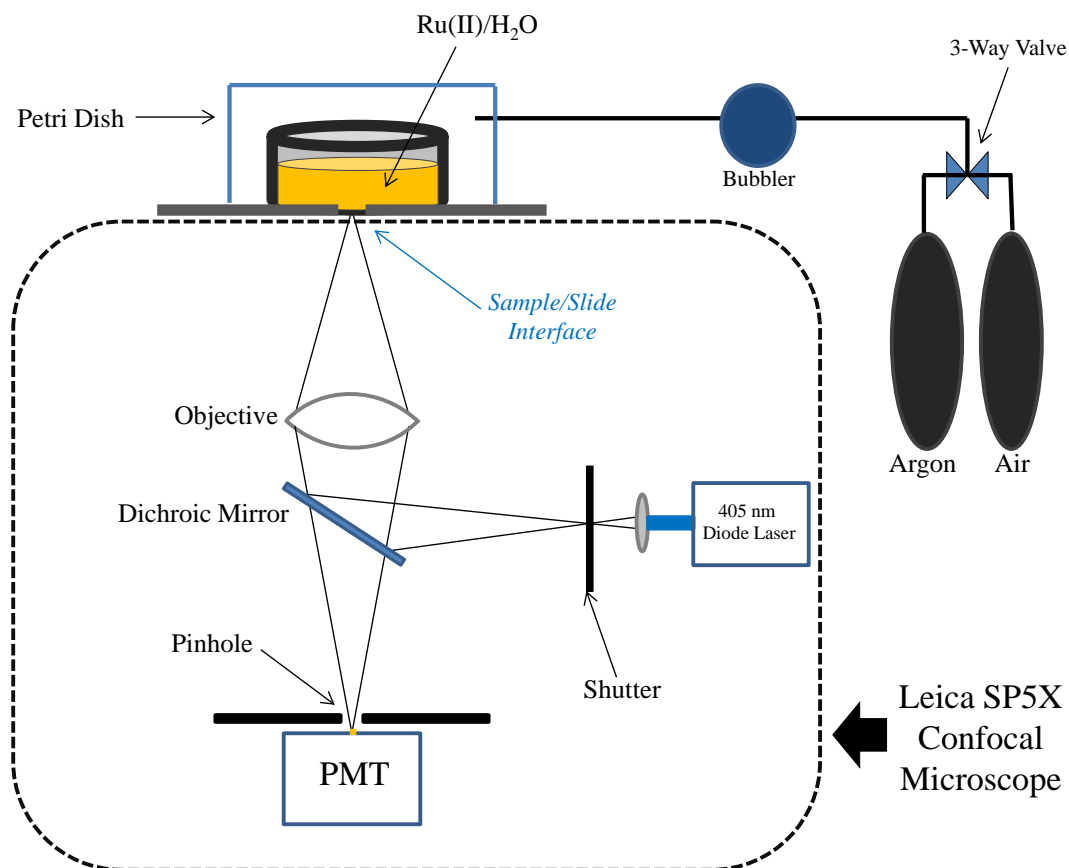


Figure 5: Illustration of the experimental setup used for diffusion coefficient of oxygen in water measurements.

Experimental Procedure: Samples were created by dissolving the Ru(bpy)₃Cl₂ complex in doubly distilled water. For this work exact concentrations of the luminescent transition metal complex was not relevant,

however, samples were made optically dilute while ensuring that the Ru(II) concentrations were still high enough to produce a sufficient signal-to-noise ratio.

A 25 mm diameter circular glass coverslip (Fisher) was placed between the bottom of the well and the sample holder. The sample well was then tightly screwed into the sample holder base, sealing the coverslip at the bottom of the well. Care had to be given such that the well was screwed tightly enough to prevent sample leakage but not too tight to crack the coverslip.

Using a 1 mL disposable syringe, samples were measure and injected into the hollow 20 mm diameter stainless steel well. Prior to the start of the measurements, the argon was disconnected from the tubing line and used to directly purge the samples for approximately 20 minutes. After the direct argon purge, the argon gas was reconnected to the tubing line. The petri dish covering was taped to the sample holder and argon flowed into the sample region.

The sample was placed on the stage of a Leica SP5X confocal microscope. The Leica LAS AF Lite software was used to set the operating parameters and record the data. A 405 nm diode laser was used to excite the sample. To minimize photo-bleaching, laser power was kept below 150 nW.

Typically, a 20x, 0.7 NA, dry objective lens was used to focus the exciting laser line and the resulting Ru(II) luminescence. The spectral range on the PMT was set to 580 – 670 nm.

A single frame image of the emission intensity profile of the Ru(II) complex dissolved in water was recorded by slowly raster scanning across the sample-slide interface. At the beginning of each measurement, the sample-slide interface was found by initially positioning the objective well below sample-slide plane then slowly raising the objective until the interface was reached. When the objective was below the sample-slide interface, the imaging focal plane was below the sample as well. As a result, the intensity (which was simultaneously monitored on the computer screen) was from background only. As the objective was slowly raised, there was an abrupt increase in the image intensity once the interface was reached.

After ensuring the focal plane was indeed at the sample-slide interface, the microscope software was set to allow the data collection for the single frame to take approximately one hour and thirty minutes to complete. The measurement time was controlled by setting the number pixels per line in the image, as well as the number of times each line of the image is averaged during the raster scan. After setting the scanning parameters, the laser focal point was slowly raster scanned across the

sample-slide interface and the focused emission intensity of the deoxygenated Ru(II) sample was recorded.

After approximately twenty minutes of measuring the deoxygenated emission intensity, the three-way valve was quickly switched to allow air to flow through the system while at the same time stopping the argon flow to the sample. At the exact time the argon flow was replaced with air, the laser shutter was quickly cycled closed and back open as a stop watch was simultaneously started. The close/open cycling of the laser shutter briefly stopped the excitation of the sample and thus the luminescence. This produced a dark line in the recorded image that was later correlated to the time oxygen was first introduced at the sample's external interface.

As oxygen diffused through the sample, the emission intensity was recorded until the single frame was complete. At which time the stop watch was immediately stopped and the total measurement time was recorded. A single frame (false color) image of the Ru(II) complex is shown in Figure 6.



Figure 6: False color image of Ru(II) emission intensity following a step change in oxygen concentration at the external surface of the sample well.

The size of the image, the speed of the raster scanning, and the number of raster scanned line averages determined the total time it took to produce the image. The total measurement time had to be long enough to obtain ample oxygen diffusion to the sample-slide interface. The initial measurements taken on the Leica confocal microscope were made before the system was modified and the laser scan speed was fixed at 400 Hz, leaving the number of pixels in the image and number of line averages as the only

adjustable parameters. Limitations in the Leica software hindered our ability to achieve images with large number of pixels and low number of line averages. Typically in the single frame measurements, each line of a 4096 x 4096 pixel image was average 512 times. Due to the large number of line averages, photo-bleaching was of some concern. However, the low laser operating power and the natural solvent motion helped minimize the amount of photo-beaching that occurred. In addition, the confocal nature of the instrument, as described earlier, ensures that as the sample is raster scanned a fresh part of the sample is constantly being excited.

To manipulate the data, the recorded images like the one shown in Figure 6, were exported as a Tagged Image File Format (TIFF) and opened using Image J software. The raw data from each TIFF image was then saved as a text file and opened using Microsoft Excel. This process converted the intensity of each pixel in the image into a corresponding number value in an $n \times m$ matrix. Where n is the number of rows and m is the number of columns. The values in each of the columns were summed together to create a single column. The single column intensity values were then plotted versus the stopwatch recorded time, with start time being marked by the dip in intensity caused by the closing and reopening of the laser shutter, and time intervals determined by the number of rows in the summed column. The

peak intensity was normalized to 1 for data analysis purposes and the resulting intensity versus time profile is shown in Figure 7.

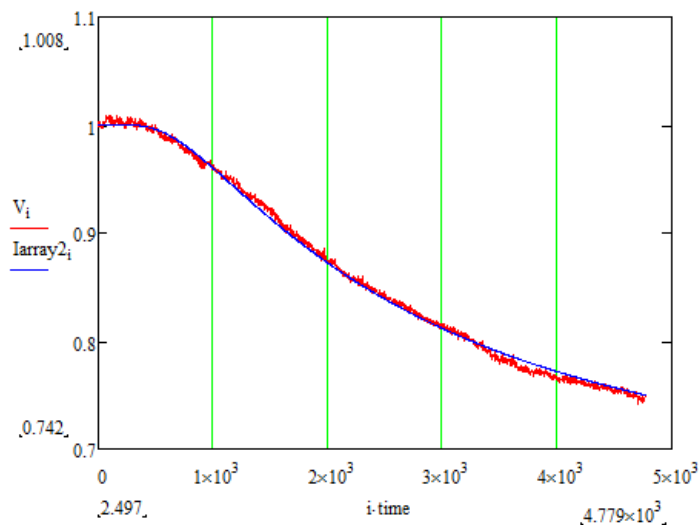


Figure 7: Intensity versus time profile for $Ru(bpy)_3^{2+}$ in water following a step change in oxygen concentration at the external surface of the sample. Red is the experimental data and blue is the best fit. Data are taken directly from the Mathcad fitting program.

As seen in Figure 7 the emission intensity, as measured at the sample-slide interface, remains at a constant value for a finite period after changing from argon to air flow. This is because the system is initially free of oxygen and it takes a finite amount of time after the gas flow is switched from argon to air for the oxygen to travel from the external surface to the monitored sample-slide interface. As oxygen diffuses through the sample and reaches

the interface, the emission intensity decreases as the oxygen concentration increases.

Data Analysis: During the data analysis it was assumed that the Ru(II) complex was uniformly doped throughout the sample. It was also assumed that the quenching properties at the sample interface, as well as throughout the bulk solution, did not vary. Simply stated, as the laser excitation beams was rastered scanned across the sample, the luminescence properties as measured at the sample-slide interface represented those of the entire sample.

As discussed in Chapter 3, the emission intensity of the Ru(II) complex is dependent upon the oxygen concentration in the sample and is given by the Stern-Volmer equation as follows

$$\frac{I_0}{I} = 1 + K_{SV}[O_2] \quad (3)$$

where I_0 is the unquenched emission intensity, I is the quenched emission intensity, K_{SV} is the Stern-Volmer quenching constant, and $[O_2]$ is the oxygen concentration (or partial pressure). Initially, before the experiment is started, the oxygen concentration throughout the sample is zero. When the experiment is begun, the oxygen concentration profile throughout the sample continually changes as oxygen diffuses through the sample. The oxygen

concentration in equation 3 can be found at all times of the measurement by using the appropriate solution to Fick's Law.

Using an expression describing the diffusion in an infinite plane sheet against an impermeable barrier-the oxygen concentration (or partial pressure) in equation 3 was given by

$$\frac{C - C_0}{C_1 - C_0} = \sum_{n=0}^{\infty} (-1)^n \operatorname{erfc} \frac{(2n + 1)l - Xl}{2(Dt)^{1/2}} + \sum_{n=0}^{\infty} (-1)^n \operatorname{erfc} \frac{(2n + 1)l + Xl}{2(Dt)^{1/2}} \quad (4)$$

where C is the oxygen concentration at the sample-slide interface at time t , C_0 is the initial oxygen concentration in the bulk sample, C_1 is the oxygen concentration at the external surface, erfc is 1 minus the error function, D is the diffusion coefficient (in cm^2/s), t is time (in s), X is the normalized depth given by x/l , x is the position, and l is the thickness of the sample (in cm).

In the case of our measurements, all samples are initially purged with argon thereby removing any ambient oxygen in the system. As a result, the initial oxygen concentration for our experiments is zero. Also, following the step change in oxygen at the external surface the oxygen concentration at the surface remains constant. Therefore, simplifying equation 4 and solving for

the oxygen concentration at all times during the measurement yields the following equation

$$C = \left[\sum_{n=0}^{\infty} (-1)^n \operatorname{erfc} \frac{(2n+1)l - Xl}{2(Dt)^{\frac{1}{2}}} + \sum_{n=0}^{\infty} (-1)^n \operatorname{erfc} \frac{(2n+1)l + Xl}{2(Dt)^{\frac{1}{2}}} \right] C_1 \quad (4)$$

Substitution of equation 4 into the Stern-Volmer equation gives the desired intensity as a function of changing oxygen concentration profile that was used to fit our measurements. The fitting was performed using a Mathcad program developed by Kneas et al. that utilizes the combination of equations 4 and 5.¹¹

The emission intensity as a function of time measured at the sample-slide interface was fit using the Kneas Mathcad routine. The thickness, l , of each sample was determined by the volume of sample, the diameter of the well, and the density of the solution. The oxygen quenching sensitivity, S , for each measurement was calculated by

$$S = I_0 / I_{final} - 1 \quad (5)$$

where I_0 is the average value of the unquenched intensity before the step change in oxygen concentration, I_{final} is the final intensity value. The D

values were the only adjustable parameters in the routine. The χ^2 for the fitting routine was given by

$$\chi^2 = \sum_{t=0}^{t_{final}} (I_{calc}(t, D) - I_{exp})^2 \quad (6)$$

where I_{calc} is the intensity calculated by the Kneas model, and I_{exp} is the experimentally measured emission intensity recorded at the sample-slide interface. The χ^2 was minimized and the values for D were calculated from the best fit to the experimental data.

Table 1 shows the calculated diffusion coefficients for oxygen in water. The measurements made using the confocal fluorescence microscopy method were made on three separate dates.

Table 1. Confocal fluorescence microscopy diffusion coefficient measurements for oxygen in water					
Date	Aug. 4, 2010	Aug. 6, 2010	Sept. 1, 2010	Average	SD
D (cm ² s ⁻¹)	1.95 x 10 ⁻⁵	2.58 x 10 ⁻⁵	1.77 x 10 ⁻⁵	2.10 x 10 ⁻⁵	4.25 x 10 ⁻⁶

The diffusion coefficient of oxygen in water was determined to be $2.10 \pm 4.25 \times 10^{-5} \text{ cm}^2\text{s}^{-1}$. This average value is in good agreement with accepted literature value of $2.20 \times 10^{-5} \text{ cm}^2\text{s}^{-1}$ at 25° C.¹⁰. While the newly developed technique produced good results, factors such as temperature can influence the accuracy and precision of the measurements. As discussed in previous chapters, the oxygen quenching of Ru(II) is temperature dependent. While all measurements were made at room temperature, there was no

attempt to control the temperature of the sample. Further, variations in sample volume will lead to variations in the height. Such variations will contribute to the accuracy and precision of the technique. The accuracy and precision of our results, as demonstrated in Table 1, gives us confidence in our newly developed method.

Oxygen Diffusion in RTILs

The confocal fluorescence microscopy method created to examine the oxygen diffusion samples in our various Ru(II)/RTIL systems was tested using Ru(bpy)₃Cl₂ dissolved in water. RTILs, however, are not conventional solvents. While the method had to be modified again to account for the unique properties of RTILs, the basis of the measurements remained the same. The diffusion-controlled oxygen quenching of the Ru(II) luminescence in the RTILs systems was utilized in the confocal fluorescence microscopy method to measure oxygen diffusion coefficients in each of our RTILs.

Materials: Each sample consisted of a small amount of ruthenium complex tris-(4,7-diphenyl-1,10-phenanthroline)ruthenium(II) dichloride, [Ru(dpp)₃]Cl₂, dissolved in 0.2 mL of RTIL. The Ru(II) complex was from GFS Chemicals Inc. The RTILs: 1-butyl-1-methylpyrrolidinium

bis(trifluoromethanesulfonyl) imide ([C4mpy][Tf₂N]), 1-butyl-1-methylpyrrolidinium bis(pentafluoroethylsulfonyl) imide ([C4mpy][beti]), 1-hexyl-1-methylpyrrolidinium bis(trifluoromethanesulfonyl) imide ([C6mpy][Tf₂N]), 1-decyl-1-methylpyrrolidinium bis(trifluoromethanesulfonyl) imide ([C10mpy][Tf₂N]), 1-propyl-3-methylimidazolium bis(pentafluoroethylsulfonyl) imide ([C3mimm][beti]), 1-ethyl-3-methylimidazolium bis(trifluoromethanesulfonyl) imide ([Emim][Tf₂N]), methyl-tributylammonium bis(pentafluoroethylsulfonyl) imide ([N4,4,4,1][beti]), and trihexyl-(tetradecyl)phosponium bis(trifluoromethanesulfonyl) imide ([P14,6,6,6][Tf₂N]) were all obtained courtesy of Dr. Gary Baker, Oak Ridge National Laboratory. The compressed argon and air gases were purchased from GTS-Welco, Allentown Pa. Due to the extremely small sample size, the Ru(II) concentrations for these experiments were not measured. However, samples were made optically dilute while ensuring that the Ru(II) concentrations were still high enough to produce a sufficient signal to noise ratio.

Experimental Setup: The setup used for examining the diffusion of oxygen in our RTIL systems is illustrated in Figure 8. Samples were placed in a custom made hollow 8 mm diameter stainless steel well. Use of the 20 mm diameter sample holder from the water measurements would have

required volumes of sample significantly larger than the amounts readily available to us. Similar to the previous sample holder, the outside of the hollow sample well contained threading that matched the base of the sample holder. A 25 mm diameter circular glass coverslip (Fisher) was placed between the bottom of the hollow well and the base. The coverslip was secured in place by carefully screwing the hollow sample well into the base of the sample holder.

Separate tubing for the air and argon gases was used. Tubing for the air flow ran from the air cylinder to the top of sample well. The air tubing was positioned so that when the air valve was opened, air would flow to the top of the sample well. The air flow was kept at very low rate to prevent disturbing the external surface of the sample.

0.9 mm diameter Teflon tubing was connected to the sample side of the argon gas tubing line. The outlet of the Teflon tubing was position at the bottom of the sample. The argon gas was bubbled directly to the bottom of the sample ensuring that the entire sample was purged.

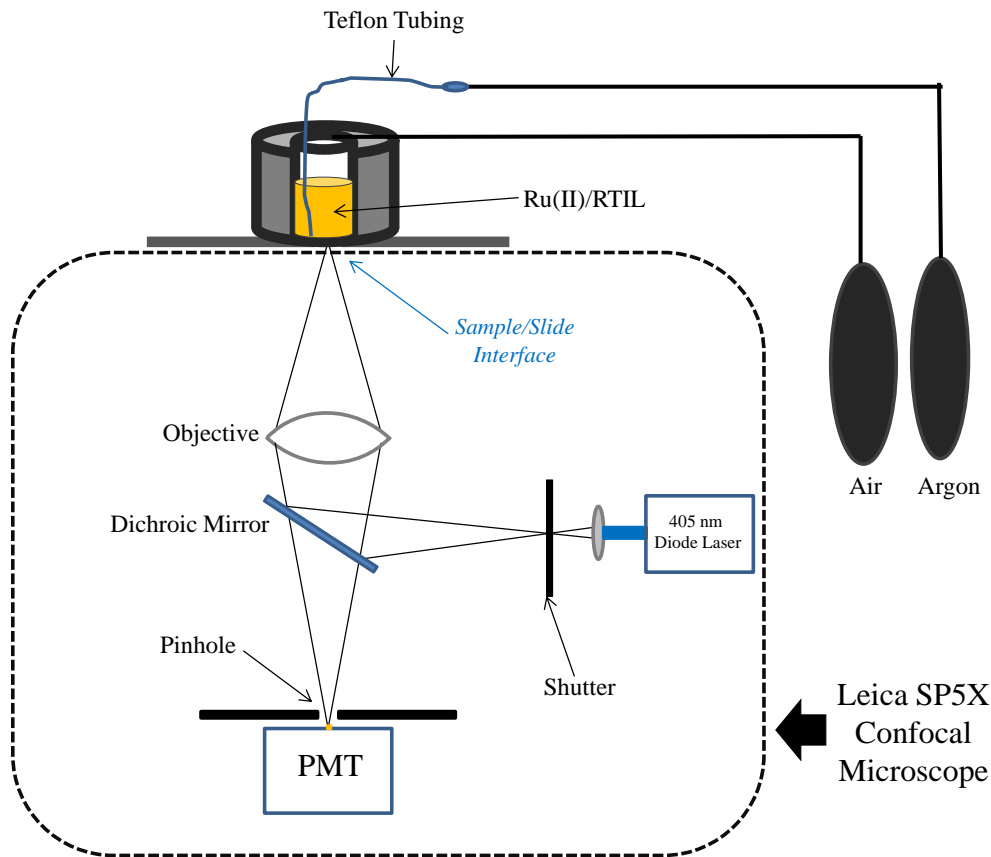


Figure 8: Illustration of the experimental setup used for the oxygen diffusion in RTILs measurements.

Experimental Procedure: For each measurement, small amounts of $\text{Ru}(\text{dpp})_3\text{Cl}_2$ was dissolved in a given RTIL. A 1 mL disposable syringe was used to measure 0.2 mL of Ru(II)/RTIL sample. To ensure that the RTILs were completely deoxygenated, samples were purged with argon for approximately 30 minutes while still in the narrow syringe. After direct purging in the syringe, samples were injected into the hollow 8 mm diameter sample well. The argon purge was continued in the sample well. The 0.9 mm

Teflon tubing used for the argon purge was positioned at the bottom of the sample well, in direct contact with the coverslip. The viscous nature of the RTILs required that the argon purge take place from the bottom of the samples. Results not presented in this work showed that unless the argon gas was bubbled at or near the bottom of the sample, the RTILs would never be completely purged.

Samples were placed on the stage of the commercial Leica SP5X confocal microscope shown in Figure 4. The Leica LAS AF Lite software was used to set the operating parameters and record the luminescence intensity. A 405 nm diode laser was used as the excitation source. The laser power was kept below 150 nW. A 20x, 0.7 NA, dry objective lens was used to focus the laser onto the sample as well as focus the resulting Ru(II) emission on the detector. The spectral range on the PMT was 580 – 670 nm. The laser scan speed was 1400 Hz. The Leica software was set to collect a 16x16 pixel image of the Ru(II) emission at the sample-slide interface every 30 seconds for 2 hours and 30 minutes. The fast laser scan speed and small image size helped minimize photo-bleaching of the samples.

At the start of each measurement, the emission intensity of the argon purged Ru(II)/RTIL sample was recorded for approximately ten minutes. The Teflon tubing was then quickly removed from the sample while

simultaneously starting the air flow. The time and frame of the change in gas flow was noted and later taken to be $t=0$ for the oxygen diffusion calculations. After the gas flow was change from argon to air, oxygen began to diffuse through the sample. Collection of emission intensity images every 30 seconds continued until the program automatically stopped at the expiration of the 2 hour and 30 minute experiment time.

The series of 16x16 pixel intensity images for each experiment were exported as Tagged Image File Format (TIFF) and opened using Image J software. The raw data from each TIFF image was then saved as text file and later opened using Microsoft Excel. In Excel the 256 intensity values from each 16x16 pixel image were summed together resulting in a single intensity value per frame. Each frame was then correlated to its experiment time with $t=0$ being the frame at which the gas was switched from argon to air.

Results and Discussion

The intensity versus time data was analyzed using the method detailed in the previous section. The Stern-Volmer quenching of the Ru(II) luminescence intensity at the slide-sample focal plane following a step change in the oxygen concentration at the external interface was combined with the solution of the Fick's Law diffusion equation to determine oxygen

diffusion coefficients in each RTIL. Figures 9 – 16 show the intensity versus time profiles of the $\text{Ru}(\text{dpp})_3^{2+}$ emission in all RTILs studied.

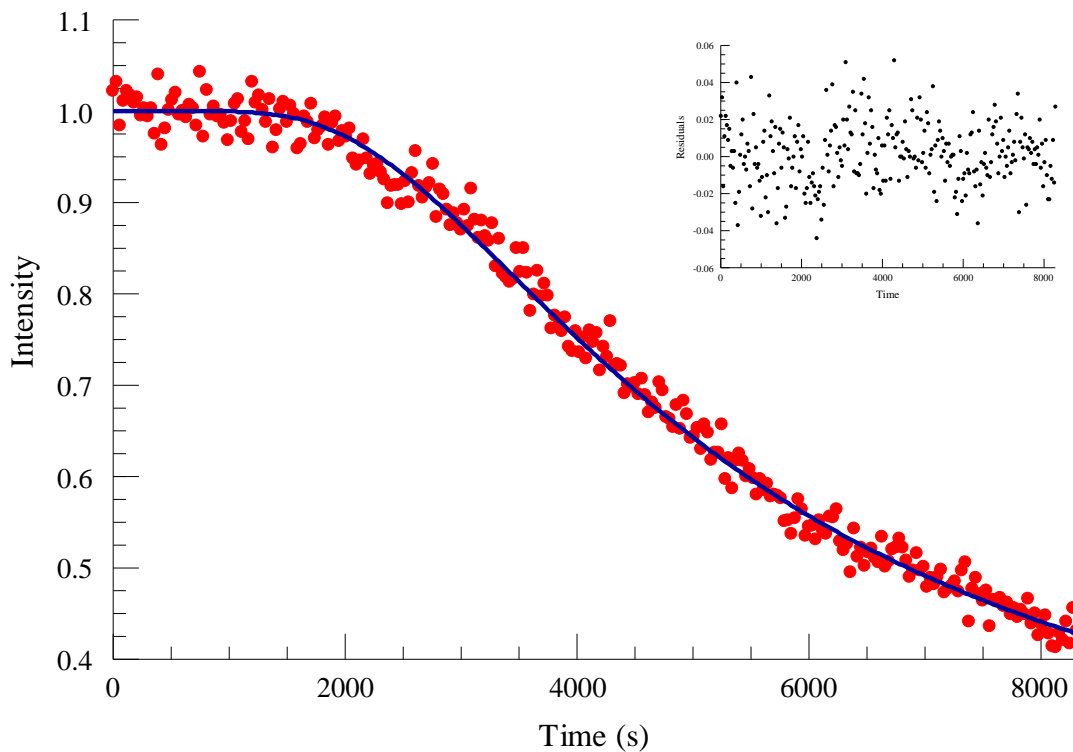


Figure 9: $\text{Ru}(\text{dpp})_3\text{Cl}_2/[\text{C6mpy}][\text{Tf}_2\text{N}]$ sample- luminescence intensity versus time profile following a step change in oxygen concentration and fit to the diffusion model. Dots are the experimental data and solid line is the best fit to the diffusion model. Included in the top right corner of the figure are the residuals of the fit.

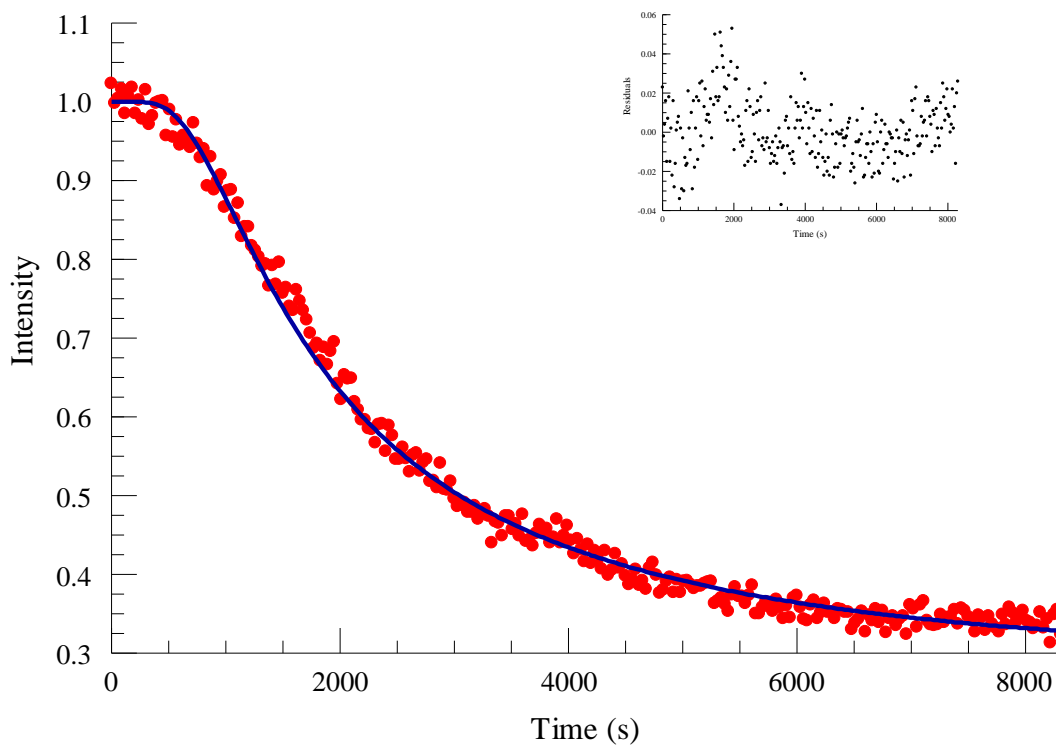


Figure 10: $Ru(dpp)_3Cl_2/[C10mpy][Tf_2N]$ sample- luminescence intensity versus time profile following a step change in oxygen concentration and fit to the diffusion model. Dots are the experimental data and solid line is the best fit to the diffusion model. Included in the top right corner of the figure are the residuals of the fit.

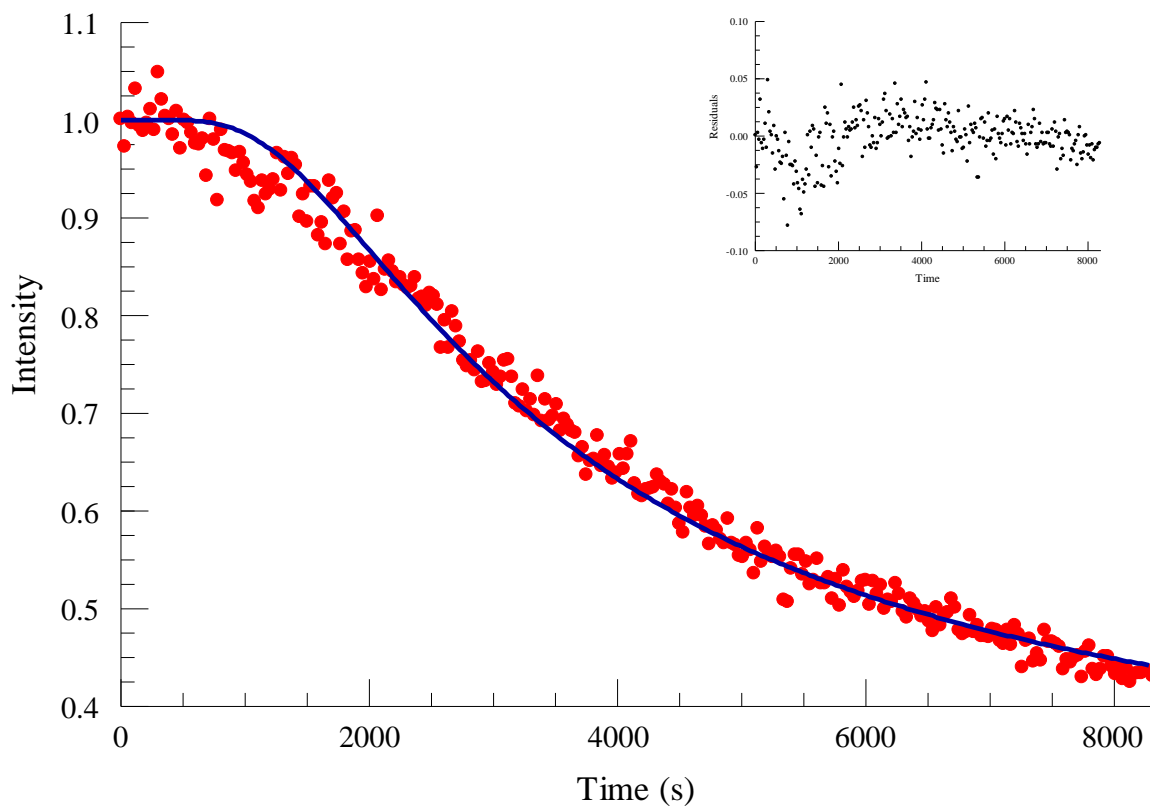


Figure 11: $Ru(dpp)_3Cl_2/[Emim][Tf_2N]$ sample- luminescence intensity versus time profile following a step change in oxygen concentration and fit to the diffusion model. Dots are the experimental data and solid line is the best fit to the diffusion model. Included in the top right corner of the figure are the residuals of the fit.

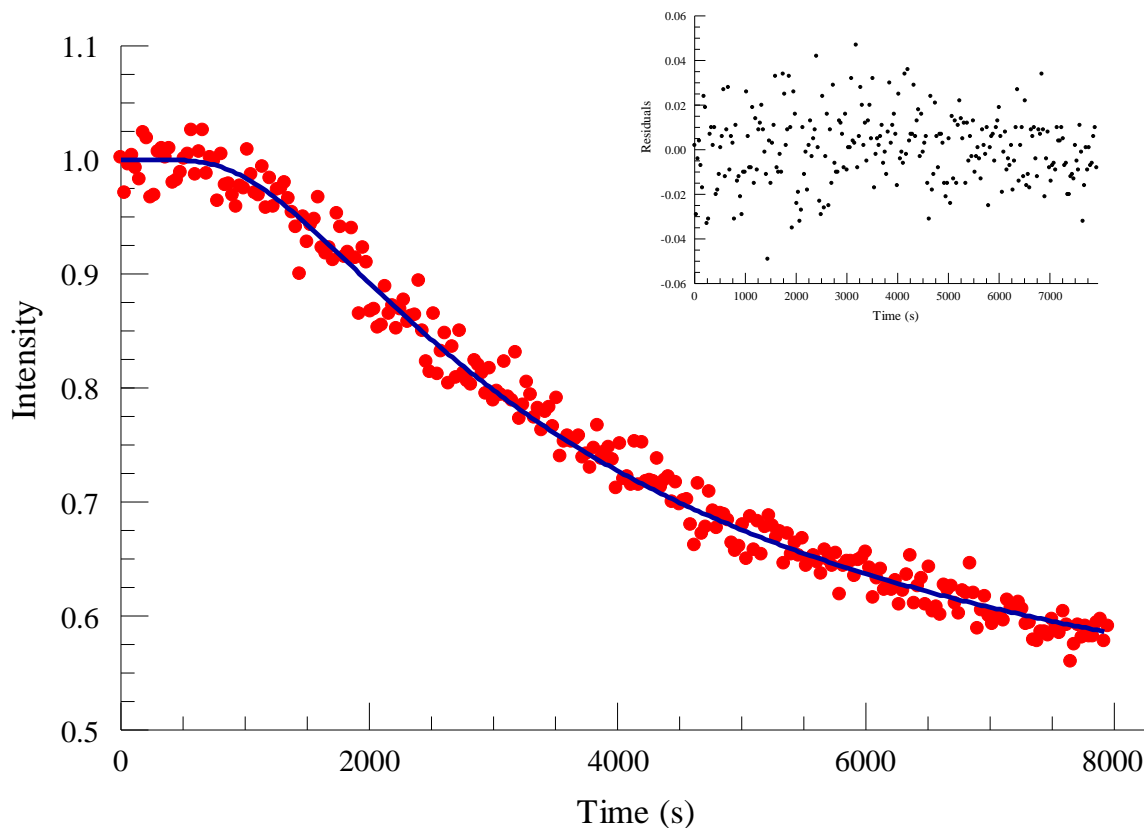


Figure 12: $Ru(dpp)_3Cl_2/[P14666]/[Tf_2N]$ sample- luminescence intensity versus time profile following a step change in oxygen concentration and fit to the diffusion model. Dots are the experimental data and solid line is the best fit to the diffusion model. Included in the top right corner of the figure are the residuals of the fit.

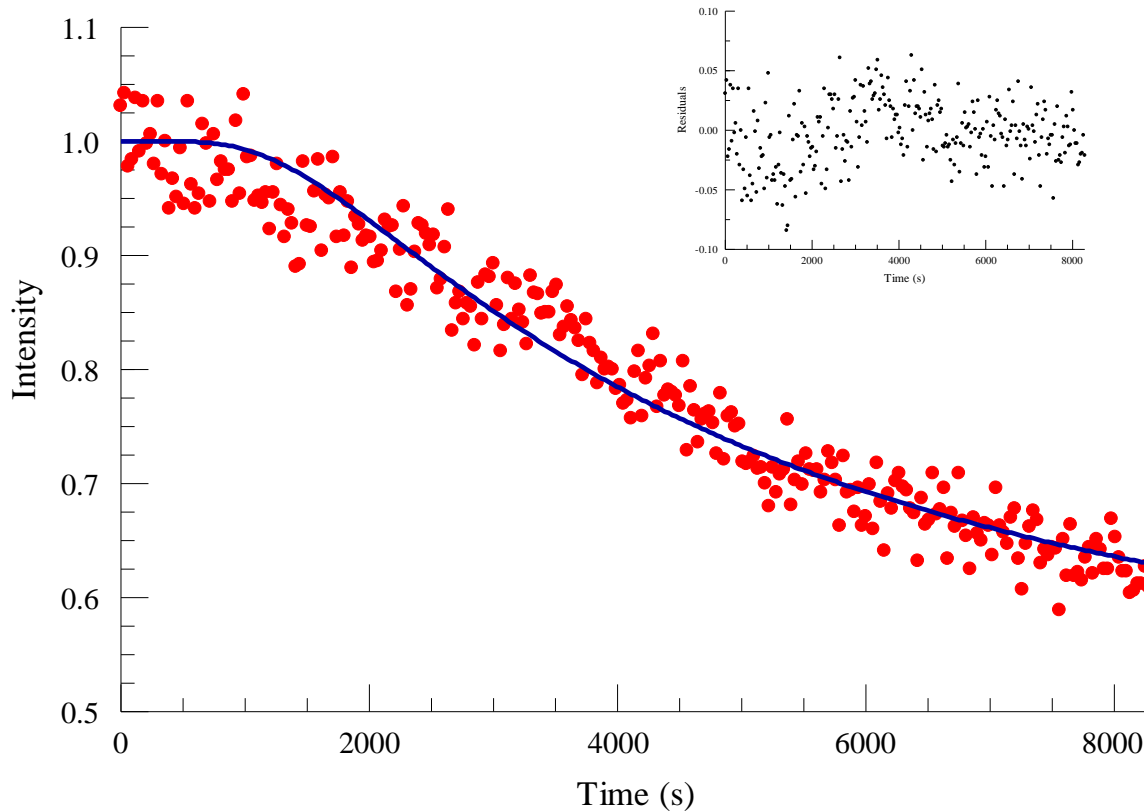


Figure 13: $Ru(dpp)_3Cl_2/[C4mpy][Tf_2N]$ sample- luminescence intensity versus time profile following a step change in oxygen concentration and fit to the diffusion model. Dots are the experimental data and solid line is the best fit to the diffusion model. Included in the top right corner of the figure are the residuals of the fit.

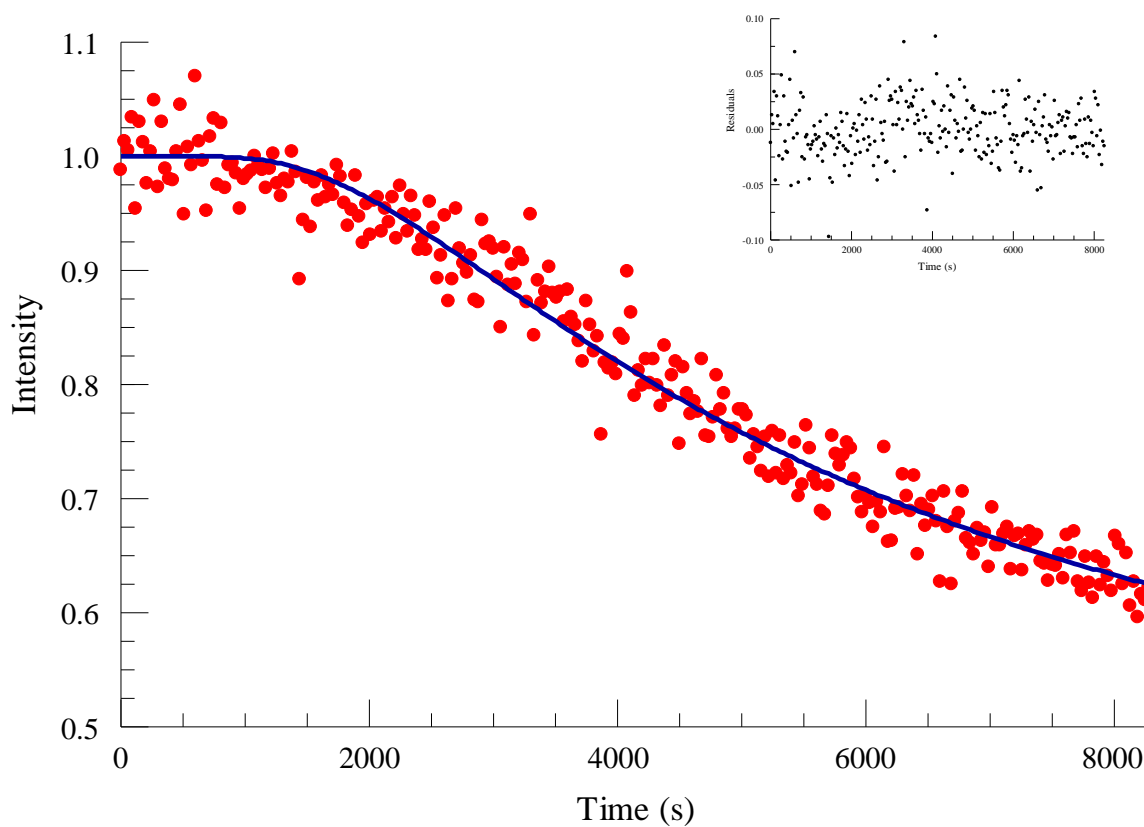


Figure 14: $Ru(dpp)_3Cl_2/[C4mpy][beti]$ sample- luminescence intensity versus time profile following a step change in oxygen concentration and fit to the diffusion model. Dots are the experimental data and solid line is the best fit to the diffusion model. Included in the top right corner of the figure are the residuals of the fit.

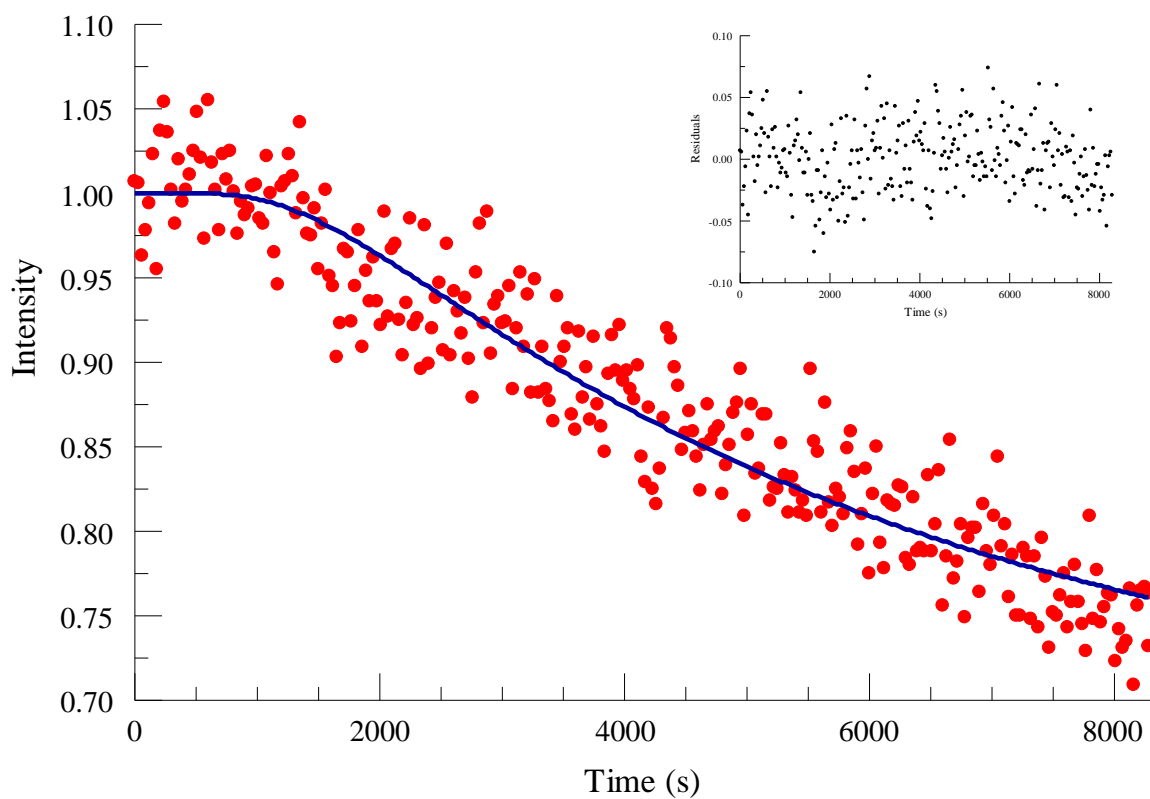


Figure 15: $Ru(dpp)_3Cl_2/[C3mmim][beti]$ sample- luminescence intensity versus time profile following a step change in oxygen concentration and fit to the diffusion model. Dots are the experimental data and solid line is the best fit to the diffusion model. Included in the top right corner of the figure are the residuals of the fit.

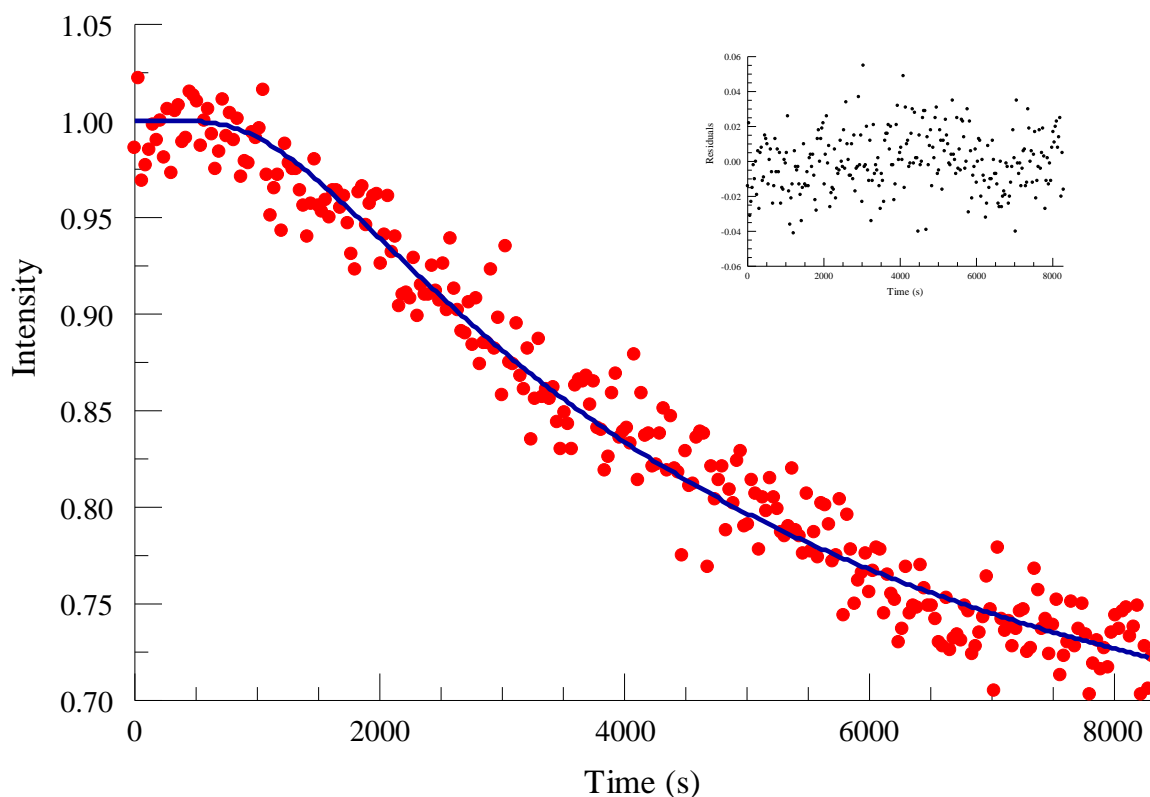


Figure 16: $Ru(dpp)_3Cl_2/[N4441][beti]$ sample- luminescence intensity versus time profile following a step change in oxygen concentration and fit to the diffusion model. Dots are the experimental data and solid line is the best fit to the diffusion model. Included in the top right corner of the figure are the residuals of the fit.

The measurements made in these diffusion experiment are based on the luminescence quenching of the Ru(II) complex. Ideally the experiment would be run until oxygen equilibrium conditions were reached within the

samples. At which time the final intensity would have reached a minimum plateau. This was not possible due to the time constraints of the experiment.

Since the oxygen concentration in the RTILs examined never reached equilibrium the proper oxygen quenching sensitivity for each sample to be used in the data analysis had to be determined systematically. For each sample the data was analyzed by substituting a range of values for I_{final} into equation 5. The range of I_{final} values was started with the final intensity value measured at the conclusion the experiment and ended with a value considerably lower than reasonably expected. Finally, a plot of equation 5, using the range of I_{final} values, versus the corresponding χ^2 was made for each sample. The value of equation 5 corresponding to the minimum of the plot was used in the data analysis. Figure 17 shows the plot of χ^2 used to determine the degree of quenching for the $\text{Ru}(\text{dpp})_3\text{Cl}_2/[\text{C6mpy}][\text{Tf}_2\text{N}]$ sample. All oxygen diffusion coefficients were determined by this procedure. Table 2 lists the determined diffusion coefficients for oxygen in our RTILs.

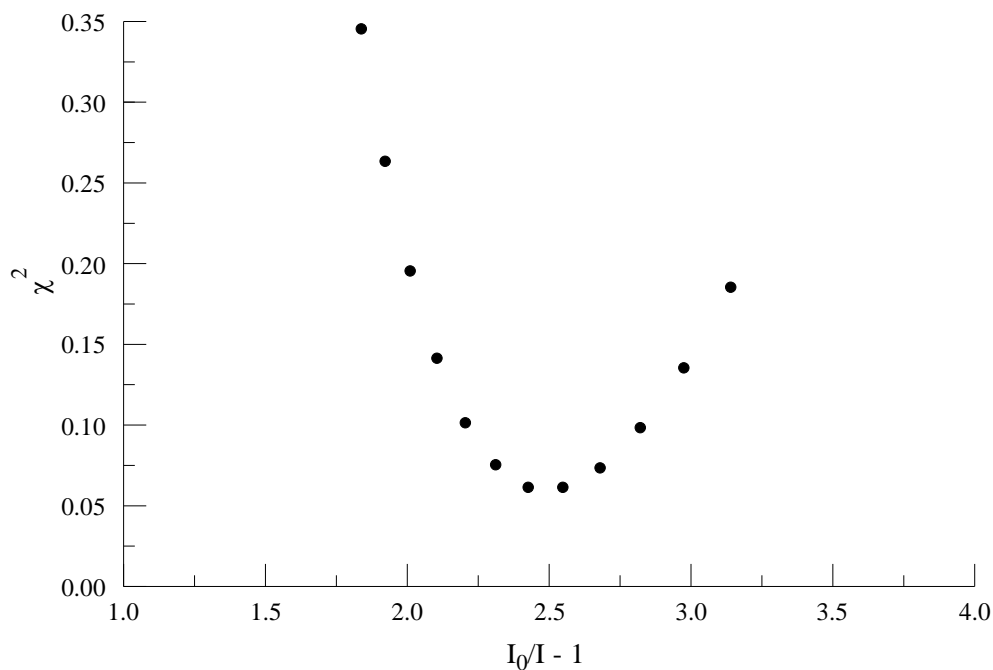


Figure 17: Plot of χ^2 versus oxygen quenching sensitivity for the $Ru(dpp)_3Cl_2/[C10mpy][Tf_2N]$ sample.

RTIL	D x10 ⁻⁶ (cm ² -sec ⁻¹)	χ^2
Emmim [Tf2N]	8.906	.106
C4mpy [Tf2N]	9.13	.207
C6mpy [Tf2N]	4.46	.078
C10mpy [Tf2N]	15.42	.061
P14666 [Tf2N]	10.76	.064
C3mmim [beti]	8.906	.2
N4441 [beti]	10.83	.076
C4mpy [beti]	6.55	.163

Conclusions

While the setup for measuring diffusion coefficients in RTILs was changed slightly from the oxygen diffusion in water measurements, the

premise of the technique remained the same. Before discussing how the measured D values for oxygen in the RTILs studied relate to the anomalously high quenching discussed in Chapter 6, verification of the results of these measurements will be presented in Chapter 8. Due to the time required to perform each experiment, measurements were not repeated.

To the best of our knowledge, this is the first report utilizing confocal fluorescence microscopy as a tool for measuring diffusion coefficients. To verify our results and show the validity of our newly developed method, oxygen diffusion coefficients in each RTIL were measured using a well-established electrochemical method.

Reference – Chapter 7

1. V. Didenko. “DNA Probes Using Fluorescence Resonance Energy Transfer (FRET): Designs and Applications.” *Biotechniques*. , 2001
2. *Fluorescence Microscopy, Volume II*; F. Rost, Cambridge University Press, 1995
3. J, Greivenkamp. *Field Guide to Geometrical Optics*. SPIE Field Guides vol. FG01. **2004**, 29
4. A, Arecchi; T, Messadi; J, Koshel. *Field Guide to Illumination*. SPIE. **2007**, 48
5. W, Boyle; G, Smith. *Charge Coupled Semiconductor Devices*. *Bell Sys. Tech. J.* 49. **1970**, 4, 587–593
6. J, Pawley. *Handbook of Biological Confocal Microscopy* 3rd ed. Berlin: Springer. **2006**
7. *Confocal scanning optical microscopy and three-dimensional imaging*; M. Laurent, G. Johannin, H. Guyader, and A. Fleury. *Biol Cell*, 1992
8. *Confocal Microscopy a Tool for the Investigation of the Anterior Part of the Eye*; P. Furrer, J. Mayer, and R. Gurny. *Journal of Ocular Pharmacology and Therapeutics*, Volume 13, Number 6, 1997

9. Confocal scanning microscopy: three-dimensional biological imaging;
D. Shotton and N. White. TIBS, November 1989
10. Ferrell, R; Himmelblau, D. *Diffusion coefficients of nitrogen and oxygen in water*, *J. Chem. Eng. Data*, **1967**, 12 (1), pp 111–115
11. Synthesis rudpp3- lifetime temp paper (23)
12. Kneas, Kristi A.; Demas, J.N.; Nguyen, Bryant; Lockhart, Aaron; Xu, Wenying; DeGraff, B. A. *Method for Measuring Oxygen Diffusion Coefficients of Polymer Films by Luminescence Quenching*. *Anal. Chem.* **2002**, 74, 1111-1118

Chapter 8: Oxygen Diffusion in RTILs: Electrochemical Method

Introduction

Oxygen diffusion coefficients in all RTILs utilized in this study have been determined. There is not an abundance of information regarding oxygen diffusion coefficients in RTILs for comparison with our results. An extensive literature search yielded only two sources in which oxygen diffusion coefficients were reported for the same RTILs used in this investigation. The diffusion of oxygen through these unique solvents is critical to the understanding of the anomalous quenching exhibited by the luminescence oxygen sensors. Therefore we must ensure the results of our oxygen diffusion measurements are credible before drawing any conclusions regarding the oxygen quenching in the systems.

Also necessary for complete analysis of the oxygen quenching behavior is the oxygen solubility. Obtaining the oxygen solubility for each RTIL will enable us to determine true bimolecular quenching rate constants for each Ru(II)/RTIL system.

The electrochemistry of chemical species has been utilized to measure their diffusion coefficients for decades. To validate the oxygen diffusion coefficients measured using the Fluorescence Confocal Microscopy experiments and to obtain another essential analytical parameter, oxygen

solubility, an electroanalytical technique known as chronoamperometry was performed on all of the RTILs used in the previous method.

Electrochemistry Background

In general, electrochemistry involves electrochemical reactions in which either an external applied drives a reaction, or a chemical reaction produces a voltage. Batteries are examples of the later, where chemical reactions produce a voltage. The other type of electrochemical reaction is caused when an applied voltage creates a driving force for the chemical reaction to occur.

A simple battery is made up of two half cells that are spatially separated but electrically connected.¹ Each half cell consists of an electrode and its supporting electrolyte. Typically, the electrode is a metal and the electrolyte is an aqueous salt of the metal. The electrodes are partially submerged in their respective electrolytes. The electrodes and electrolytes are chosen such that reduction takes place at the surface of one electrode, while oxidation takes place at the surface of the other electrode. The reducing electrode is called the cathode while oxidation occurs at the anode. The two electrode/electrolyte systems are connected by a salt bridge, which allows charge to flow through it but no mass transfer. The chemical energy, produced by the reactions between the electrodes and the electrolytes, is

converted to electrical energy that can be tapped from the external electrodes.¹⁻²

The second type is the basis for the electrochemical technique, chronoamperometry, used in this study. A chronoamperometric measurement initially starts by applying a potential at which no electrochemical reactions proceeds. The value of the applied potential is the voltage of the working electrode relative to the reference electrode. The applied potential is held constant for a selected period of time to establish a baseline and then is rapidly switched to a potential at which electrolysis occurs. The ensuing electrochemical reaction takes place at the surface of the working electrode. The applied potential may be held at this new value for the remainder of the experiment, or it may be stepped back to the original starting potential. In the case of reversible systems, if the potential is stepped back to the original value, the product formed after the first potential step will undergo a chemical reaction back to its original state. When the resulting current is analyzed as a function of time, various system parameters such as concentration of the diffusing species, diffusion coefficient, and number of electrons transferred during the reaction may be determined.³⁻⁴

Chronoamperometric measurements are performed using either two or three electrodes. The electrodes can be of various geometries and materials. Carbon, gold (Au), platinum (Pt), and mercury (Hg) are among the more commonly used working electrode materials. While the geometry of the working electrode does indeed affect the diffusion of the electroanalytic species in the system, the working electrode material does not. Material does however affect background current. Also, trace amounts of water or acid in systems with gold or platinum working electrodes could lead to the production of hydrogen gas by the reduction of hydrogen ions in the system.⁵ While this, and the cost of both gold and platinum may be disadvantageous, gold and platinum wires are rigid, can be readily obtained in a wide range of sizes and high purity, and has good electrochemical inertness.

In both a two and three electrode setup, the value of the applied voltage relative to the reference electrode is the potential which causes the desired reaction to proceed. A three electrode setup consists of a working electrode, an auxiliary electrode, and a reference electrode. The working electrode, reference electrode, and electrolytic solution create a closed path for current flow through the electrochemical cell. The movement of charged particles at and near the surface of the electrodes will cause variances in the

surface potentials. The potential at the auxiliary electrode is adjusted to maintain a constant potential at the surface the working electrode relative to the reference electrode. In a two electrode system, the reference electrode completes the current path between the working electrode and electrolyte, as well as providing the reference point for controlling a constant potential at the surface of the working electrode.

Fundamentally, chronoamperometry is a measurement of a diffusing electroactive species that occurs from the creation of a heterogeneous region in the electrolyte following a step change in potential. Consider a two electrode system consisting of a platinum planar electrode with a corresponding reference electrode. The electrodes are immersed in a homogeneous solution containing an electroactive species with a known reduction-oxidation (redox) potential. Since the electrochemical reaction of interest occurs at the surface of the working electrode, let's examine what happens in the vicinity of the surface of the electrode. For a system involving reduction the applied potential is initially above where no electrolysis occurs. When the potential is stepped below the reduction potential, the following reaction occurs



where O is the electroactive species, n is the number of electrons transferred in the reaction, and R is the reduced form of the electroactive species. Prior to the potential step, there was no R in the system at all, only O. All of the electroactive species in the direct vicinity of the surface of the working electrode are instantaneously reduced, as given by equation 1, immediately following the potential step. The region near the surface of the working electrode, with a quantity of R and void of O, creates a concentration gradient between the region near the surface of the electrode and the bulk solution in the process. Figure 1 gives a simplistic illustration of the depletion region of O and formation of R. The concentration gradients produced provides the driving force for the diffusion of both O from the bulk solution to the surface of the electrode, and R from the region near the electrode's surface to the bulk solution. The one dimensional diffusion of the electroactive species from regions of high concentration to low concentration can be described by Fick's First Law as follows

$$J = -D \frac{\partial}{\partial x} [O, R] \quad (2)$$

where J is the diffusion flux which is a measure of the number of species flowing through an area per unit time, and D is the diffusion coefficient.

Faraday's Law, named after the English physicist Michael Faraday, states that the mass of a given substance that is produced or consumed at an

electrode is proportional to the quantity of electric charged passed through the cell.⁵ The value of Faraday's constant (F)

$$F = eN_A \approx 96,485.31 \text{ C/mole} \quad (3)$$

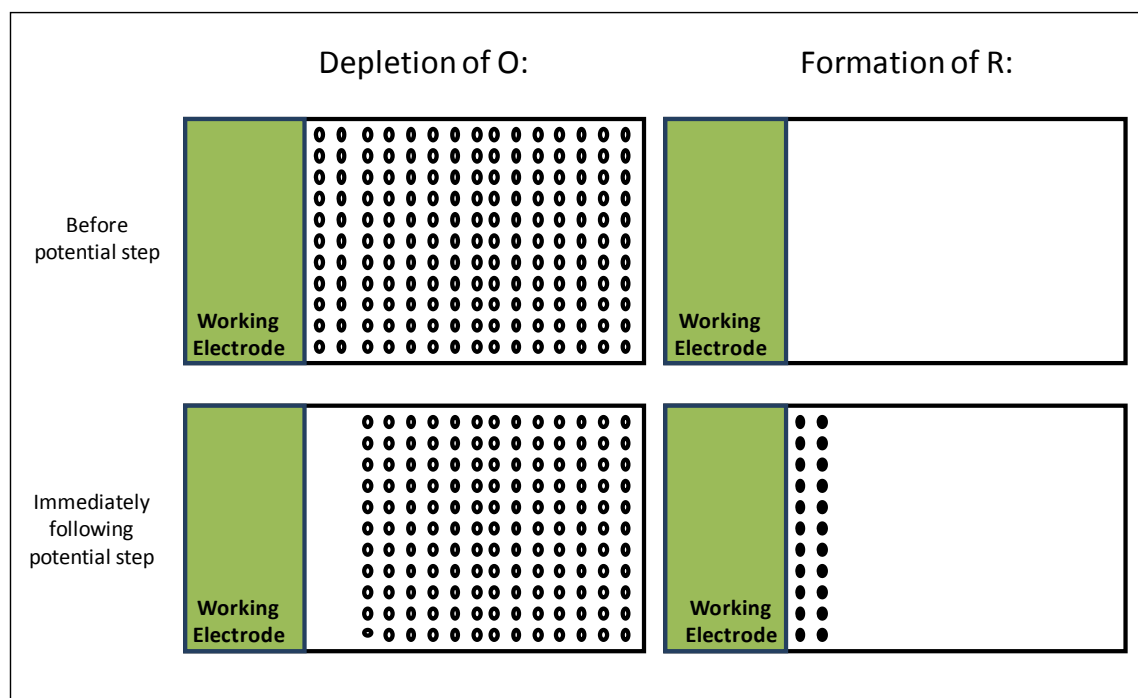


Figure 1: Illustration of the depletion of O and the formation of R.

where e is the charge on an electron, N_A is Avogadro's number, and C is a coulomb. So, the total passing through the surface of an electrode would be given by

$$Q = nFN \quad (4)$$

where N is the total number of moles of the species reacted. It follows that the current (i) produced at the electrode surface can be related to the amount of electroactive species produced or consumed by

$$i_t = \frac{dQ}{dt} = nF \frac{dN}{dt} \quad (5)$$

Rewriting J in terms of area (A) and combining equation 2 with equation 5 gives the current at the surface of a working electrode of area A as

$$i_t = -nFAD \frac{\partial}{\partial x} [O, R]_{x=0,t} \quad (6)$$

In 1903, American physical chemist Frederick Cottrell, using Fick's Second Law and the appropriate boundary conditions, derived the following expression for the current at an infinite planar electrode from a redox reaction following a step change in potential

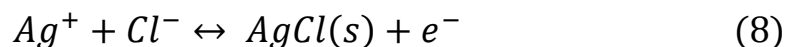
$$i_t = \frac{nFAc_{O,R}D_{O,R}^{1/2}}{\pi^{1/2}t^{1/2}} \quad (7)$$

where $c_{O,R}$ is the concentration of the oxidized or reduced species respectively and $D_{O,R}$ is the diffusion coefficient of the oxidized or reduced species respectively.^{3,6} Equation 7, known as the Cottrell equation, has been derived for many other geometries of electrodes as well.

Materials: A supporting electrolyte of 1M potassium chloride (KCl) was prepared by dissolving the appropriate amount of potassium chloride (Fisher) in deionized water. The 1M KCl solution was then used to make

the 5mM (or 5.29 mM) ferricyanide sample by dissolving the appropriate amount of potassium ferricyanide (Fisher) in the 1M supporting electrolyte. The RTILs used in this experiment were as follows: [N4,4,4,1][beti], [P14,6,6,6][Tf₂N], [C4mpy][Tf₂N], [C6mpy][Tf₂N], [C10mpy][Tf₂N], [Emmim][Tf₂N], [C3mimm][beti], and [C4mpy][beti]. All RTILs were courtesy of Dr. Gary Baker, Oak Ridge National Laboratory.

Instrumentation: Measurements were made using a two electrode setup consisting of either a 10 μm diameter or 25.6 μm Pt micro-disk working electrode (CH Instruments) and a silver/silver chloride (Ag/AgCl) reference electrode. The Ag/AgCl reference electrode was made by placing one end of a 5mm diameter silver wire in 1M hydrochloric acid (HCl) with the other end connected to the positive terminal of a potentiostat. A separate 28 gauge silver-plated copper wire lead was placed in the 1M HCl and connected to the negative terminal of the potentiostat. A positive 1.5 V, relative to the silver wire, was applied to the two wires for approximately 20 seconds. With the given applied potential, the following reaction proceeds at the surface of the silver wire



Thus, a thin AgCl salt layer is formed on the surface of the silver wire.

All chronoamperometric measurements were carried out in the laboratory of Dr. Jill Venton (Chemistry department, University of Virginia) using a ChemClamp (Dagan, Minneapolis, MN, $n = 0.01$ headstage), PCI 6711 and 6052 computer interface cards (National Instruments, Austin, TX) and home built break-out box. Tarheel software was used for the data collection. Current versus time data sets were saved as ASCII files and analyzed using PSI Plot (Poly Software International) software.

Working Electrode Electrochemical Radius

Determination

Chronoamperometry is routinely used to determine the diffusion coefficient and the concentration of an electroactive species using an electrode geometry appropriate version of the Cottrell equation. In order to obtain these quantities, the electrode properties must be known. One such electrode property that is essential for the chronoamperometric evaluation of an electroactive species is the electrochemical area of the working electrode. In order to determine the electrochemical area of the working electrode, it is common practice to first performed chronoamperometric measurements on a well-studied electroactive species with a known diffusion coefficient.

If the diffusion coefficient of the electroactive species is known, the electrochemical area, and thus the radius, of the working electrode can be calculated from equation 7 or its derivatives. While the physical radius of the electrode can be measured mechanically, it is the electrochemical radius that is of importance in electrochemical experiments. Since the surface of the working electrode is where the chemical reaction of interest takes place, adsorption, oxidation, or any defects at the surface of the electrode would alter the electrochemical area of the electrode and as a result, the measured current. Ferricyanide ($\text{Fe}(\text{CN})_6^{3-}$), which has a diffusion coefficient of $7.6 \times 10^{-6} \text{ cm}^2/\text{s}$ in 1M KCl at 25 °C, was the standard used for the determination of the electrochemical radius of the working electrode.⁷

Polishing: Prior to the start of the experiment, the working electrode was polished. Several drops of deionized water were used to wet the polishing cloth. After sufficiently wetting the cloth, a few milligrams of 0.05 micron alumina (CH Instruments) were placed on the polishing cloth. While holding the electrode perpendicular to the polishing pad, the electrode was moved in a small circular motion for approximately 3-4 minutes. The electrode was then thoroughly rinsed with deionized water and allowed to air dry. The electrode was polished in this fashion every few experiments.

Measurements: Data was collected at a sampling frequency of 1,000 Hz. All potential values applied to the working electrode were calculated relative to the reference electrode. The initial voltage was 0.000 V. Current versus time data were acquired by applying a pre-step voltage of 600 mV to the working electrode for 20 seconds, stepping the potential to 0 V for 20 seconds, and then stepping the potential back to 600 mV for 20 seconds.

Figure 2 represents the potential applied to the working electrode.

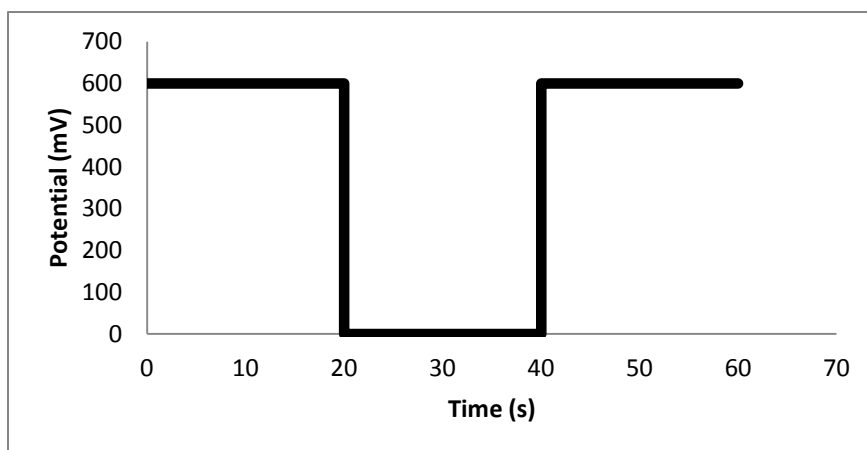


Figure 2: Illustration of the square-wave potential applied to the working electrode.

Results and Discussion

The reversible chemical reaction of ferricyanide to ferrocyanide ($\text{Fe}(\text{CN})_6^{4-}$) has been extensively investigated. Ferricyanide can be reduced to ferrocyanide according to the following reaction



When the potential illustrated in Figure 2 is applied the working electrode of the electrochemical cell, from $t=0$ seconds until $t=20$ seconds, there is zero resulting current since the applied potential is above the potential at which electrolysis occurs for the ferricyanide system. At $t=20$ seconds, when the potential is rapidly switched from 600 mV to 0 V, all of the $\text{Fe}(\text{CN})_6^{3-}$ near the Pt electrode surface is instantaneously reduced. This causes a large spike in the magnitude of the recorded current. As the species that was instantaneously reduced, $\text{Fe}(\text{CN})_6^{4-}$, diffuses away from the surface of the working electrode, current decreases as further reduction is limited by the diffusion of the electroactive $\text{Fe}(\text{CN})_6^{3-}$ from the bulk solution to the surface of the electrode. The current falls off as $t^{-1/2}$ as given by the Cottrell equation and then plateaus. At $t=40$ seconds, the potential is stepped back to 600 mV, causing all of the $\text{Fe}(\text{CN})_6^{4-}$ near the surface of the working electrode to be instantaneously oxidized back to $\text{Fe}(\text{CN})_6^{3-}$. The result is a large current in

the reverse direction. Current falls off as further oxidation is limited by the diffusion of $\text{Fe}(\text{CN})_6^{4-}$ back to the surface of the electrode. Unlike the reduction current, the reverse current quickly reaches zero as essentially all of the $\text{Fe}(\text{CN})_6^{4-}$ that was produced is oxidized back to $\text{Fe}(\text{CN})_6^{3-}$. Figure 3 shows the resulting current as a function of time for the ferricyanide/ferrocyanide system following the potential illustrated in Figure 2. As seen in Figure 3, the current in each of the three distinct regions of the figure follows as predicted for the applied potential profile shown in Figure 2.

The first potential step is the start of the electrochemical reaction of interest and therefore taken to be $t = 0$. While Figure 1 provided an illustration of the driving force for the current to which is to be analyzed, it was an over simplified depiction of the current response. An additional “charging” current is also present at short times.

The charging current is the result of the double layer capacitance at the surface of the electrode-electrolyte interfaces. Negative ions near the surface of an electrode held at a positive potential will be attracted to the electrode, forming a layer of negative ions. The charge on the redistributed negative ions is opposite the positive charge of the electrode, thus creating the required condition of neutrality at the electrolyte-electrode interface

under equilibrium conditions. The ion layer-electrode interface is equivalent to parallel plate capacitors separated by a small distance (the ion layer radius). Thus there is always an inherent capacitive charging current associated with any electrode-electrolyte system when the electrode potential is switched. Currents associated with instrumentation electronics is an important but separate issue.

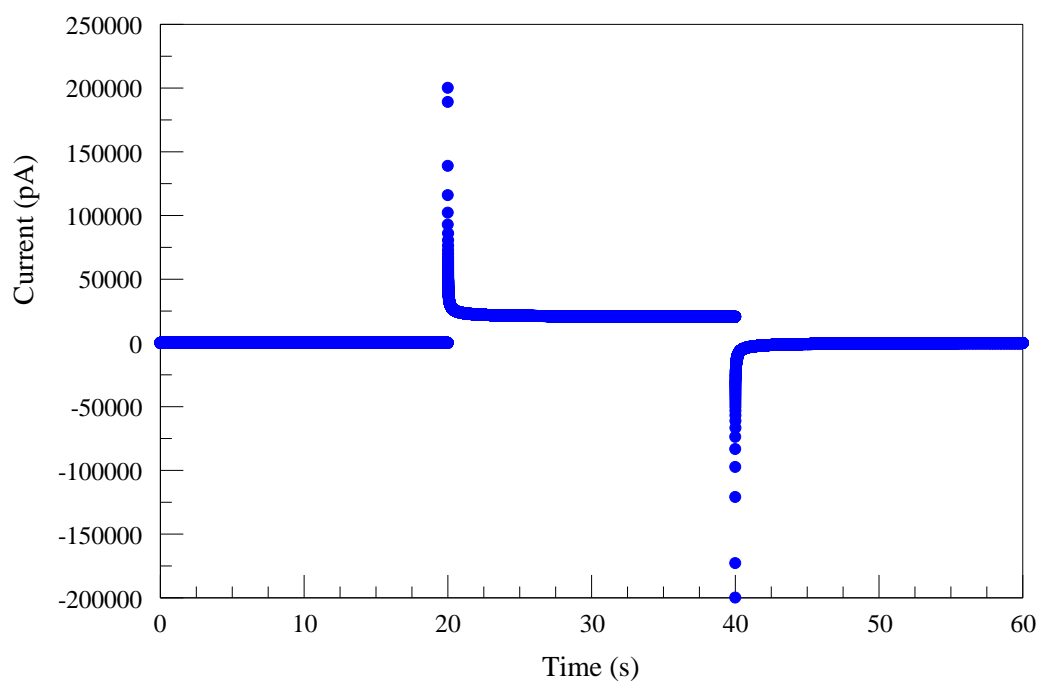


Figure 3: Current profile of the ferricyanide/ferrocyanide system as measured at the surface of the working electrode following the application of the potential in Figure 2.

An expanded current versus time data set of 1 M KCl supporting electrolyte only and 5 mM ferricyanide in 1 M KCl are shown in Figure 4, with start time, $t = 0$, taken to be the time of the first potential step. The exponential decrease of the capacitive charging current causes its value to rapidly fall off. Subsequently, it is common practice when analyzing chronoamperometric measurements to begin data analysis several microseconds after the potential step.

To minimize the adverse effect of background currents, measurements made in 1 M KCl supporting electrolyte only were performed then subtracted from the 5 mM ferricyanide data set. This improved the quality of the empirical fits during radius determination data analysis slightly, but more importantly provided an operating method that could be utilized during future RTIL measurements.

As discussed earlier, RTILs can have considerable amounts of impurities. The combination of a high impurity concentration in a RTIL and the adverse instrumentation currents could produce unknown electrochemistry that would ultimately influence our data analysis and results.

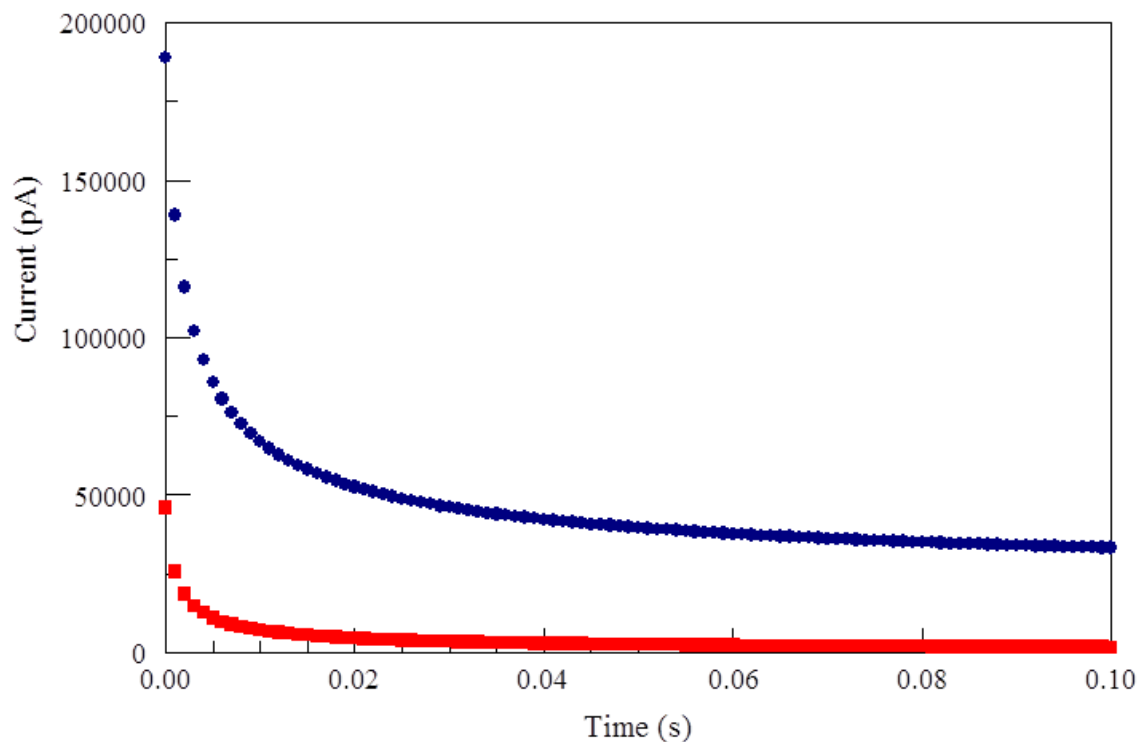


Figure 4: Current profile of the 1 M KCl supporting electrolyte only and 5 mM ferricyanide in 1 M KCl following a step change in potential. Circles are the 5 mM ferricyanide data points while the squares are the 1 M KCl data points.

For all chronoamperometric measurements the initial current response is always some form of the Cottrell equation similar to that given in equation 6. The geometry of the working electrode will cause proportionality constants and offsets to vary from electrode to electrode. For certain

electrode geometries, the solution to Fick's Law and thus the current response of a chronoamperometric measurement will not go to zero at infinity as predicted by the general form of the Cottrell equation but will instead reach a steady state value.

Unlike the case of planar electrodes that was used to explain the theory behind chronoamperometry earlier in this section, disc shape electrodes are one of a few geometries in which the current at the working electrode reaches a steady state value after some finite period of time. The initial current response still follows the Cottrell equation but a steady state condition will be obtained if the experiment proceeds long enough.⁸⁻¹³ The ability of an electrode to obtain steady state is independent of the size of the electrode. However, the size of the electrode will determine how long it will take for the current to reach steady state.¹¹ Larger electrodes will require longer times to achieve steady state.

In the process of deriving the Cottrell equation we showed, in equation 6, that the current response at the surface of the working electrode was dependent on the change in concentration of the electroactive species. For the geometries of electrodes that are able to obtain steady state conditions, the rate at which the electroactive species is depleted near the surface of the electrode must equal the rate of replenishment. This balance

creates an unchanging concentration of the electroactive species in the region near the surface of the electrode.

The experimentally observed transient and steady state current at the surface of a micro-disk electrode, resulting from the reduction or oxidation of an electrolytic species following a step change in potential is described by the following expression, derived by Bard et al¹¹

$$I_t = \pi^{1/2} n F D_{O,R}^{1/2} c_{O,R} r^2 t^{-1/2} + 4 n F D_{O,R} c_{O,R} r \quad (10)$$

where I_t is the current at the surface of the working electrode. Equation 10 describes the current response for two distinct regions, short times and long times, of a micro-disk chronoamperometric curve. Shoup and Szabo obtained an empirical fit to equation 10 that described the chronoamperometric current for all times.¹³ The following Shoup and Szabo expression which we used for fitting is accurate to 0.06% for all times

$$I = -4 n F D c r f(\tau) \quad (11)$$

where

$$f(\tau) = 0.7854 + .8863 \tau^{-1/2} + 0.2146 e^{-0.7823/\sqrt{\tau}} \quad (12)$$

and

$$\tau = \frac{4Dt}{r^2} \quad (13)$$

Figure 5 shows the chronoamperometric data for 5 mM $\text{Fe}(\text{CN})_6^{3-}$ background subtracted current as a function of time and the fit to equation 11 used for the electrochemical radius determination of the 10 μm diameter Pt micro-disk electrode. The radius was determined to be $5.1 \pm 0.003 \mu\text{m}$ using nonlinear least squares fitting in PSI Plot. The $t^{-1/2}$ dependence in the transient portion of equation 11 causes the function to blow up at $t = 0$. As a result, the first point in the data set was dropped. Data analysis was started at $t = 5 \text{ ms}$, to minimize effects of the charging current. Only the first one second of the collected data was used in the fit; one second was found to be sufficient time for the system to reach steady state. Similarly, using a 5.29 mM $\text{Fe}(\text{CN})_6^{3-}$ sample, the electrochemical radius of the 25 μm diameter Pt micro-disk electrode was found to be $13.0 \pm 0.01 \mu\text{m}$.

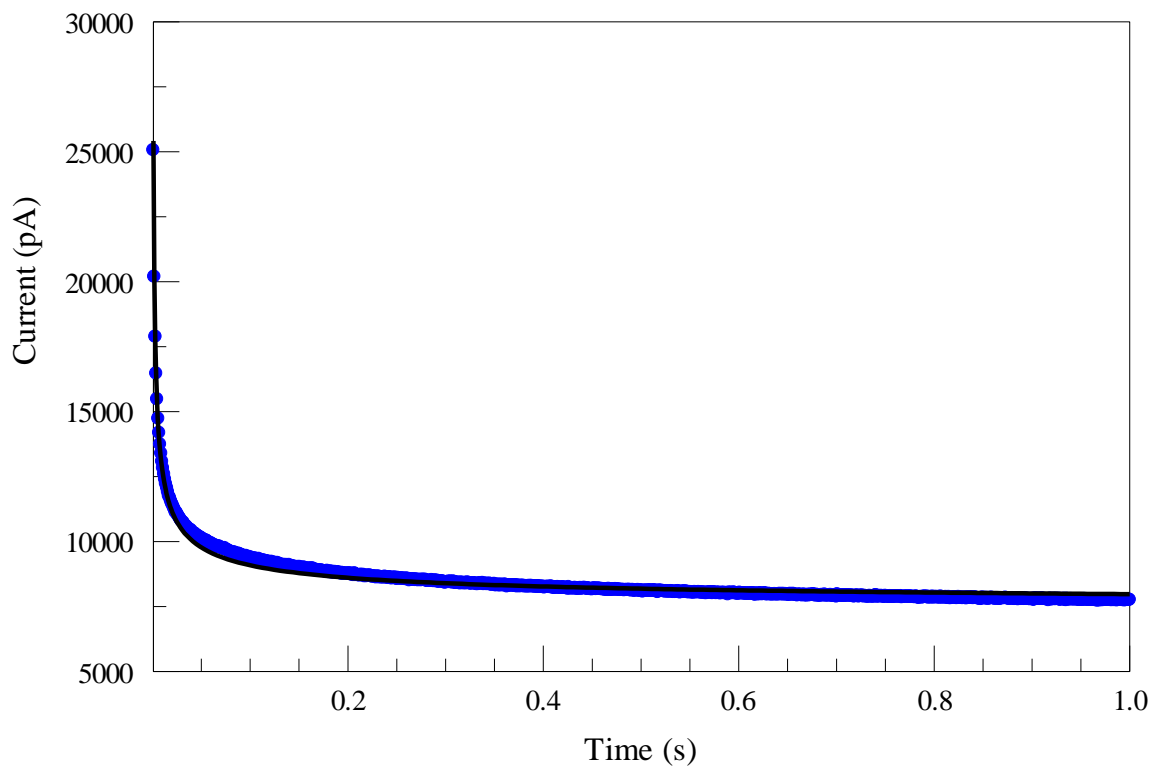


Figure 5: Background subtracted chronoamperometric data for 5 mM $Fe(CN)_6^{3-}$ and the fit to equation 11. Circles are the data points and the solid line is the fit.

Oxygen Diffusion in RTILs

Experimental Setup: Instrumentation and software was the same as described for the Working Electrode Electrochemical Radius Determination section above. Figure 6 shows the experimental setup used for the electroanalytical determination of the oxygen diffusion coefficients and

oxygen solubility of the listed RTILs. A two electrode setup, consisting of a 10 μm diameter Pt micro-disk working electrode and a silver/silver chloride reference electrode was used for each chronoamperometric measurement. The two electrodes were positioned side by side in close proximity to each other, but never touching one another. The bottom of a 2 mL Eppendorf tube was cut off and used as the sample holder into which the RTILs were pipetted.

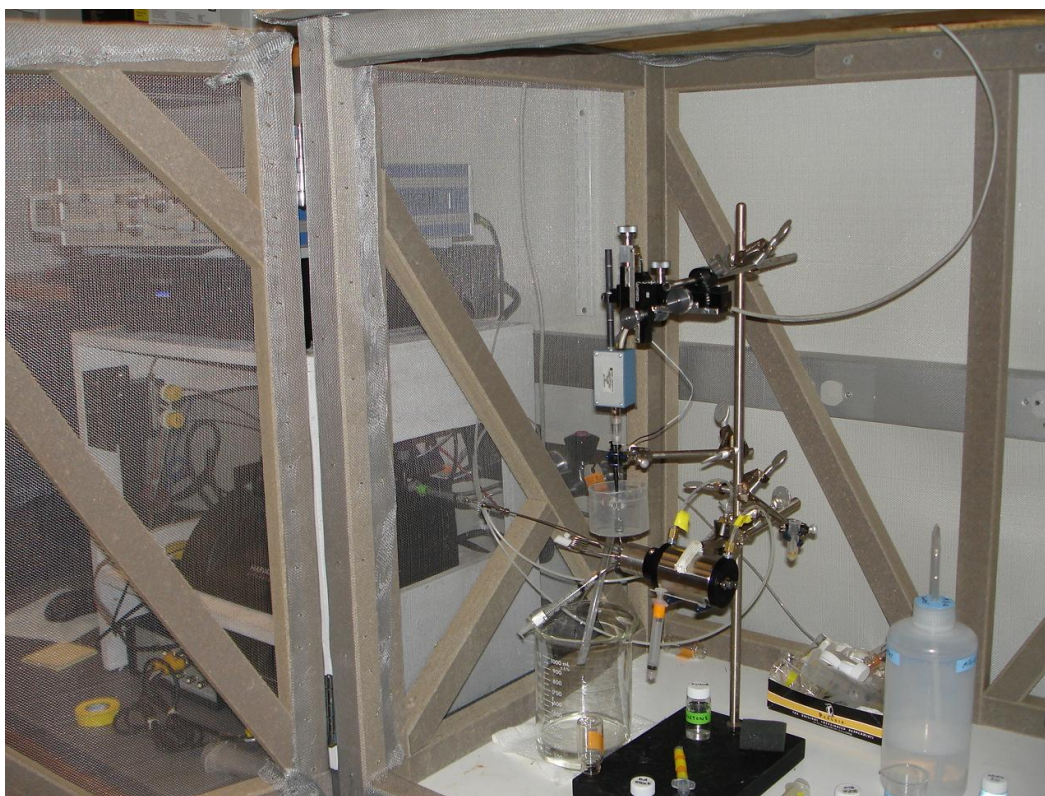


Figure 6: Picture of electrochemical instrumentation used for the determination of oxygen diffusion coefficients.

Purging: For each measurement, a few ml of each RTIL sample were first placed in a small glass vial. To remove any ambient oxygen present in the samples, the RTILs were initially purged with compressed argon for approximately 45 minutes. A magnetic stir bar and stir plate were used to ensure good mixing. After the argon purge, a small amount of sample ($\sim 1/8$ ml) was pipetted into the sample holder. Chronoamperometric measurements were immediately made on the oxygen-free samples.

After each measurement, the volume of sample that was used in the electrochemical measurement was separated from the remaining unused sample and both the working electrode and the reference electrode were wiped clean with lens paper. Lens paper was used to minimize the possibility of stray cloth fibers adhering to the surface of the electrodes. After stopping the argon purge in the unused sample, the sample was then purged with compressed oxygen for approximately 45 minutes. After purging with oxygen, a small amount of sample was pipetted into the sample holder and chronoamperometric measurements were immediately made on the oxygen-saturated samples.

Measurements: Chronoamperometric measurements of both the argon saturated and the oxygen saturated RTILs were performed at a sampling frequency of 1,000 Hz, with a total data collection time of 60

seconds. At the start of the measurement, a pre-step voltage of 0 V was applied to the working electrode for 20 seconds. After the 20 seconds, the potential was stepped below the oxygen reduction potential. To ensure complete oxygen reduction at the surface of the electrode, the magnitude of the applied potential was greater than the reduction potential but not too large as to cause additional, unwanted, electrochemistry. This is especially important in a two electrode setup since the electrochemistry at the surface of the working electrode changes the potential of the electrode.

It is common practice to determine the value of the applied potential to be used by first running cyclic voltammetry measurements of the desired electrolytic species. Since it would be extremely time consuming to run cyclic voltammetry (CV) measurements on all of our RTILs, CV experiments were not performed. It is, however, reasonable to assume that the reduction potential of O₂ would not vary greatly in the RTILs studied here. Literature values support this. Two of the RTILs in this work, P14,6,6,6-[Tf₂N] and Emim-[Tf₂N], have been investigated by electrochemical methods elsewhere.^{14,16} Cyclic voltammetry measurements in those studies showed the reductions potential to be approximately -0.8 V versus a silver reference electrode. The potential of a silver wire is +0.79 V versus a normal hydrogen electrode (N.H.E.) and the potential of Ag/AgCl

electrode is +0.222 V versus a N.H.E. Thus, after adjusting for the difference in reference electrode potentials, and slightly increasing the magnitude of the potential, a step potential of -1.5 V versus the Ag/AgCl reference electrode was determined to be a reasonable value.

Finally, after holding the potential at -1.5 V for 20 seconds, the potential was stepped back to 0 V for 20 seconds and the measurement was concluded. The resulting square wave potential applied to the working electrode was similar to that of Figure 3 but with the corresponding values discussed.

Results and Discussion

The electrochemistry of molecular oxygen in conventional aqueous solutions has been greatly studied.¹⁴⁻¹⁹ At the surface of an electrode, with proper applied voltage, molecular oxygen in conventional solvents, is known to undergo a reversible one electron reduction to a superoxide as follows



where O_2^- is reduced dioxygen.¹³⁻¹⁸ Cyclic voltammetric and chronoamperometric studies have revealed that the reduction of oxygen in certain RTILs follow equation 14 as well.¹³⁻¹⁶ The superoxide radical is extremely reactive; as a result, the reduction of oxygen in some RTILs has

also shown to be an irreversible process.¹⁴⁻¹⁶ Figure 7 is an illustration of the diffusion and reduction of oxygen at the surface of an electrode.

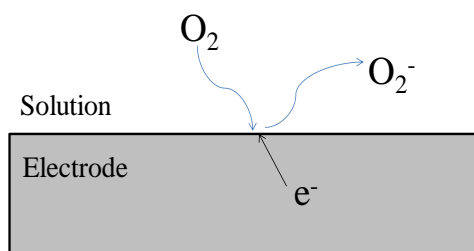
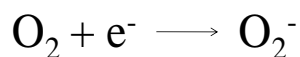


Figure 7: Illustration of oxygen diffusion and reduction at the surface of an electrode.

Unlike the chronoamperometric measurements made when determining the electrochemical radius of the working electrode, where the concentration of the electroactive species was known, the concentration of oxygen in the RTILs is unknown. Using nonlinear least square fitting in PSI Plot, equation 11 was used to determine the diffusion coefficients and the oxygen concentrations of the RTILs in this study.

The electrochemical radius calculated previously, along with initial guesses for the adjustable parameters D and c , were entered into equation 11. The PSI Plot software iterated through various values of D and c ,

minimizing the square of the difference between the experimental data and that calculated by equation 11 until the optimal values for D and c were determined. The experimental and calculated data for the diffusion of oxygen in the RTILs studied are shown in Figures 8 – 14.

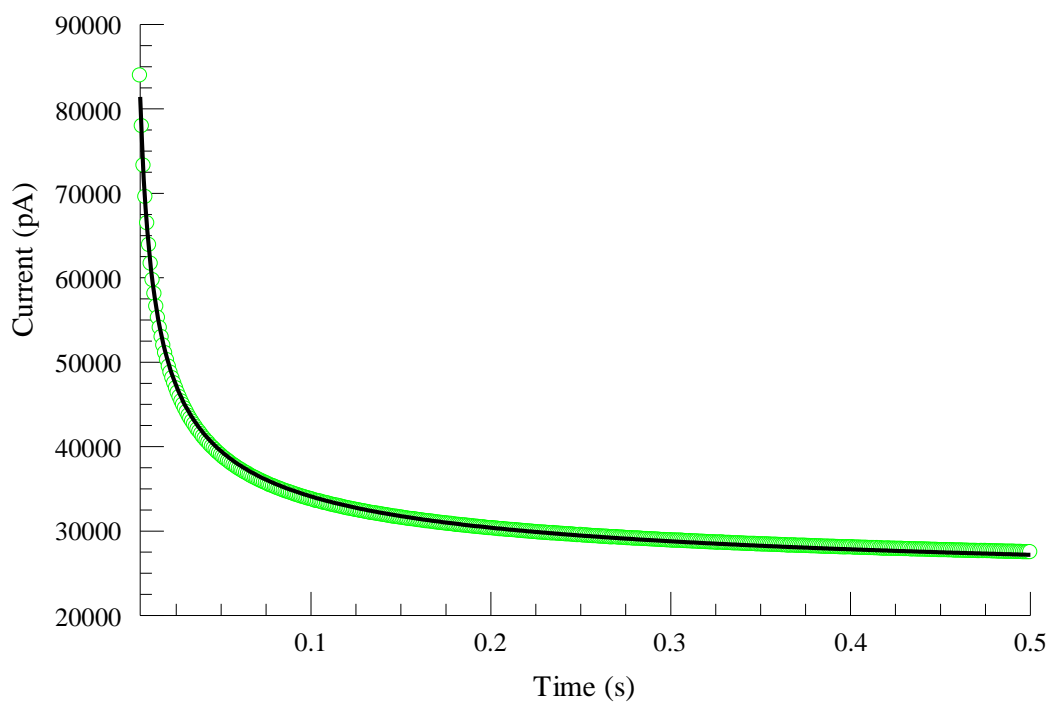


Figure 8: Experimental and calculated data for oxygen diffusion in [Emim][Tf₂N] RTIL. Open circles are the experimental data points while the solid line is the fit to equation 11.

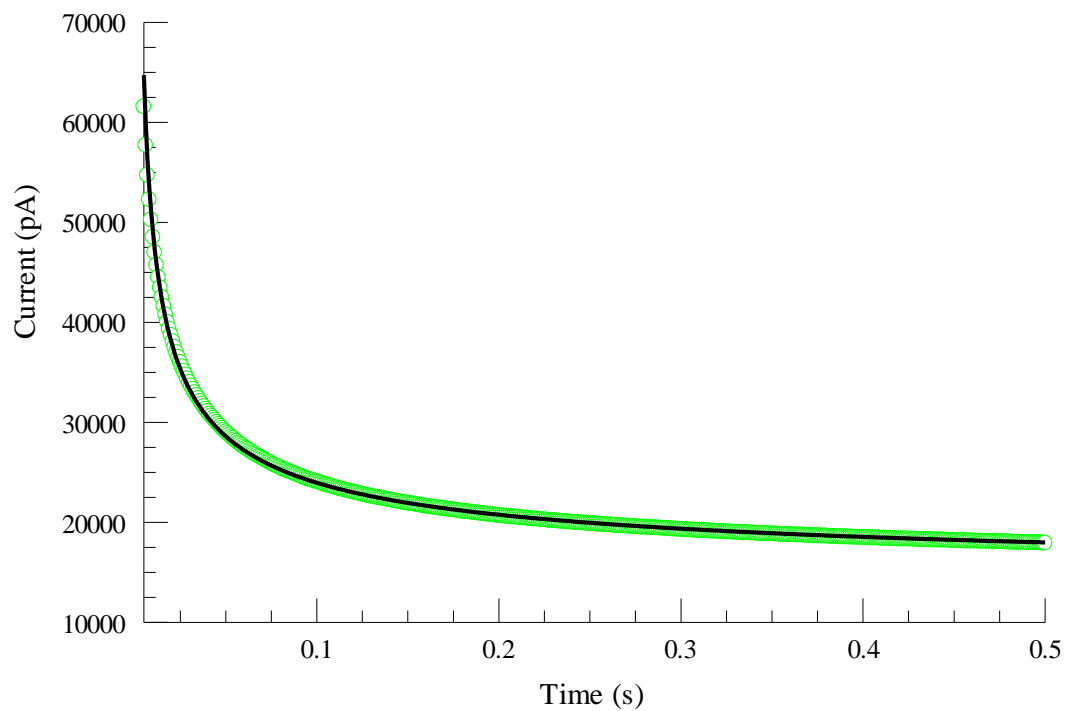


Figure 9: Experimental and calculated data for oxygen diffusion in [C10mpy][Tf2N] RTIL. Open circles are the experimental data points while the solid line is the fit to equation 11.

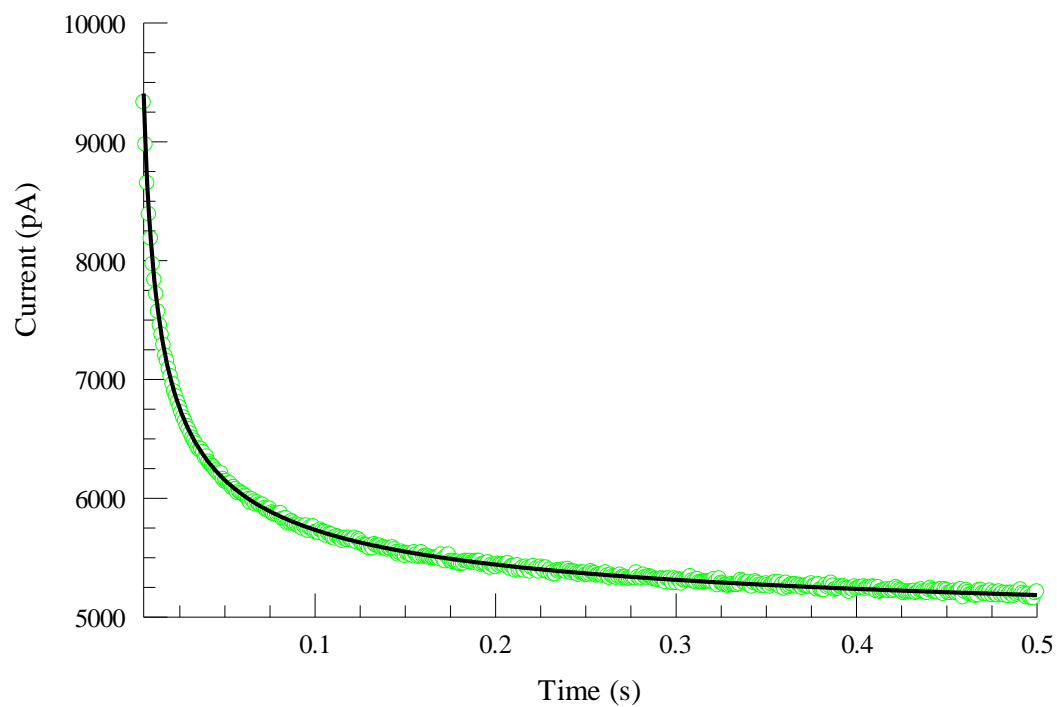


Figure 10: Experimental and calculated data for oxygen diffusion in [C4mpy][Tf2N] RTIL. Open circles are the experimental data points while the solid line is the fit to equation 11.

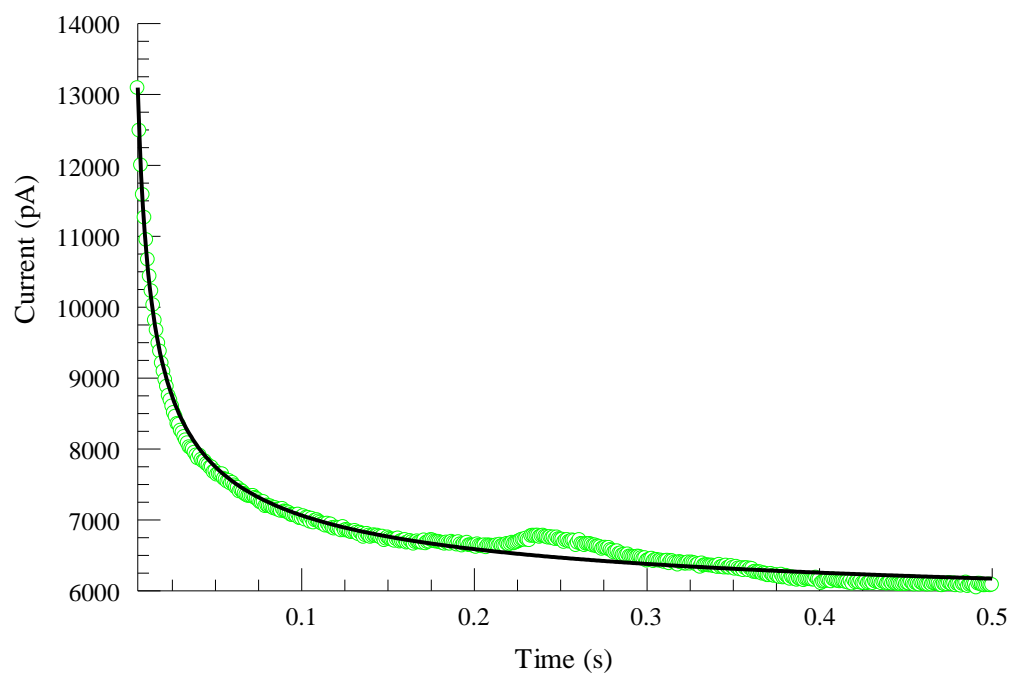


Figure 11: Experimental and calculated data for oxygen diffusion in [C6mpy][Tf2N] RTIL. Open circles are the experimental data points while the solid line is the fit to equation 11.

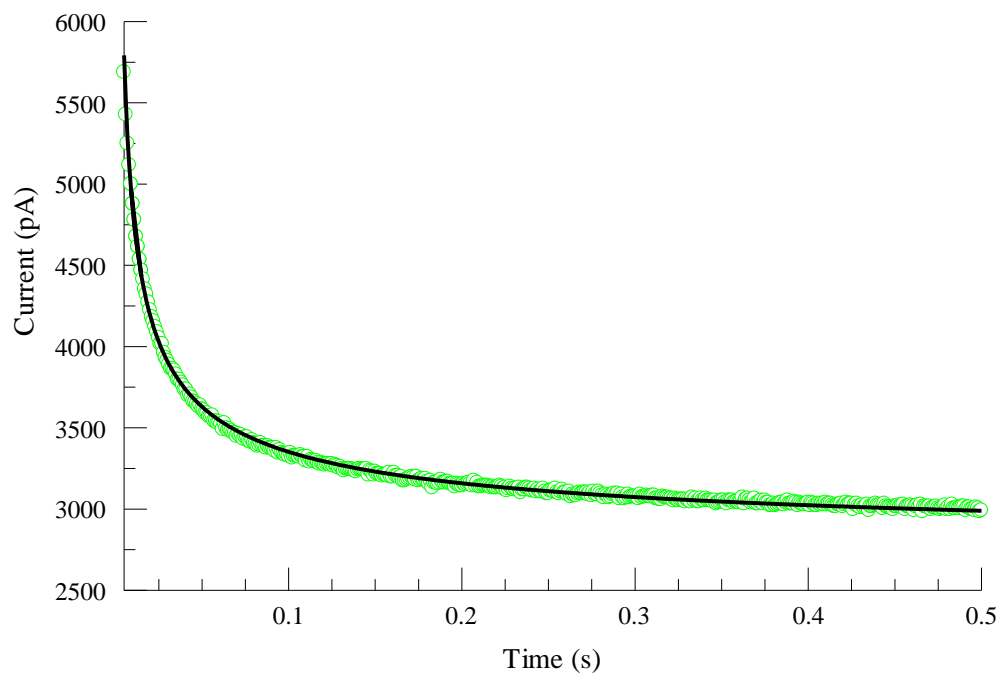


Figure 12: Experimental and calculated data for oxygen diffusion in [N4441][beti] RTIL. Open circles are the experimental data points while the solid line is the fit to equation 11.

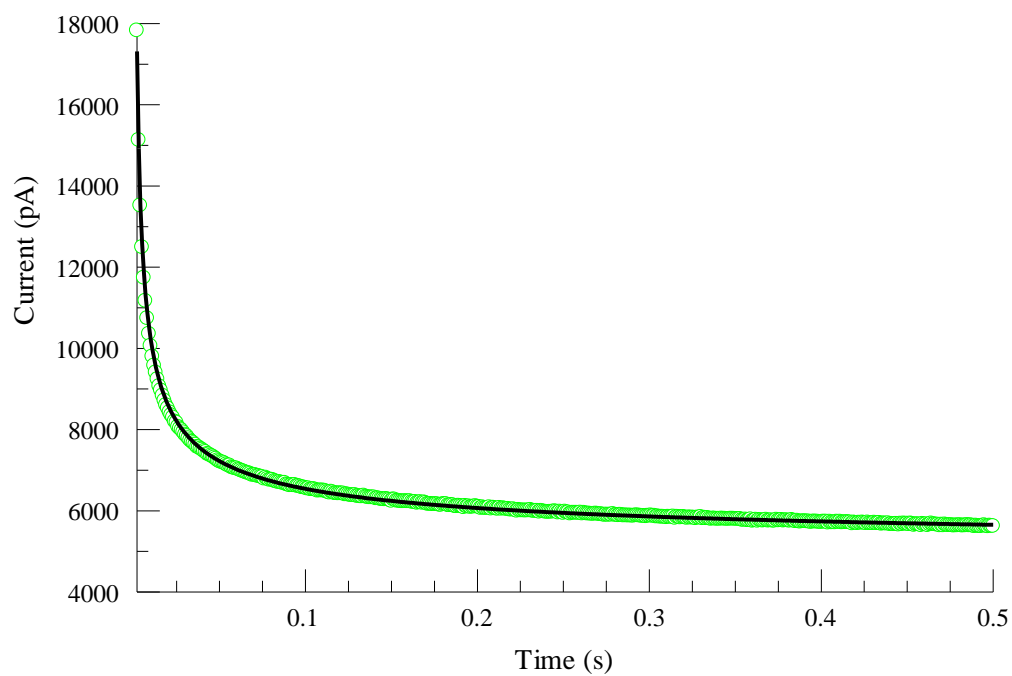


Figure 13: Experimental and calculated data for oxygen diffusion in [C3mmim][beti] RTIL. Open circles are the experimental data points while the solid line is the fit to equation 11.

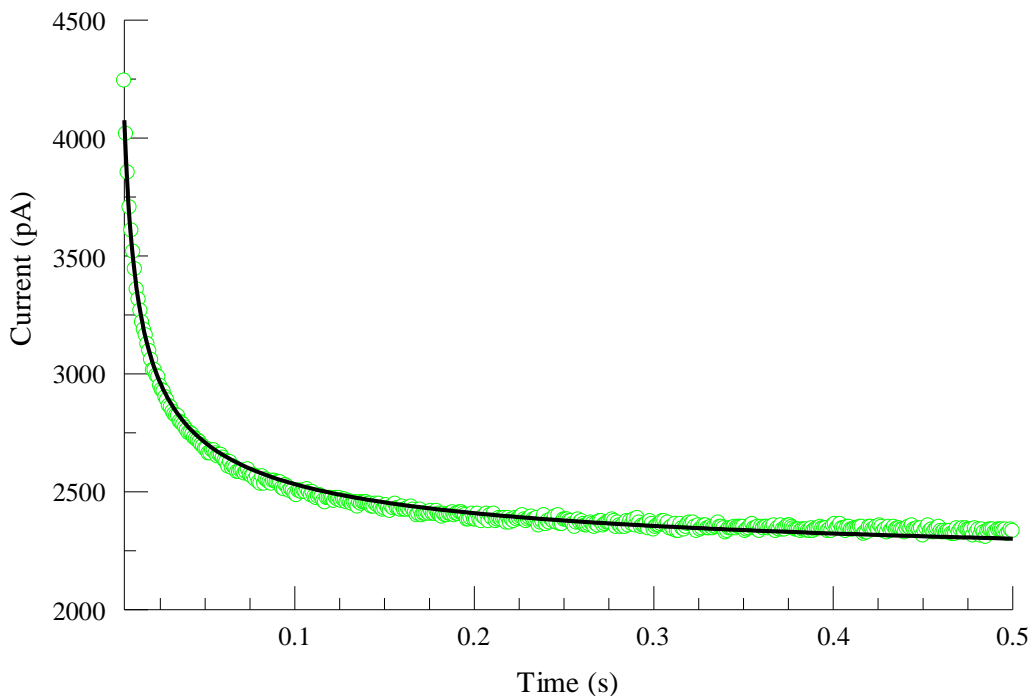


Figure 14: Experimental and calculated data for oxygen diffusion in [P14666][Tf₂N] RTIL. Open circles are the experimental data points while the solid line is the fit to equation 11.

The distortion in the chronoamperometric profile of Figure 11 is the result of oxygen pockets in the sample. During the oxygen purging of the [C6mpy][Tf₂N] RTIL shown in Figure 11, visible bubbles were observed. The bubbles were approximately tens of microns in diameter. Relative to the size of the electrode, the volume of pure oxygen contained in the bubbles was significantly large. The bubbles of oxygen create localized pockets of high oxygen concentration. Spikes in the current occur as the oxygen bubbles diffuse to the surface of the working electrode.

The experimental data was fit remarkably well to the Shoup and Szabo equation over both the transient and steady state regions. A single step, one electron transfer, was assumed in the fitting. The values of D and c for the all the RTILs investigated in this work are displayed in Table 1. Values for the [C4mpy][beti] system are not reported due to problems with the measurement resulting from insufficient amounts of that particular RTIL available to produce reliable results.

RTIL	$D \times 10^{-6} \text{ (cm}^2 \cdot \text{sec}^{-1}\text{)}$	$[\text{O}_2] \text{ (mM)}$
Emmim [Tf ₂ N]	7.33 ± 0.3^a	5.18 ± 0.7^a
C4mpy [Tf ₂ N]	8.24 ± 0.03	2.93 ± 0.03
C6mpy [Tf ₂ N]	4.23 ± 0.06	6.57 ± 0.08
C10mpy [Tf ₂ N]	6.04 ± 1.8^a	5.24 ± 1.3^a
P14666 [Tf ₂ N]	9.2 ± 0.1	1.17 ± 0.01
C3mmim [beti]	3.54 ± 0.02	7.11 ± 0.03
N4441 [beti]	6.16 ± 0.03	2.23 ± 0.009
a) Average and SD of three separate measurements		

The values shown in Table 1 are consistent with other values of oxygen diffusion coefficients and oxygen concentrations in RTILs reported elsewhere in literature.¹⁴⁻¹⁶ With the exception of the [Emmim][Tf₂N] and [C10mpy][Tf₂N] systems the standard deviations reported in Table 1 are from the PSI Pot fitting routine. For the [Emmim][Tf₂N] and [C10mpy][Tf₂N] RTILs the standard deviation from three independent measurements are reported instead.

Table 2 list literature values of oxygen diffusion coefficients and oxygen concentrations for some of the same RTILs that were used in our study. In both literature studies the Shoup and Szabo equation was also used to evaluate chronoamperometric data from a micro-disk electrode. The only glaring discrepancy between our results and that of the literature values listed in Table 2 are for the [P14666][Tf₂N] system. A closer look at the chronoamperometric data shows that our fit to the Shoup and Szabo equation begins to increasingly deviate from the steady state value. The steady state current is directly proportional to the concentration of oxygen. As seen in Figure 14, the fit falls below our measured values in the steady state region. As a result it is not surprising that our measured oxygen concentration value for this particular RTIL is low. It appears as though the routine is fitting for a steady state region at some relatively low value for oxygen concentration. In the literature cited, Evans et. Al also had problems fitting their oxygen diffusion data of the [P14666][Tf₂N] RTIL to the Shoup and Szabo equation. They attributed the deviations in the data from the best fit to multiple electron transfer processes.

RTIL	T (K)	D x10 ⁻⁶ (cm ² ·sec ⁻¹)	[O ₂] (mM)
Emmim [Tf ₂ N]	Room Temp	8.3	3.9
P14666 [Tf ₂ N]	308	6.0 ± 0.5	7.5 ± 0.6

Additional measurements were also made to demonstrate the reproducibility of our results. [Emmim][Tf₂N] and [C10mpy][Tf₂N] were the two RTILs chosen for these measurements. In addition to having relatively large amounts of [Emmim][Tf₂N] and [C10mpy][Tf₂N] RTILs, their data sets produced some of the better and the worse fits, respectively, to the Shoup and Szabo equation during the initial experiment. The precision of our results are shown in Table 3. The six reproducibility measurements were all performed in the same day, but several weeks after the initial chronoamperometric experiments were done. The standard deviations reported in Table 3 are from the PSI Pot fitting routine.

While the [Emmim][Tf₂N] system produced very reproducible results, the [C10mpy][Tf₂N] showed poor reproducibility in these measurements. Impurities in the [C10mpy][Tf₂N] RTIL is most likely the cause of the poor data fitting and poor reproducibility.

Electroactive impurities in the RTIL would greatly complicate the chemistry in the system during the electrochemical measurements. These impurities could interact with the working electrode, the superoxide, and/or ions of the RTIL. The highly reactive nature of the superoxide generated during the reduction of oxygen further compounds the problem. Electrochemical reactions between the highly reactive superoxide and

impurities would be likely. Moreover, simple background subtraction of the argon purged data wouldn't resolve this issue. Furthermore, any electrochemical reactions involving impurities wouldn't necessarily be reproducible. Additional currents resulting from unknown and uncorrected for electrochemistry could account for the lower quality fits and almost 50% deviation in the oxygen diffusion coefficient values obtained between reproducibility runs in the [C10mpy][Tf₂N] RTIL system.

Emmim [Tf ₂ N]	Run 1	Run 2	Run 3	Average	SD
D x10 ⁻⁶ (cm ² ·sec ⁻¹)	7.07 ± 0.05	7.27 ± 0.03	7.66 ± 0.02	7.33	0.3
[O ₂] (mM)	5.36 ± 0.03	4.45 ± 0.02	5.73 ± 0.01	5.18	0.7
C10mpy [Tf ₂ N]					
D x10 ⁻⁶ (cm ² ·sec ⁻¹)	6.48 ± 0.03	7.59 ± 0.07	4.04 ± 0.05	6.04	1.82
[O ₂] (mM)	4.9 ± 0.04	4.14 ± 0.03	6.68 ± 0.03	5.24	1.3

Conclusion

Oxygen diffusion coefficients and the oxygen solubility for several RTILs were measured using electrochemical methods. These measurements will be used to verify the results of the oxygen diffusion coefficient measurements made using the developed confocal fluorescence microscopy method. Also, the calculated oxygen solubility will be used to determine true bimolecular quenching rate constants in each of the RTILs studied.

While we appear to have achieved good results for our electrochemical measurements, there are several factors that could produce errors and/or cause our values to differ from others reported. For example, all measurements during this investigation were made at room temperature, but the temperature of the RTIL systems was not monitored or controlled during any of our electrochemical experiments. When comparing the results of any measurement involving diffusion of a gas in a solvent, it is important to understand that diffusion rates, as well as solubility of the gas, may greatly vary with temperature. This was shown by Huang et al in an experiment in which oxygen diffusion in a series of RTILs was studied over a temperature range of 293 – 318 K using chronoamperometry.¹⁵ The researchers found that while the oxygen concentration didn't change much over the given temperature range, the oxygen diffusion coefficient varied by up to 70%.

Also, RTILs are known to be susceptible to impurities. Impurities in our RTILs were first noticed during our quenching experiments because of their intense fluorescence. Any electroactive impurities from the synthesis of the RTILs that are still present in the system could adversely affect electrochemical measurements. The superoxide, O_2^- , produced by the applied voltage is extremely reactive and may react with these impurities.

Furthermore, RTILs are also known to be very prone to water absorption; the potentials used in the reduction of oxygen are of the same range for the reduction of water. While all of these factors may be significant problems associated with the evaluation of any electrochemical diffusion measurements in RTILs, we are confident in the quality of our results.

Reference – Chapter 8

1. R. Olenick; T, Apostol; D, Goodstein. Beyond the mechanical universe: from electricity to modern physics. Cambridge University Press. **1986**
2. D. Oxtoby; N. Nachtrieb. "Principles of Modern Chemistry." 3rd Edition; Saunders College Publishing. 1996
3. P. Kissinger; W, Heineman. "Laboratory Techniques in Electroanalytical Chemistry." Marcel Dekker. 1984
4. Meites; Thomas; "Advanced Analytical Chemistry.",
5. J, Bockris; A, Reddy. Modern Electrochemistry I. Plenum Press: New York. **1970**
6. F, Cottrell. Z. Phys. Chem. 42. **1903**, 385
7. P. Kovach; W. Caudil; D. Peters; M. Wightman. "Faradaic Electrochemistry at Microcylinder, Band, and Tubular Electrodes." J. Electroanal. Chem. 1985
8. J. Baur; M. Wightman. "Diffusion Coefficients Determined with Microelectrodes.",
9. T. Hepel; J. Osteryoung. "Chronoamperometric Transients at the Stationary Disk Microelectrode." Department of Chemistry, State University of New York at Buffalo. 1981

10. K. Oldham; C. Zoski. "Comparison of Voltammetric Steady States at Hemispherical and Disc Microelectrodes.",
11. A. Bond; K. Oldham; C. Zoski. "Steady state voltammetry,
12. G. Denault; M. Mirkin; A. Bard. "Direct Determination of Diffusion Coefficients by Chronoamperometry at Microdisk Electrodes.",
13. D. Shoup; A. Szabo. "Chronoamperometric Current at Finite Disk Electrodes." *J Electroanal. Chem* 1982
14. R. Evans; O. Klymenko; S. Saddoughi; C. Hardacre; R. Compton. "Electroreduction of Oxygen in a Series of Room Temperature Ionic Liquids Composed of Group 15-Centered Cations and Anions." *J. Phys. Chem* 2004
15. X. Huang; E. Rogers; C. Hardacre; R. Compton. "The Reduction of Oxygen in Various Room Temperature Ionic Liquids in the Temperature Range 293-318 K: Exploring the Applicability of the Stokes-Einstein Relationship in Room Temperature Ionic Liquids." *J. Phys Chem.* 2009
16. M. Buzzeo; O. Klymenko; J. Wadhawan; C. Hardacre; K. Seddon; R. Compton. "Voltammetry of oxygen in the room-temperature ionic liquids 1-ethyl-3-methylimidazolium bis((trifluoromethyl)sulfonyl)imide and hexyltriethylammonium

bis((trifluoromethyl)sulfonyl)imide: one-electron reduction to form superoxide. Steady-state and transient behavior in the same cyclic voltammogram resulting from widely different diffusion coefficients of oxygen and superoxide” J. Phys Chem. 2003

17.D, Sawyer; E, Seo. One-Electron Mechanism for the Electrochemical Reduction of Molecular Oxygen. Inorganic Chemistry, Vol. 16. **1976**

18.R, Ferrell; D, Himmelblau. Oxygen in Water. Journal of Chemical and Engineering Data. Vol. 12. **1967**

19.D, Maricle; W, Hodgson. Reduction of Oxygen to Superoxide Anion in Aprotic Solvents. Anal. Chem. Vol. 37. **1965**

Chapter 9: Discussion and Future Work

Introduction

The luminescence based oxygen sensing of the Ru(II)/RTIL systems investigated in this work is predicated on the deactivation of the excited MLCT state of the luminescent metal complex. This deactivation, also known as quenching, is the result of collisions between oxygen and the metal complex. Therefore, the distance oxygen can travel during the excited state lifetime of the complex will ultimately determine the oxygen sensing capability of the system.

Oxygen diffusion coefficients in several RTILs have been measured using two independent techniques to help explain the remarkable oxygen quenching exhibited in the systems. Confidence in the D values obtained is essential before any detailed evaluation of the oxygen quenching can be initiated.

For diffusion controlled reactions, the maximum theoretical rate constants for reaction are determined by the diffusion coefficients of the reacting species. The information obtained from the experiments described in Chapters 7 and 8 is used to provide insight into the anomalously high quenching observed in the Ru(II)/RTIL systems.

The feasibility of RTILs for real world luminescence oxygen sensing applications is examined by investigating the oxygen quenching of a Ru(II)/ionic liquid encapsulated gel, ILEG.

Oxygen Diffusion Measurements

In order to assess the validity of the oxygen diffusion coefficients measured using our Confocal Fluorescence Microscopy method described in Chapter 7, oxygen diffusion coefficients for the RTILs examined in this work were measured using the electroanalytical technique known as chronoamperometry as detailed in Chapter 8. Electroanalytical techniques such as chronoamperometry have been used for decades to investigate the diffusion properties of electroactive species. Additionally, the reduction of oxygen in solvents is a well-studied process. These two factors combined make chronoamperometric evaluation of oxygen diffusion coefficients in RTILs the ideal method for appraising the effectiveness of our diffusion measurements reported in Chapter 7. Table 1 shows the values of D calculated by both methods.

Table 1. Oxygen Diffusion Coefficients in RTILs			
RTIL	Confocal Fluorescence Microscopy Method		Chronoamperometric Method
	D x10 ⁻⁶ (cm ² ·sec ⁻¹)	χ^2	D x10 ⁻⁶ (cm ² ·sec ⁻¹)
Emmim [Tf ₂ N]	8.91	.106	7.33 ± 0.3 ^a
C4mpy [Tf ₂ N]	9.13	.207	8.24 ± 0.03
C6mpy [Tf ₂ N]	4.46	.078	4.23 ± 0.06
C10mpy [Tf ₂ N]	16.1	.061	6.04 ± 1.8 ^a
P14666 [Tf ₂ N]	10.8	.064	9.2 ± 0.1
C3mmim [beti]	8.91	.2	3.54 ± 0.02
N4441 [beti]	10.83	.076	6.16 ± 0.03
C4mpy [beti]	6.55	.163	

a) Average of three measurements, with SD between the measured values

On comparison of the diffusion coefficients, there is good agreement between the results evaluated using the two completely different techniques. The agreement between the two sets of results, however, is not perfect. The [C10mpy] [Tf₂N] RTIL produced the largest discrepancy between D values obtained by the two separate methods. This comes as no surprise given that the [C10mpy] [Tf₂N] RTIL produced some of the poorer fit data sets during the chronoamperometric experiments. Impurities in the RTILs, first noticed during luminescence quenching experiments, is believed to be the major cause of the poor fit for the [C10mpy] [Tf₂N] chronoamperometric measurement.

As seen in Table 2, literature results obtained for oxygen diffusion coefficients in two of the same RTILs used in this study are similar in value to those measured by both diffusion methods in this work. This provides

further demonstration of the validity of our newly developed technique for measuring oxygen diffusion coefficients.

	Confocal Method	Electrochemical Method	Literature Value
RTIL	$D \times 10^{-6} \text{ (cm}^2 \cdot \text{sec}^{-1}\text{)}$	$D \times 10^{-6} \text{ (cm}^2 \cdot \text{sec}^{-1}\text{)}$	$D \times 10^{-6} \text{ (cm}^2 \cdot \text{sec}^{-1}\text{)}$
Emmim [Tf2N]	8.91	7.33 ± 0.3^a	8.3
P14666 [Tf2N]	10.8	9.2 ± 0.1	6.0 ± 0.5^b

a) Average of three separate measurements b) Temperature = 308 K

It is well-known that RTILs can contain high concentrations of impurities. Electrochemical reactions associated with impurities in RTILs can adversely affect chronoamperometric diffusion measurements. Our method for measuring oxygen diffusion coefficients are not influenced by these undesired impurities. As a result, our D values are preferred and therefore used in the analysis of the bimolecular quenching rate constants in the RTILs.

Quenching Rate Constants

Chronoamperometric measurements performed in Chapter 8 not only substantiated our previously evaluated diffusion coefficients but they also yielded a parameter essential for determining true bimolecular quenching rate constants, k_q , for each RTIL, oxygen solubility. The solubility of oxygen in RTILs is information is generally not known. Table 3 shows the oxygen solubility for the RTILs investigated in this work.

RTIL	Chronoamperometric Measurement [O ₂] (mM)	Literature Value [O ₂] (mM)
Emmim [Tf2N]	^a 5.18 ± 0.7	3.9
C4mpy [Tf2N]	2.93 ± 0.03	7.5 ± 0.6 ^b
C6mpy [Tf2N]	6.57 ± 0.08	
C10mpy [Tf2N]	^a 5.24 ± 1.3	
P14666 [Tf2N]	1.17 ± 0.01	
C3mmim [beti]	7.11 ± 0.03	7.5 ± 0.6 ^b
N4441 [beti]	2.23 ± 0.009	

a) Average and SD of three separate measurements. b) Temperature = 308 K

The bimolecular quenching rate constant for the deactivation of the MLCT of the Ru(II) complexes described in Chapter 6 is related to the Stern-Volmer quenching constant, K_{SV} , and the unquenched lifetime, τ_0 , of the MLCT excited state by

$$k_q = K_{SV} / \tau_0 \quad (1)$$

For a diffusion-controlled process, such as the dynamic quenching of the excited Ru(II) MLCT state by oxygen, the observed rate constant is limited by the rate of diffusion of the reacting species. In such cases the maximum rate constant for the reaction (excited state deactivation), k_{max} , can be obtained by the Smoluchowski equation¹ by

$$k_{max} = \frac{4\pi N(r_{Ru(II)} + r_{O_2})(D_{Ru(II)} + D_{O_2})}{1000} \quad (2)$$

where N is Avogadro's number, $r_{Ru(II)}$ is the radius of the luminescent Ru(II) TMC, r_{O_2} is the radius of the quencher, oxygen, $D_{Ru(II)}$ is the diffusion

coefficient of the Ru(II) complex, and D_{O_2} is the diffusion coefficient of oxygen.

The Stokes-Einstein relationship can be used to predict the diffusion coefficients, D , by

$$D = k_b T / 6\pi\eta R \quad (3)$$

where, k_b is the Boltzmann's constant, T is temperature in Kelvin, η is the viscosity, and R is the molecular radius of the diffusing species.¹ If we assume equivalent radii for the two reacting species while substituting equation 3 into equation 2, k_{max} can be estimated as

$$k_{max} = 8Nk_b T / 3000\eta \quad (4)$$

True bimolecular quenching rate constants and Stern-Volmer constants based on the oxygen solubility measurements of Chapter 8 and the maximum quenching rate constants predicted by the Smoluchowski equation for the Ru(II)/RTILs studied are shown in Table 4. For comparison, unquenched lifetimes and viscosities are also included in the table.

Table 4. Oxygen Quenching of Ru(II) TMCs in RTILs						
Ru(II) TMC	RTIL	τ_0 (μs)	K_{sv} (M^{-1})	$k_{\text{q}} \times 10^{-9}$ ($\text{M}\cdot\text{s}^{-1}$)	$k_{\text{max}} \times 10^{-9}$ ($\text{M}\cdot\text{s}^{-1}$)	η (cP)
Ru(dpp)₃²⁺	Emmim [Tf2N]	5.9	5676	0.96	0.17	38
	C4mpy [Tf2N]	5.7	8362	1.47	0.072	94
	C6mpy [Tf2N]	6.1	3364	0.55	0.092	73
	C10mpy [Tf2N]	5.7	3798	0.67	0.06	110
	P14666 [Tf2N]	4.8	16923	3.53	0.023	290
	C3mmim [beti]	5.5	2377	0.43	0.024	277
	N4441 [beti]	5.2	7130	1.37	0.0064	>1200
	C4mpy [beti]	5.5		1.28 ^a	0.04	160
Ru(bpy)₃²⁺	P14666 [Tf2N]	0.516	1846	3.58	0.0023	290
	C4mpy [Tf2N]	0.695	901	1.30	0.072	94
	C6mpy [Tf2N]	0.665	435	0.65	0.092	73
	C10mpy [Tf2N]	0.650	475	0.73	0.06	110
	a) [O ₂] of 3mM was assumed					

As visible in Table 4, the predicted values of k_{max} grossly underestimates the experimentally measured bimolecular quenching rate constants. The mostly obvious problem is the invalid assumption that the radii of oxygen and the Ru(II) complexes are equivalent. With that in mind, k_{max} was recalculated using estimated radii for molecular oxygen and the Ru(II) complex. r_{O_2} was taken as the molecular bond length 1.21 Å. Mercury 3.0 (UK) software was used to estimate $r_{\text{Ru(II)}}$ as 9.1 Å and 6.5 Å for Ru(dpp)₃²⁺ and Ru(bpy)₃²⁺ respectively. Using these values for the radii, the Smoluchowski equation and the Stokes-Einstein equation were combined to give new k_{max} values. The recalculated k_{max} values using the estimated radii for oxygen and Ru(II) complexes are shown in Table 5. Also

included in the table, for comparison, are the experimental bimolecular quenching rate constants and viscosities.

Ru(dpp)₃²⁺	RTIL	k_q × 10⁻⁹ (M·s)⁻¹	k_{max} × 10⁻⁹ (M·s)⁻¹	η (cP)
	Emmim [Tf2N]	0.96	0.43	38
	C4mpy [Tf2N]	1.47	0.17	94
	C6mpy [Tf2N]	0.55	0.22	73
	C10mpy [Tf2N]	0.67	0.15	110
	P14666 [Tf2N]	3.53	0.056	290
	C3mmim [beti]	0.43	0.058	277
	N4441 [beti]	1.37	0.013	>1200
	C4mpy [beti]	1.28	0.10	160
Ru(bpy)₃²⁺				
	P14666 [Tf2N]	3.58	0.043	290
	C4mpy [Tf2N]	1.30	0.13	94
	C6mpy [Tf2N]	0.65	0.17	73
	C10mpy [Tf2N]	0.73	0.11	110

Even after correcting for the discrepancy between the radii of the two reacting species, predicted k_{max} values still substantially underestimate the bimolecular quenching rate constants. This is most evident for the higher viscosity RTILs. Also, within the RTILs the bimolecular quenching rate constants do not demonstrate the $1/\eta$ dependence as predicted by equation 3. In fact, quenching appears to be completely independent of viscosity.

We ascribe the high degree of quenching and its invariance, relative to viscosity, to the unique structure of the RTILs. As discussed in Chapter 5, it is known that RTILs can have considerable short range order. There are two main theories regarding the structure of RTILs. One suggests that RTILs

exist as crystal structures with liquid-like channels connecting them.⁴⁻⁶ The other proposes that the bulky cations of the RTILs form aggregates surrounded by free anions.⁸⁻⁹ Either theory provides a mechanism as to how RTILs have high viscosities yet simultaneously maintain excellent oxygen quenching. Inside RTILs the crystal-like patches or aggregates hinder the motion of the system thus creating its macroscopic viscosity, while channels between the patches or aggregates provide open pathways for fluent oxygen diffusion.

As seen in Table 5 from the experimentally measured D values, the diffusion of oxygen through the RTILs is not affected by the magnitude of the macroscopic viscosity. Even within the RTILs where the most viscous sample, [N4441][Tf2N], is more than 30 times more viscous than the least viscous, [Emmim][Tf2N], RTIL the values of k_q differ by no more than 12%. Oxygen is able to rapidly move through the open channels in the RTILs, quenching the Ru(II) luminescence. The Ru(II) complex may be free to move through the open channels as well as may be bound to the aggregates. Regardless, it's the unimpeded motion of oxygen through the channels that accounts for the high degree of quenching.

Ru(II) TMC	RTIL	$k_q \times 10^{-9} \text{ (M}\cdot\text{s)}^{-1}$	$D \times 10^{-6} \text{ (cm}^2\cdot\text{sec}^{-1}\text{)}$	$\eta \text{ (cP)}$
Ru(dpp) ₃ ²⁺	Emmim [Tf2N]	0.96	8.91	38
	C4mpy [Tf2N]	1.47	9.13	94
	C6mpy [Tf2N]	0.55	4.46	73
	C10mpy [Tf2N]	0.67	16.1	110
	P14666 [Tf2N]	3.53	10.8	290
	C3mmim [beti]	0.43	8.91	277
	N4441 [beti]	1.37	10.83	>1200
	C4mpy [beti]	1.28 ^a	6.55	160
	a) [O ₂] of 3mM was assumed			

The Stokes-Einstein equation is often used to estimate diffusion coefficients because, generally, D values aren't typically a commonly known parameter. Actual D values for oxygen in our RTILs, calculated using the confocal fluorescence microscopy diffusion technique were substituted into equation 2 and used to determine a new set of diffusion-limited bimolecular quenching rate constants, $k_{\text{max}2}$. Diffusion coefficients for the metal complexes are not known for all of the RTILs studied. However, D for Ru(dpp)₃²⁺ in [Emmim][Tf₂N] was calculated using Fluorescence Correlation Spectroscopy (FCS). This value was used in calculations for all samples. Values for the experimentally determined bimolecular quenching rate constant and the predicted diffusion-limited rate constants determined by both methods are shown in Table 7.

Table 7. Diffusion Limited Quenching Rate Constants of Ru(II)/RTIL Systems					
Ru(dpp) ₃ ²⁺	RTIL	Experimental k _q × 10 ⁻⁹ (M·s) ⁻¹	Eq. 2 with D calculated from Eq. 3 k _{max} × 10 ⁻⁹ (M·s) ⁻¹	Eq. 2 with experimentally determined D k _{max2} × 10 ⁻⁹ (M·s) ⁻¹	η (cP)
	Emmim [Tf2N]	0.96	0.43	7.2	38
	C4mpy [Tf2N]	1.47	0.17	7.4	94
	C6mpy [Tf2N]	0.55	0.22	3.7	73
	C10mpy [Tf2N]	0.67	0.15	13	110
	P14666 [Tf2N]	3.53	0.056	8.7	290
	C3mmim [beti]	0.43	0.058	7.2	277
	N4441 [beti]	1.37	0.013	8.7	>1200
	C4mpy [beti]	1.28	0.10	5.3	160
Ru(bpy)₃²⁺					
	P14666 [Tf2N]	3.58	0.043	6.4	290
	C4mpy [Tf2N]	1.30	0.13	5.5	94
	C6mpy [Tf2N]	0.65	0.17	2.7	73
	C10mpy [Tf2N]	0.73	0.11	9.5	110

Substitution of experimentally obtained Ds produced calculated k_{max2} values greater than those experimentally obtained. It is assumed by the use of equation 2 that every oxygen/Ru(II) encounter will quench the excited MLCT state. However, the efficiency of oxygen quenching is not likely to be 100%, resulting in an overestimation of predicted bimolecular quenching rate constants.

The Stokes-Einstein equation obviously fails to predict the oxygen diffusion in our RTIL systems. The model assumes spherical diffusing species through a continuous media.¹⁴ Due to their symmetry, both metal complexes can be assumed to be spherical. However, this assumption is invalid for molecular oxygen. Also, the Stokes-Einstein relationship was originally determined for molecules that are large relative to the diffusive

media.¹ Again, this assumption is invalid for molecular oxygen diffusing through the RTILs. When used to calculate diffusion coefficients for small molecules relative to the diffusive media, equation 3 tends to underestimate D values.¹

Ionic Liquid Encapsulated Gels Oxygen Sensing

Properties

Thin films are often used in luminescence sensing because for many applications it is impractical to have a luminophore in solution. The luminescent probe is often embedded in a polymer to provide physical support. For the case of a luminophore in solution, while instantaneously molecules are in different environments, the molecular motion of the system is fast enough to allow sampling of all local environments during the excited state lifetime of the luminophore. This makes all molecules equivalent, and the decays are single exponential. However, in a polymer where the system is rigid, there is not ample molecular motion to allow for sampling of all the local environments during the luminescence decay, thus creating a heterogeneous system. Since the local surrounding of the luminophore affects its emission characteristics, heterogeneity of the system can lead multiexponential decays and deviation from ideal sensor characteristics.

For many oxygen sensing applications having the luminophore in solution is not a feasible design. However, the adverse effects of having the luminophore in a polymer support are not desirable either. Ionic liquid encapsulated sol gels, ILEGs, provide a transparent rigid sensor support without the adverse effects mentioned above.

Preliminary oxygen quenching data of $\text{Ru}(\text{dpp})_3^{2+}$ dissolved in $[\text{Emmim}][\text{Tf}_2\text{N}]$ encapsulated in a 28% by weight silica sol gel along with data from the metal complex dissolved in pure ionic liquid are shown in Table 8. The unquenched lifetime and the bimolecular quenching rate constant are almost the same for the two systems. With the amount of silica in the sol gel it is not surprising that there are some differences between the ILEG and pure ionic liquid. FCS measurements of $\text{Ru}(\text{dpp})_3^{2+}$ in the pure RTIL and in the ILEG produced values of $D=2.5 \times 10^{-7}$ and $D=1.25 \times 10^{-7}$ respectively. That the motion of the large metal complex is further hindered by the silica matrix is understandable. The magnitude of the diffusion coefficient of oxygen is greater than an order of magnitude larger than that of the metal complex. As a result, the diffusion of oxygen through the systems plays the dominant role relative to the metal complex. The marginal difference between the quenching in the ILEG and the pure ionic liquid is attributed to the high mobility and small size of molecular oxygen.

Table 8. Oxygen Diffusion and Quenching of Ru(dpp)₃²⁺ in RTIL and ILEG			
	τ_0 (μ s)	$k_q \times 10^{-9}$ (M·s) ⁻¹	η (cP)
Emmim [Tf2N]	5.9	0.96	38
Emmim [Tf2N] ILEG	6.2	0.81 ^a	Solid
a) [O ₂] of pure RTIL assumed			

As seen in Figures 1 and 2, the lifetime and oxygen quenching temperature dependence for the ionic liquid and ILEG systems show remarkable similarity as well. As the temperature dependence of both the oxygen quenching and the luminescence lifetime are extremely sensitive to the local environment of the sensor, this further suggests that the luminescent complex behaves much like as if it is in pure ionic liquid with minimum affects from the rigid silica matrix. The near pure exponentiality of the decays in the ILEG further supports that the complex is effectively dissolved in the ionic liquid domains.

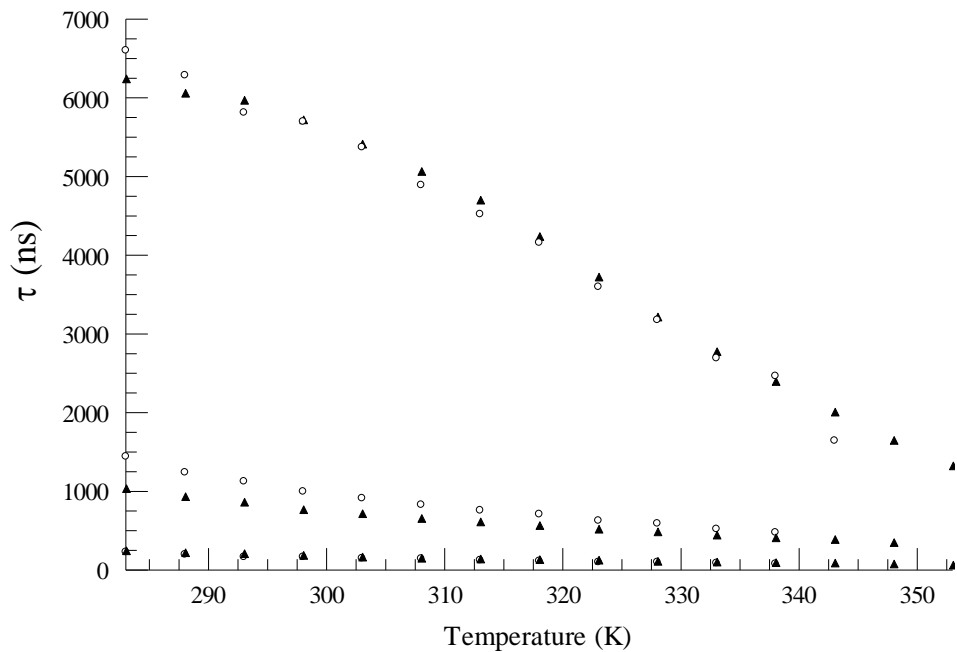


Figure 1. Lifetime temperature dependence of $\text{Ru}(\text{dpp})_3^{2+}$ in $[\text{Emmim}][\text{Tf}_2\text{N}]$ RTIL and $[\text{Emmim}][\text{Tf}_2\text{N}]$ ILEG for nitrogen, air, and oxygen purged samples. The open circles are ILEG data and the solid triangles are $[\text{Emmim}]$ solution.

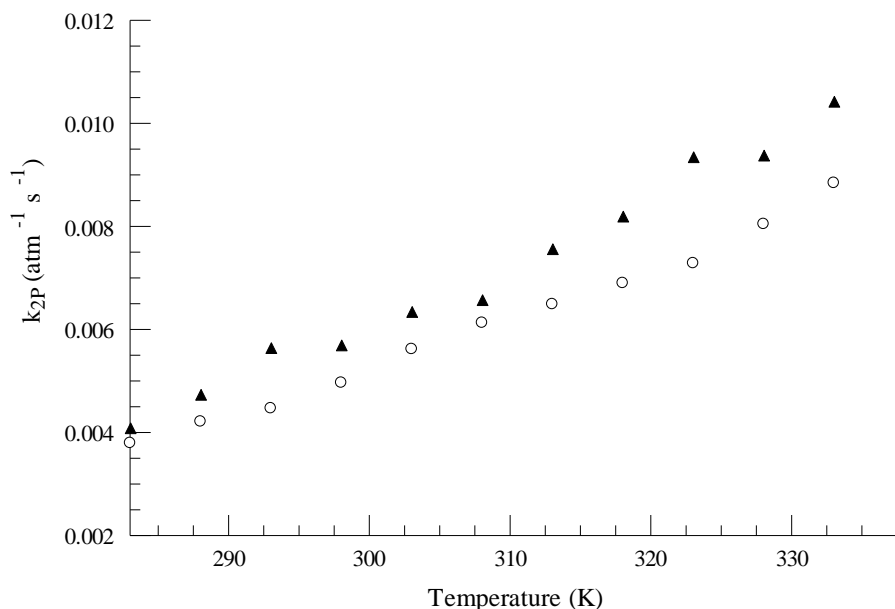


Figure 2. Lifetime temperature dependence of pseudo bimolecular quenching rate constant, k_{2P} , for [Emmim][Tf₂N] RTIL and [Emmim][Tf₂N] ILEG. The open circles are [Emmim] solution and solid triangles are ILEG data.

Conclusions and Future Work

In conclusion, the unique structure of RTILs was used to explain the exceptionally high luminescence oxygen quenching of Ru(II) TMCs in a series of RTILs and an [Emmim][Tf₂N] encapsulated gel. Aggregation of the large bulky cations can cause RTILs to have extremely high macroscopic viscosities. A newly developed method for measuring oxygen diffusion coefficients revealed that the oxygen diffusion in RTILs is not affected by

the large macroscopic viscosity of the RTILs. The highly mobile oxygen molecule rapidly diffuses through channels in the RTILs, quenching the Ru(II) luminescence.

The quenching behavior of sol gels based on [Emmim][Tf₂N] RTIL closely resembled that of the pure [Emmim][Tf₂N] ionic liquid. The small variations between the quenching performance of the pure ionic liquid and the ILEG are attributed to the metal complex's interaction with the silica matrices.

Future experiments will expand upon the oxygen diffusion measurements carried out in this work. Oxygen diffusion coefficients in ILEGs will be determined using the method developed by the Demas group.

Also, efforts are currently underway to construct a RTIL based on a luminescent TMC. The ideal is to attach the proper ligands in the proper way to a luminescent TMC, such as Re(I), to create a bulky, highly asymmetrical, luminescent cation. With a luminescent RTIL, extremely thin films could be made without having to worry about dye concentrations and absorbance which would yield low signals.

RTILs show great promise as luminescence sensor supports and have the potential of becoming the next great advancement in luminescence based sensor technology.

Reference – Chapter 9

1. J. Lakowicz. "Principles of Fluorescence Spectroscopy." 2nd ed.; KluwerAcademic/Plenum Publishers: New York, 1999.
2. A. Einstein. *Z. Elektrochem.* 14, **1908**, 235
3. E, Reynolds; J, Demas; B, DeGraff. Viscosity and Temperature Effects of Oxygen Quenching of Tris-(2,2'-bipyridine)ruthenium(II).
4. Gomes, M. F.; Lopes, J. N.; and Padua, A. "Thermodynamics and Micro Heterogeneity of Ionic Liquids." *Top Curr Chem.* **2009**
5. Liu, Y.; Li, J.; Wang, M.; Li, Z.; Liu, H.; He, P.; Yang, X.; Li, J. "Preparation and Properties of Nanostructure Anatase TiO₂ Monoliths Using 1-Butyl-3-methylimidazolium Tetrafluoroborate Room-Temperature Ionic Liquids as Template Solvents." *Crystal Growth & Design*, **2005**, 5 (4), pp 1643–1649
6. Triolo, A.; Russina, O.; Fazio, B.; Triolo, R.; Di Cola, E. "Morphology of 1-alkyl-3-methylimidazolium hexafluorophosphate room temperature ionic liquids." *Chemical Physics Letters* 457, **2008**, 362–365
7. Katayanagi, H.; Hayashi, S.; Hamaguchi, H.; Nishikawa, K. "Structure of an ionic liquid, 1-n-butyl-3-methylimidazolium iodide, studied by wide-

angle X-ray scattering and Raman spectroscopy.” *Chem. Phys Let.* 392, **2004**, 460–464.

8. Triolo, A.; Russina, O.; Bleif, H.; and Di Cola, E. “Nanoscale Segregation in Room Temperature Ionic Liquids.” *J. Phys. Chem. B.* 111, **2007**, 4641-4644

9. D. Rooney; J. Jacquemin; R. Gardas. “Thermophysical Properties of Ionic Liquids.” *Top Curr Chem.* 290, **2009**, 185-212